POLITECNICO DI TORINO

Department of Mechanical and Aerospace Engineering

Numerical analysis of the non-linear behaviour of a magnetic bearings vertical rotor

Supervisors: Candidate:
Prof. Alessandro Vigliani   Costantino Gagliardi
Prof. Elvio Bonisoli
Ing. Domenico Litisano

Index

1. Introduction

The specialized branch of applied mechanics that deals with the study of behaviour and the diagnosis of rotating structures is rotodynamic.

A rotor is a body suspended through a set of cylindrical hinges or bearings that allows it to rotate freely around an axis fixed in space.

Rotodynamic has been deeply studied in the last century and the correct functioning of a rotor represented a complex engineering problem due to the numerous difficulties deriving from the need to satisfy the various specifications for the different operating conditions.

Rotational motion is employed to achieve translation, to store energy, to transfer power from one point to another and to obtain kinetic energy from other kinds of energy. Rotors used in machines and mechanisms provide numerous advantages as regards efficiency, wear, and easy adjustments.

However, the rotational movements are accompanied by "mechanical side effects".

In fact, due to several factors contributing to energy transfer, the rotor rotation can be accompanied by various vibration modes that depend on the structure of the rotor and its unbalance.

One of the most important works regarding the rotodynamic is undoubtedly that of Jeffcott where the behaviour of a shaft simply supported and with the presence of damping was analysed.

Therefore, he obtained a model that is characterised simply by a synchronous whirl, which represents the only stationary solution.

Starting from the model proposed by Jeffcott, in this thesis work we proposed the study of a vertical axis magnetic rotor usable as kinetic energy accumulator.

In the first part the structure of the rotor is analysed in all its components. The rotor has been called "magnetic rotor" because the bearings used are permanent magnets. In fact, in the second chapter the magnetic behaviour and the characteristics on the dynamics and stability of the system are studied.

In the following chapters, the mathematical model of the rotor was analysed. In the first instance, we focused on a linear behaviour of the system through modal and motion analysis. In the second phase we proceeded to the study of a non-linear system with modal analysis.

It was also decided to pay attention to the case in which the rotor was unbalanced through a dynamic and modal analysis of the system. At the present time, finite elements are widely used to compute critical speeds and unbalance responses.

Finally, we proceeded with a frequency analysis of the system to be able to clearly identify the critical speeds to be analysed in a future experimental analysis.

2. Magnetic rotor

Following the ISO definition, a rotor is a body suspended through a set of cylindrical hinges or bearings that allow it to rotate freely about an axis fixed in space, while the part of the machine that does not rotate is called stator.

The rotor of our interest is a vertical magnetic rotor as shown in Figure 2.1.

Some simplifications that allow the linearization of the mathematical model of rotors can be made. In the undeformed configuration, the rotor has, a well-defined and fixed rotation axis (vertical axis), which coincides with one of the barycentric principal axes of inertia if the rotor is perfectly balanced. This is possible because an unbalanced rotor has only small differences compared to an ideal condition. Also, the displacement of the rotation axis from its nominal position due to deformations or perturbations of the system is reduced.

Another assumption made is that of axial symmetry, so the dynamic study of an axis-symmetrical rotor is greatly simplified.
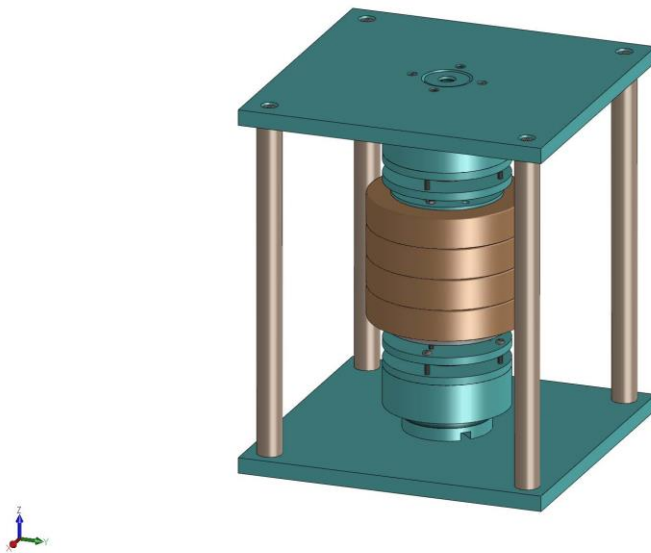
Figure 2.1 – Model of vertical magnetic rotor.

The typical behaviour of a rotor can be simplified through some fundamental aspects:

> - the rotor shafts do not "vibrate", it spins and whirl;
> - the rotor supports undergo vibrations;
> - due to the rotation, the centre of the disk moves on a trajectory whose amplitude depends on the speed;
> - as the speed of rotation increases there is an increase in the amplitude of the vibration. The maximum speed peak is called critical;
> - if the amplitude of the vibration is excessive, catastrophic failures can occur.

The most important elements of the rotor under study are:

- the shaft,

- the hubs,
- magnetic bearings,
- sapphire.

The stator structure is composed by polytetrafluoroethylene (PTFE known as Teflon) elements. The choice to use this material is due to the diamagnetic behaviour of Teflon, in fact the magnetic susceptibility is negative and so it tends to exclude a magnetic field from its interior.

Another important feature is the possibility to change the rotating mass based on the number of hubs on the shaft.

2.1 Rotor components

2.1.1 Shaft

Figure 2.1.1.1 shows the vertical rotor shaft. The shaft is made of aluminium alloy and can be considered as a rigid body. It has not a homogeneous distribution of the mass due to the presence of a flange, a useful support for the brass hubs.

Aluminium has been chosen because of its paramagnetic characteristic, meaning that they are weakly attracted to a magnet: this effect is thousands of times weaker than in ferromagnetic materials.

Figure 2.1.1.1 – Rotor shaft.

2.1.2 Brass hubs

The mass of the rotor assembly is represented by the brass hubs (Figure 2.1.2.1) which are positioned in abutment with the shaft flange. If the number of hubs is increased, the mass and the moment of inertia of the entire rotor increased, too. Furthermore, the centre of the mass is displaced according to a fixed Cartesian reference.
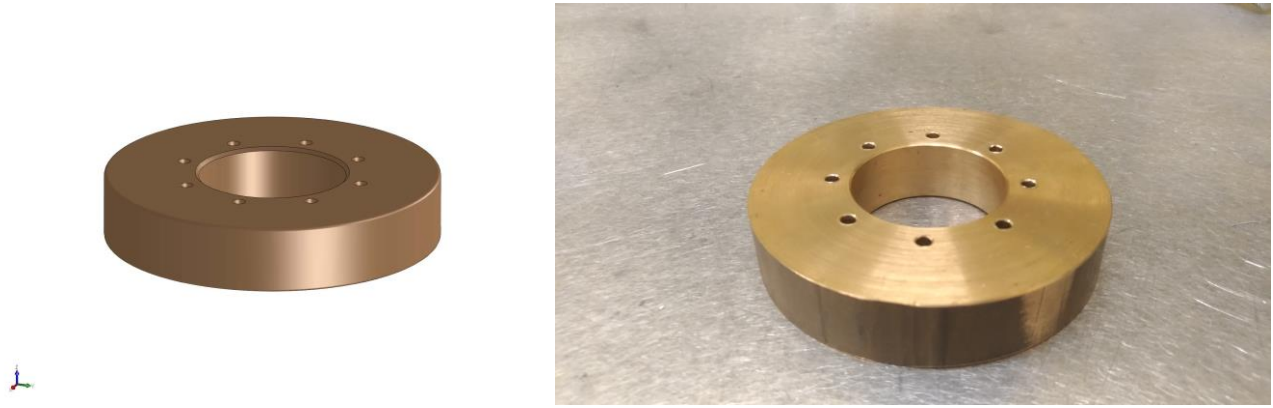
Figure 2.1.2.1 – Brass hub.

2.1.3 Magnetic bearings

In this rotor model there are neodymium magnets. This type of magnets are permanent magnets made from an alloy of neodymium, iron and boron and they are the strongest type of permanent magnet commercially available.

These elements have strong anisotropic characteristics which allow to obtain a residual magnetic induction three or four times stronger than that obtainable by the traditional permanent magnets [2]. Moreover, they have a silvery-white colour, they are fragile, and they are easily damaged.

The neodymium magnets are graded according to their maximum energy product, which relates to the magnetic flux output per unit volume. They are classified by letter N followed by two numbers.
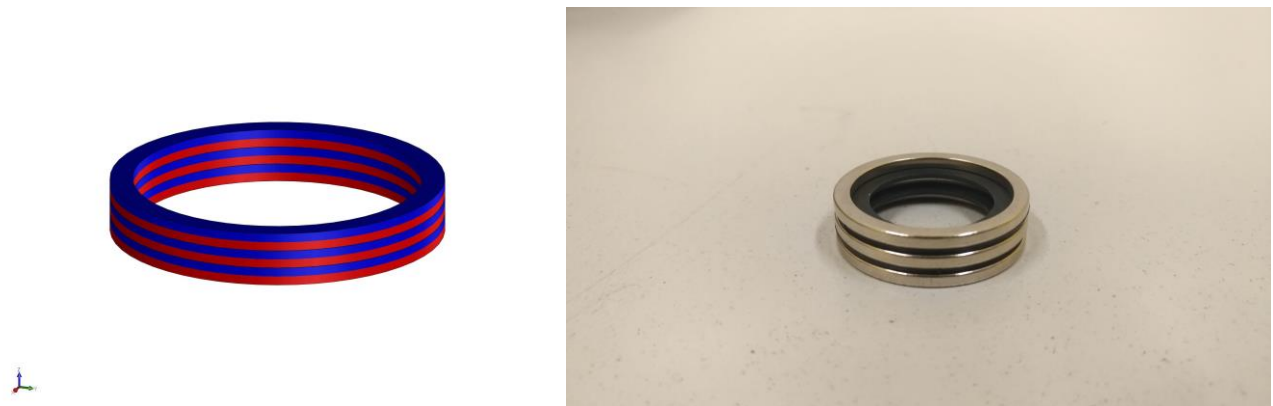

Figure 2.1.3.1 – Stator and rotor magnets.

2.1.4 Sapphire

Another important element of rotor is the sapphire. This is used as thrust bearing along a vertical axis because the magnetic forces reduce the weight force contribution without eliminating it.

The sapphire has been chosen as material because it has a high hardness (9 on the Mohs scale).
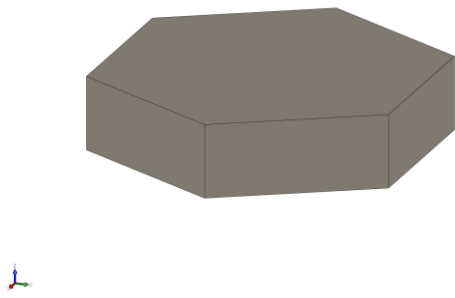
Figure 2.1.4.1 – Sapphire.

2.2 Possible configurations

The vertical magnetic rotor, which are analysed, has five different possible configurations based on the number of hubs and the number of permanent magnets mounted on the shaft.
By increasing the number of magnets, the forces exchanged between the stator and rotor are higher, with a minimum reduction of the rotor unit mass.

2.2.1 Case 1 – Rotor without hubs

Figure 2.2.1.2 shows a section of shaft with an only magnet. Here, in the place of the permanent magnets, there are Teflon spacers that are replaced by magnets in the other configurations.
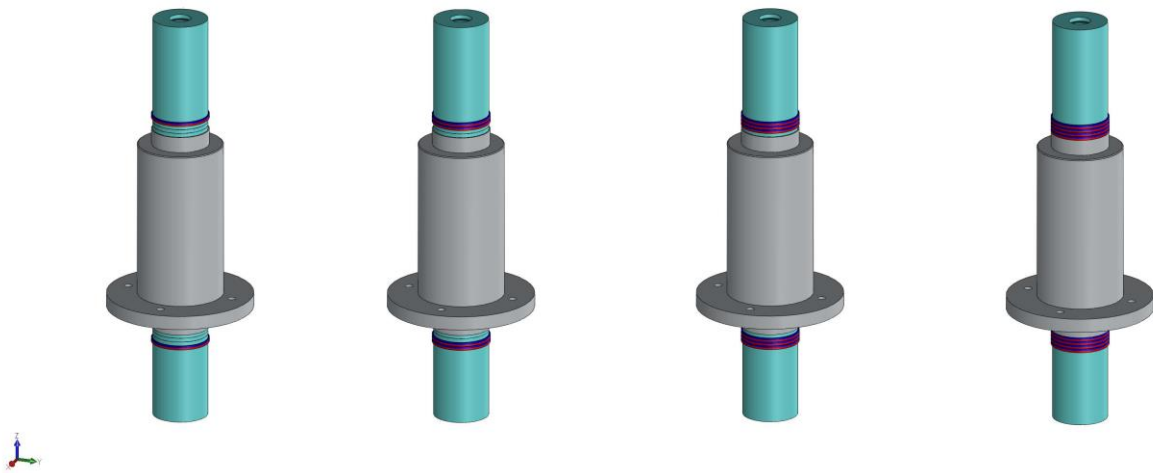
Figure 2.2.1.1 – Rotor without hubs with 1 magnet (in the upper left corner), 2 magnets (in the upper right corner), 3 magnets (in the lower left corner) and 4 magnets (in the lower right corner).
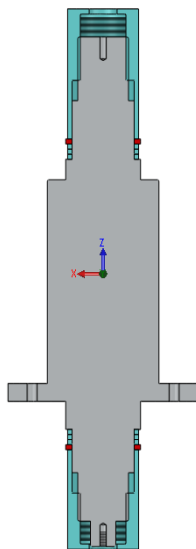
Figure 2.2.1.2 – Section of rotor with a magnet.

In Table 2.2.1.1 the most important characteristics of the rotor without hubs are listed. The centre of the mass is the same for all the cases with different number of magnets, while the moments of inertia change because a different mass with the increase of magnets.

Table 2.2.1.1 – Characteristics of the rotor without hubs.

Number of magnets	Mass [kg]	Centre of mass [m]			Moments of inertia [kg m^2]		
		X	Y	Z			
1	0.567	0	0	-0.0087	$1.196 \cdot 10^{-3}$	0	0
					0	$1.196 \cdot 10^{-3}$	0
					0	0	$0.151 \cdot 10^{-3}$
2	0.567	0	0	-0.0087	$1.193 \cdot 10^{-3}$	0	0
					0	$1.193 \cdot 10^{-3}$	0
					0	0	$0.151 \cdot 10^{-3}$
3	0.566	0	0	-0.0087	$1.191 \cdot 10^{-3}$	0	0
					0	$1.191 \cdot 10^{-3}$	0
					0	0	$0.151 \cdot 10^{-3}$
4	0.565	0	0	-0.0087	$1.190 \cdot 10^{-3}$	0	0
					0	$1.190 \cdot 10^{-3}$	0
					0	0	$0.151 \cdot 10^{-3}$

2.2.2 Case 2 – Rotor with a hubs

Figure 2.2.2.1 shows the four possible cases when there is only one hub on the shaft. The hub is into contact with the shaft flange and it is anchored to the flange with parallel pins hardened.
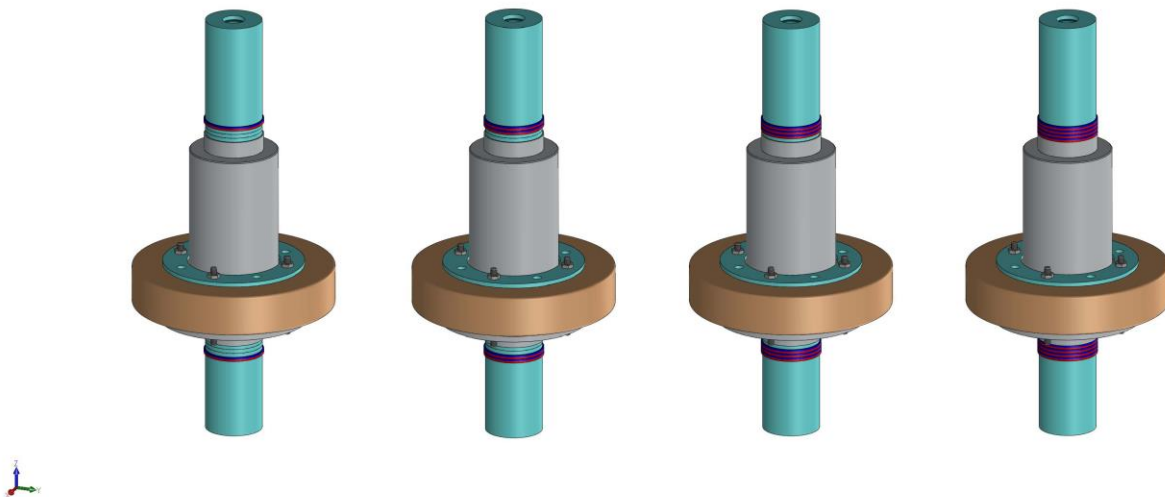

Figure 2.2.2.1 – Rotor with a hub with 1 magnet (in the upper left corner), 2 magnets (in the upper right corner), 3 magnets (in the lower left corner) and 4 magnets (in the lower right corner).

Adding new elements on the rotor group, has repercussions with increasing mass and about the moments of inertia.

Table 2.2.2.1 – Characteristics of the rotor with a hub.

Number of magnets	Mass [kg]	Centre of mass [m]			Moments of inertia [kg m^2]		
		X	Y	Z			
1	1.630	0	0	-0.024	$2.246 \cdot 10^{-3}$	0	0
					0	$2.246 \cdot 10^{-3}$	0
					0	0	$1.745 \cdot 10^{-3}$
2	1.629	0	0	-0.024	$2.243 \cdot 10^{-3}$	0	0
					0	$2.243 \cdot 10^{-3}$	0
					0	0	$1.744 \cdot 10^{-3}$
3	1.628	0	0	-0.024	$2.241 \cdot 10^{-3}$	0	0
					0	$2.241 \cdot 10^{-3}$	0
					0	0	$1.744 \cdot 10^{-3}$
4	1.627	0	0	-0.024	$2.238 \cdot 10^{-3}$	0	0
					0	$2.238 \cdot 10^{-3}$	0
					0	0	$1.744 \cdot 10^{-3}$

2.2.3 Case 3 – Rotor with two hubs

Similarly, to the cases analysed above, we proceed with the study of the characteristics of the rotor group with two hubs.
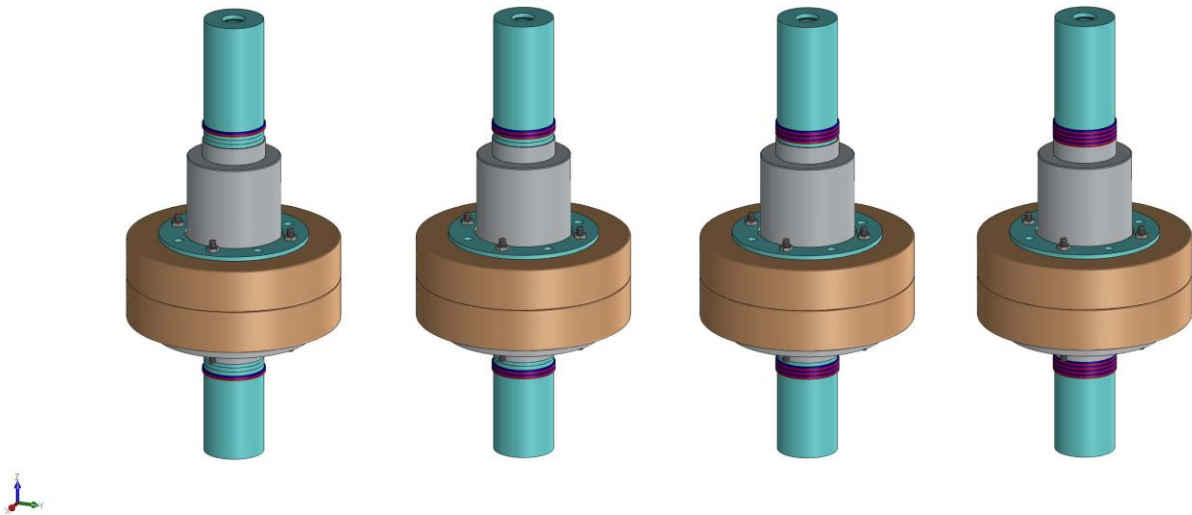

Figure 2.2.3.1 – Rotor with two hubs with 1 magnet (in the upper left corner), 2 magnets (in the upper right corner), 3 magnets (in the lower left corner) and 4 magnets (in the lower right corner).

Table 2.2.3.1 – Characteristics of the rotor with two hubs.

Number of magnets	Mass [kg]	Centre of mass [m]			Moments of inertia [kg m^2]		
		X	Y	Z			
1	2.686	0	0	-0.02	$3.162 \cdot 10^{-3}$	0	0

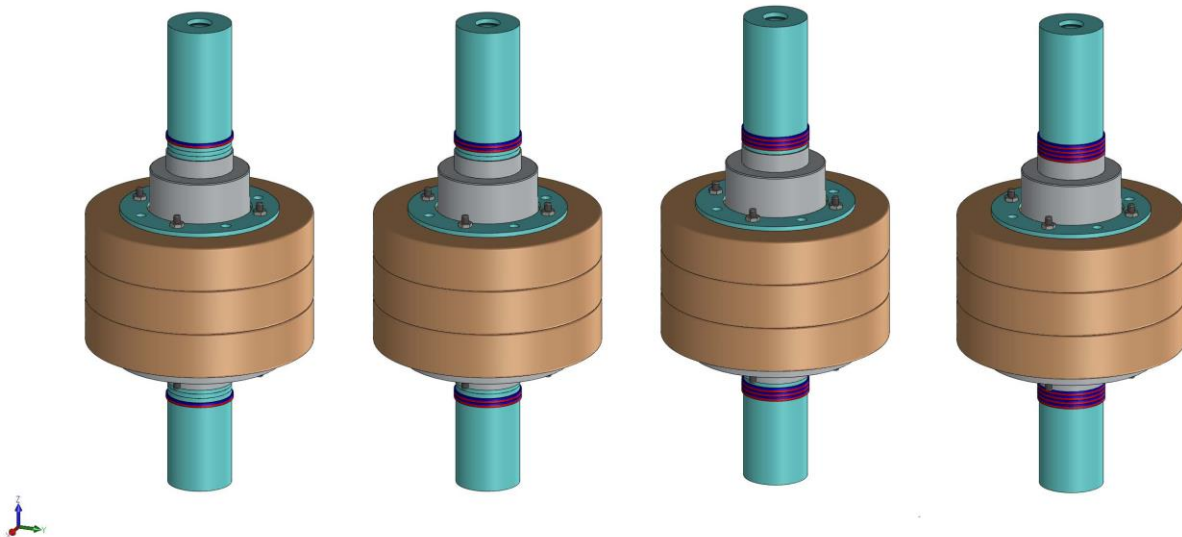| | | | | | 0 | $3.162\cdot10^{-3}$ | 0 |
					0	0	$3.333\cdot10^{-3}$
2	2.685	0	0	-0.02	$3.159\cdot10^{-3}$	0	0
					0	$3.159\cdot10^{-3}$	0
					0	0	$3.333\cdot10^{-3}$
3	2.685	0	0	-0.02	$3.157\cdot10^{-3}$	0	0
					0	$3.157\cdot10^{-3}$	0
					0	0	$3.332\cdot10^{-3}$
4	2.684	0	0	-0.02	$3.155\cdot10^{-3}$	0	0
					0	$3.155\cdot10^{-3}$	0
					0	0	$3.332\cdot10^{-3}$

2.2.4 Case 4 – Rotor with three hubs

Figure 2.2.4.1 – Rotor with three hubs with 1 magnet (in the upper left corner), 2 magnets (in the upper right corner), 3 magnets (in the lower left corner) and 4 magnets (in the lower right corner).

Table 2.2.4.1 – Characteristics of the rotor with three hubs.

Number of magnets	Mass [kg]	Centre of mass [m]			Moments of inertia [kg m²]		
		X	Y	Z			
1	3.743	0	0	-0.012	$4.546\cdot10^{-3}$	0	0
					0	$4.546\cdot10^{-3}$	0
					0	0	$4.921\cdot10^{-3}$
2	3.742	0	0	-0.012	$4.543\cdot10^{-3}$	0	0
					0	$4.543\cdot10^{-3}$	0
					0	0	$4.921\cdot10^{-3}$
3	3.741	0	0	-0.012	$4.541\cdot10^{-3}$	0	0
					0	$4.541\cdot10^{-3}$	0

Number of magnets	Mass [kg]	X	Y	Z	Moments of inertia [kg m²]		
					0	0	$4.921 \cdot 10^{-3}$
4	3.741	0	0	-0.012	$4.539 \cdot 10^{-3}$	0	0
					0	$4.539 \cdot 10^{-3}$	0
					0	0	$4.921 \cdot 10^{-3}$

2.2.5 Case 5 – Rotor with four hubs
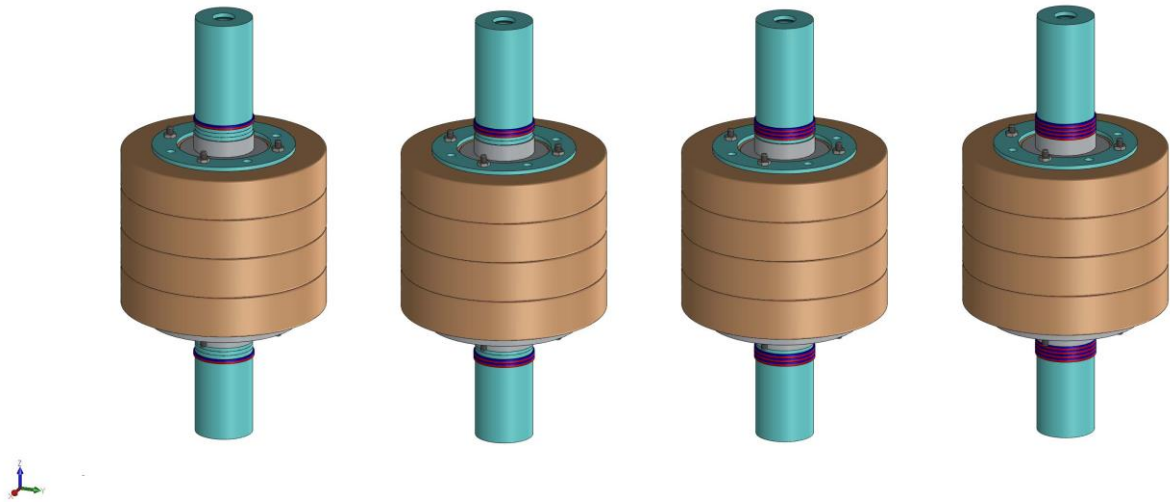
Figure 2.2.5.1 – Rotor with four hubs with 1 magnet (in the upper left corner), 2 magnets (in the upper right corner), 3 magnets (in the lower left corner) and 4 magnets (in the lower right corner).

Table 2.2.5.1 – Characteristics of the rotor with four hubs.

Number of magnets	Mass [kg]	Centre of mass [m]			Moments of inertia [kg m²]		
		X	Y	Z			
1	4.799	0	0	-0.004	$6.655 \cdot 10^{-3}$	0	0
					0	$6.655 \cdot 10^{-3}$	0
					0	0	$6.509 \cdot 10^{-3}$
2	4.799	0	0	-0.004	$6.652 \cdot 10^{-3}$	0	0
					0	$6.652 \cdot 10^{-3}$	0
					0	0	$6.509 \cdot 10^{-3}$
3	4.798	0	0	-0.004	$6.650 \cdot 10^{-3}$	0	0
					0	$6.650 \cdot 10^{-3}$	0
					0	0	$6.509 \cdot 10^{-3}$
4	4.797	0	0	-0.004	$6.648 \cdot 10^{-3}$	0	0
					0	$6.648 \cdot 10^{-3}$	0
					0	0	$6.509 \cdot 10^{-3}$

2.3 Chosen configuration

Among many possible configurations, it is decided to place four hubs and four magnets on the vertical rotor because the goal to achieve is to maximize the level of energy to be stored.
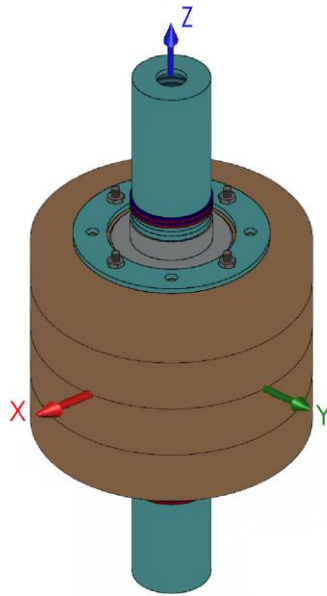
Figure 2.3.1 – Rotor with four hubs with four magnets.

Table 2.3.1 – Characteristics of the rotor in chosen configuration.

Number of magnets	Mass [kg]	Centre of mass [m]			Moments of inertia [kg m²]		
		X	Y	Z			
4	4.798	0	0	-0.004	$6.657 \cdot 10^{-3}$	0	0
					0	$6.657 \cdot 10^{-3}$	0
					0	0	$6.509 \cdot 10^{-3}$

3. Simulation of the interaction between permanent magnets

Permanent magnets are widely used for the realization of technological components that require enhanced magnetic characteristics. In this thesis work, the magnets are used as bearings and therefore it is inherent to evaluate the magneto-elastic force developed between stator rings and rotor rings.

Permanent magnets are unique in their ability to deliver magnetic flux into the airgap of a magnetic circuit without any continuous expenditure of energy. The flux density may be uniform or nonuniform, steady or time varying. Magnet applications can also be classified by their influence on the magnet or by the physical effect that is being exploited.

Spatially nonuniform fields offer another series of potentially useful effects.

Through the knowledge of the local distribution of the magnetic field, it is possible to evaluate magneto-mechanical couplings between similar-shaped permanent magnets. The local magnetic force of a volume unit results:

$$\mathbf{F} = \mathbf{M} \cdot \nabla \mathbf{B} \tag{3.1}$$

whereas the volume unit momentum is

$$\mathbf{T} = \mathbf{M} \wedge \mathbf{B} \tag{3.2}$$

where $\mathbf{M}$ is residual magnetization vector and $\mathbf{B}$ is magnetic flux density vector.
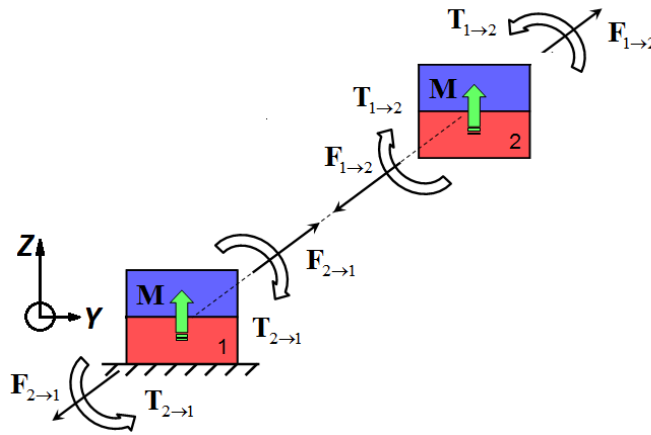

Figure 3.1 – Free body scheme of two magnets.

Applying the equations of the magnetic interaction are calculated the forces and the torques on the magnet 2 due to the magnetic field generated by the magnet 1 (Equations 3.3 and 3.4);

$$\mathbf{F}_{1\rightarrow 2} = \mathbf{M}_2 \cdot \nabla \mathbf{B}_1 = -\mathbf{M}_1 \cdot \nabla \mathbf{B}_2 \tag{3.3}$$

$$\mathbf{T}_{1\rightarrow 2} = \mathbf{M}_2 \wedge \mathbf{B}_1 = -\mathbf{M}_1 \wedge \mathbf{B}_2 \tag{3.4}$$

$$\mathbf{F}_{1\rightarrow 2} = \int_{vol,2} \mathbf{M}_2 \cdot \nabla \mathbf{B}_1 \, dvol = -\int_{vol,1} \mathbf{M}_1 \cdot \nabla \mathbf{B}_2 \, dvol \tag{3.5}$$

$$\mathbf{T}_{1\rightarrow 2} = \int_{vol,2} \mathbf{M}_2 \wedge \mathbf{B}_1 \, dvol = -\int_{vol,1} \mathbf{M}_1 \wedge \mathbf{B}_2 \, dvol \tag{3.6}$$

For simplicity, let's examine a generic parallelepiped-shaped magnet sketched in Figure 3.2. This magnet has dimensions 2a, 2b, 2c and residual magnetic induction $\mathbf{B_r} = \mu_0 \cdot \mathbf{M}$, where $\mu_0 = 4 \cdot \pi \cdot 10^{-7} \frac{H}{m}$ is the magnetic permeability of vacuum and $\mathbf{M}$ is the residual magnetization, arranged along the z axis.
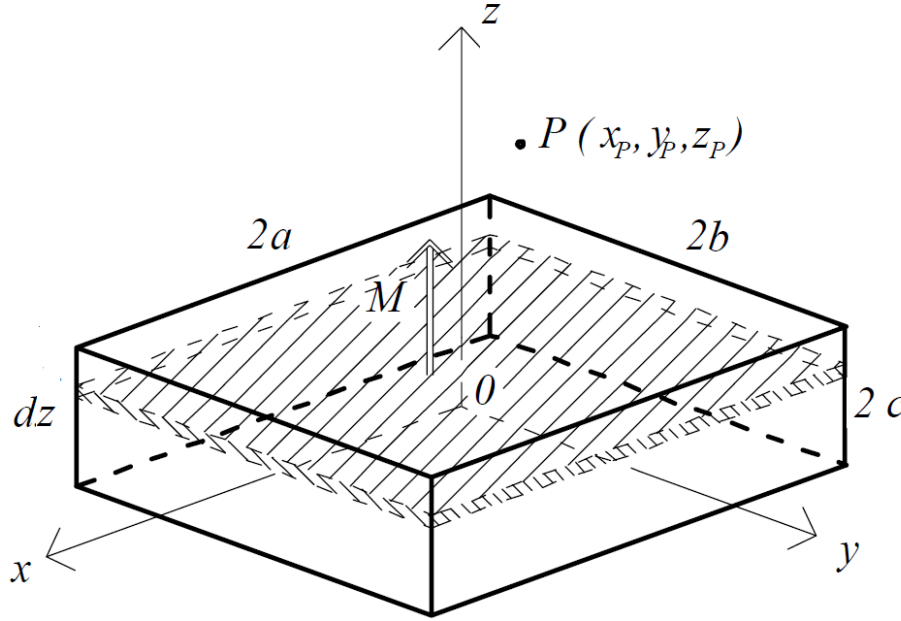

Figure 3.2 – Geometric characteristics of the permanent magnet

The magnetic interaction forces are evaluated along the three main directions:

$$F_{1\rightarrow2,x} = \left(M_{x,2} \frac{\partial B_{x,1}}{\partial x} + M_{y,2} \frac{\partial B_{x,1}}{\partial y} + M_{z,2} \frac{\partial B_{x,1}}{\partial z} \right) \tag{3.7}$$

$$F_{1\rightarrow2,y} = \left(M_{x,2} \frac{\partial B_{y,1}}{\partial x} + M_{y,2} \frac{\partial B_{y,1}}{\partial y} + M_{z,2} \frac{\partial B_{y,1}}{\partial z} \right) \tag{3.8}$$

$$F_{1\rightarrow2,z} = \left(M_{x,2} \frac{\partial B_{z,1}}{\partial x} + M_{y,2} \frac{\partial B_{z,1}}{\partial y} + M_{z,2} \frac{\partial B_{z,1}}{\partial z} \right) \tag{3.9}$$

$$T_{1\rightarrow2,x} = M_{y,2} B_{z,1} - M_{z,2} B_{y,1} \tag{3.10}$$

$$T_{1\rightarrow2,y} = M_{z,2} B_{x,1} - M_{x,2} B_{z,1} \tag{3.11}$$

$$T_{1\rightarrow2,z} = M_{x,2} B_{y,1} - M_{y,2} B_{x,1} \tag{3.12}$$

These forces can be compared to elastic forces and therefore only the linear component is able to evaluate the rigidity through equations 3.13, 3.14 and 3.15.

$$K_{xx} = -\frac{dF_x}{dx} \tag{3.13}$$

$$K_{yy} = -\frac{dF_y}{dy} \tag{3.14}$$

$$K_{zz} = -\frac{dF_z}{dz} \tag{3.15}$$

These parameters are important for evaluating the stability or instability of an axis because it is well known that stable passive magnetic levitation is impossible except for a few cases: such result is commonly referred to as the Earnshaw's theorem, even if the original paper by S. Earnshaw dealt with the equilibrium of systems of particles governed by inverse square law forces [3] and the proof of instability was extended to a ferromagnetic or paramagnetic body in a magnetic field only about a century later by W. Braunbeck [4][5].

The above equations have been implemented in Matlab to obtain the trend of forces, torques and stiffness as a function of the displacement of one of the two magnets.

3.1 Case 1 – Interaction between two prisms

Simulation features:
- two prismatic magnets,
- moving a manet along the z axis,
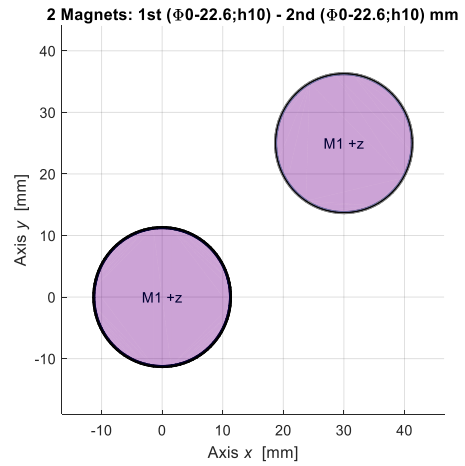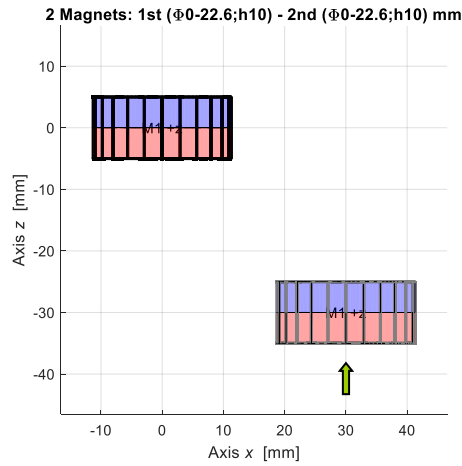- offset in the x and y directions.
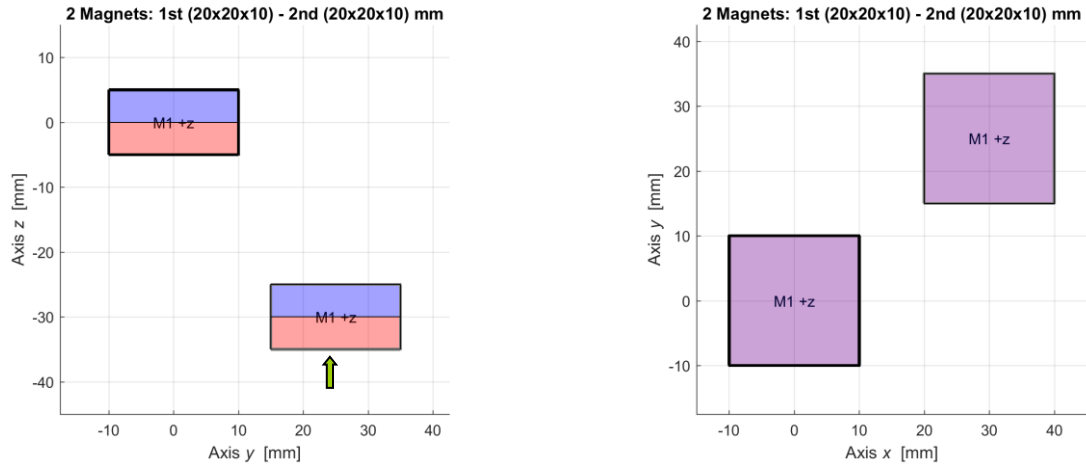
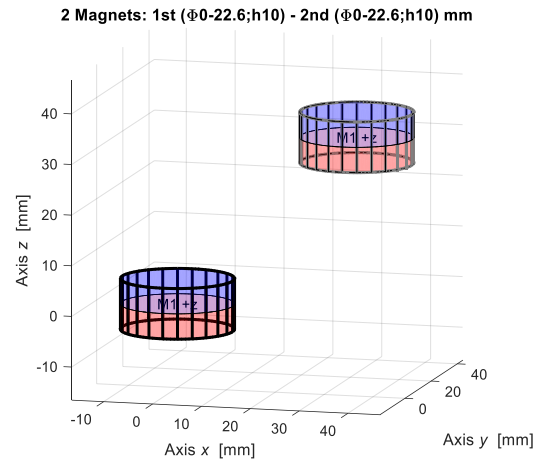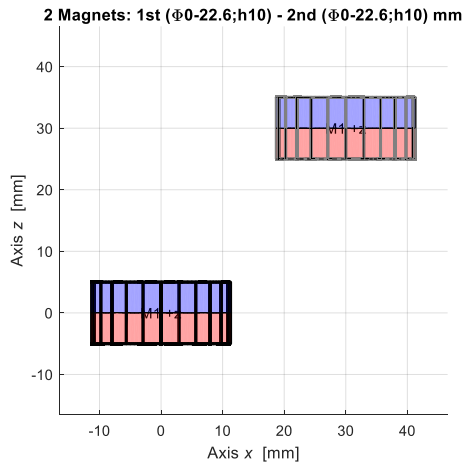Figure 3.1.1 – Initial configuration case 1.
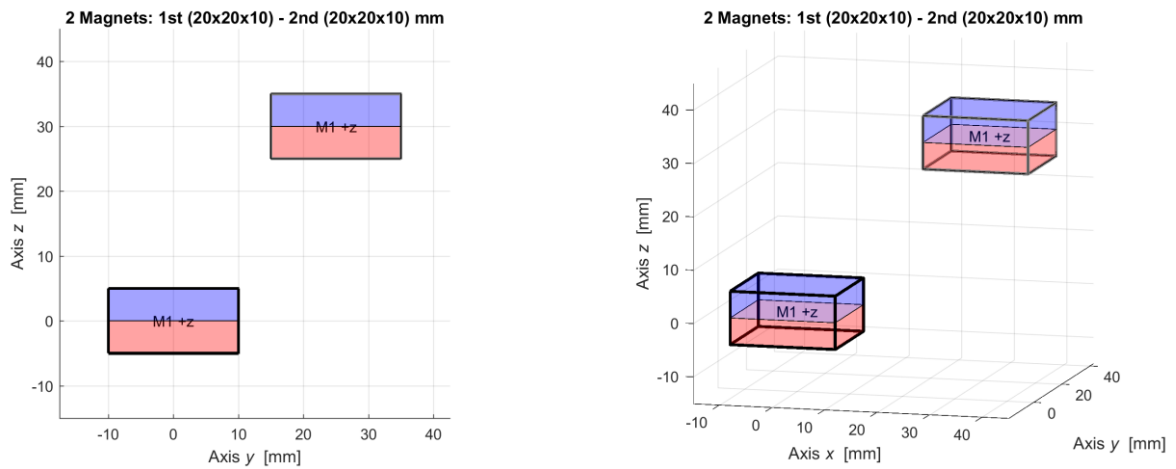
Figure 3.1.2 – Final configuration case 1.

Table 3.1.1 – Properties of the material and the geometric characteristics.

Characteristic	Property	Value
Geometry	$2a$, size along x [mm]	20
	$2b$, size along y [mm]	20
	$2c$, height along z, magnetization axis [mm]	10
Material	B_r, residual magnetic induction [T]	1.2
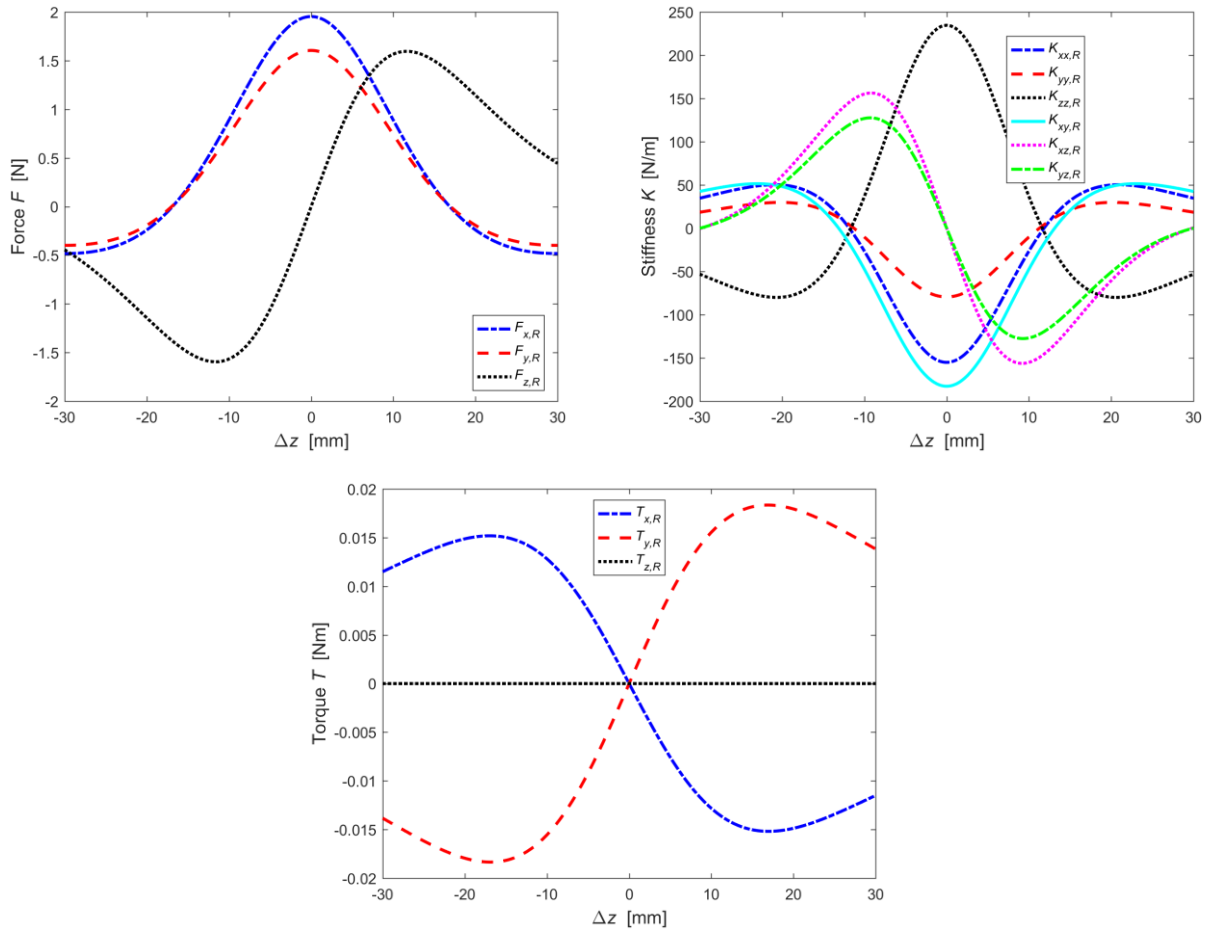
Figure 3.1.3 – Forces, stiffnesses and torques in case1.

The two prismatic magnets have a positive pitch both in the x direction and in the y direction. In this case, the magnet 2 is moved along the z direction, maintaining the two constant misalignments. Considering the configuration in which the two magnets are at the same height, corresponding to the position $\Delta z = 0$. The force along the z direction will be zero, while the forces along the x and y directions will both be positive, i.e. the magnet 2 will tend to move away from the magnet 1.

3.2 Case 2 – Interaction between two cylindrical magnets

Similarly, to what has been studied in the previous paragraph, the force formulas, stiffnesses and torques were implemented through Matlab.

Simulation features:
- two prismatic magnets,
- moving a manet along the z axis,
- offset in the x and y directions.

Figure 3.2.1 – Initial configuration case 2.

Figure 3.2.2 – Final configuration case 2.

Table 3.2.1 – Properties of the material and the geometric characteristics.

Characteristic	Property	Value
Geometry	$\varnothing$, diametrical size [mm]	22.6
	$2c$, height along z, magnetization axis [mm]	10
Material	B_r, residual magnetic induction [T]	1.2

In this case, the same offset values and the same value of displacement of the magnet 2 have been of the previous case assigned.

Furthermore, the diameter of the cylinder has been obtained in such a way that the same volume of the parallelepiped has the same height. This feature is very important as it allows us to obtain the strengths, stiffnesses and torques equal to those obtained in Case 1.
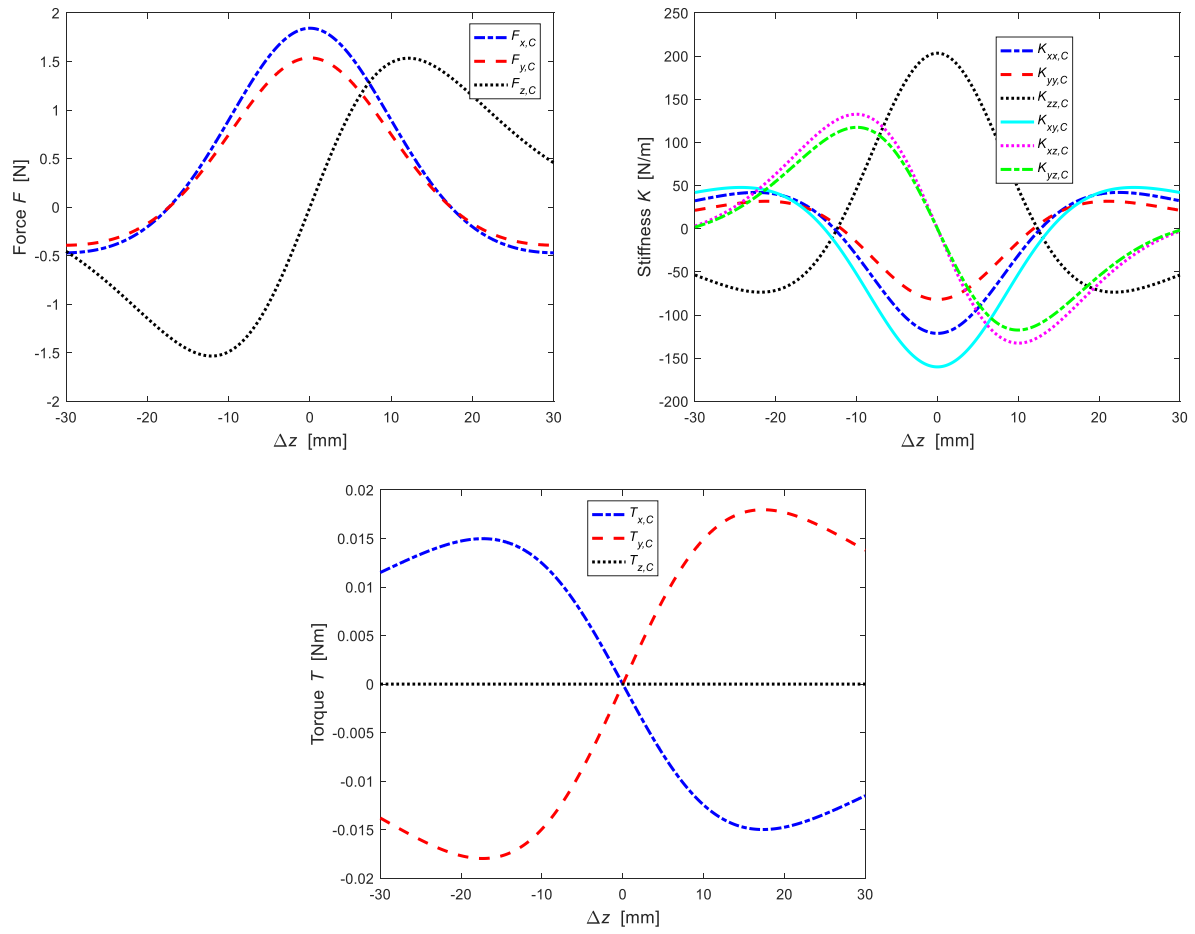
Figure 3.2.3 – Forces, stiffnesses and torques in case 2.

The trend of forces, stiffnesses and torques is the same for two different geometries and this allows us to assert that the quantities examined do not depend on the geometry of the treated body.

4. Interaction between prismatic magnetic rings

Considering the equality of the results obtained between two magnets of different shapes, we can hypothesize to calculate the interaction between circular magnetic rings such as that between rings of prismatic shape. The geometric characteristics of the magnetic rings can be found in Table 4.1.

Table 4.1 – Properties of the material and geometric characteristics of the circular magnetic rings.

Characteristic	Property	Value
Geometry1 – Stator rings	$2h$, height along z, magnetization axis [mm]	2
	$\varnothing_{ext.}$-$\varnothing_{int}$, diametrical size [mm]	37-32
Geometry 2 – Rotor rings	$2h$, height along z, magnetization axis [mm]	2
	$\varnothing_{ext.}$-$\varnothing_{int}$, diametrical size [mm]	29.5-24.5
Material	B_r, residual magnetic induction [T]	1.2

The analogy with the prismatic rings can only be applied if the magnets have the same volume and height. We will obtain therefore the geometrical characteristics reported in Table 4.2.

Table 4.2 – Properties of the material and geometric characteristics of the prismatic magnetic rings.

Characteristic	Property	Value
Geometry1 – Stator rings	$2c$, height along z, magnetization axis [mm]	2
	$2a_{ext}$-$2a_{int}$, size along x [mm]	32.8-28.4
	$2b_{ext}$-$2b_{int}$, size along y [mm]	32.8-28.4
Geometry 2 – Rotor rings	$2h$, height along z, magnetization axis [mm]	2
	$2a_{ext}$-$2a_{int}$, size along x [mm]	26.1-21.7
	$2b_{ext}$-$2b_{int}$, size along y [mm]	26.1-21.7
Material	B_r, residual magnetic induction [T]	1.2

4.1   Case 1 – Simulation of two magnets with axial displacement

4.1.1   Magneti con asse di magnetizzazione nello stesso verso

Simulation features:
- prismatic magnetic rings,
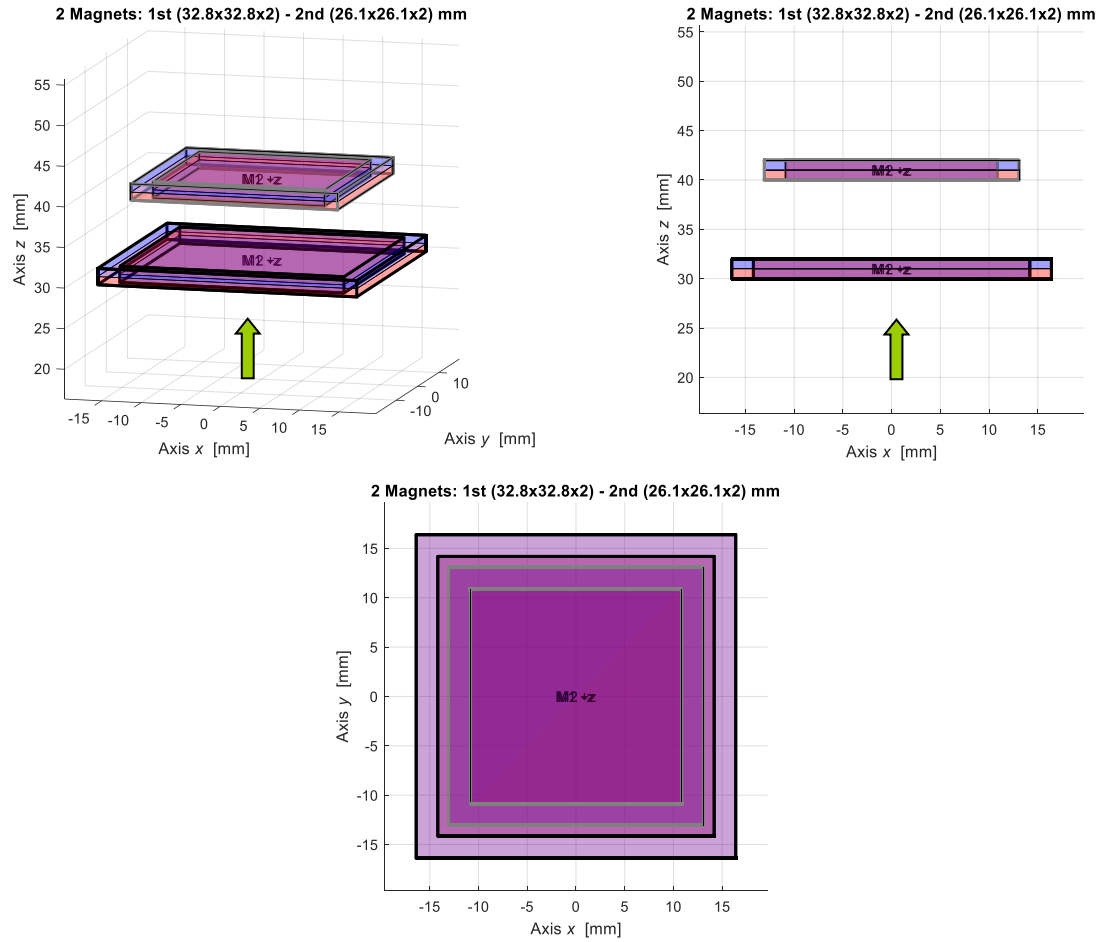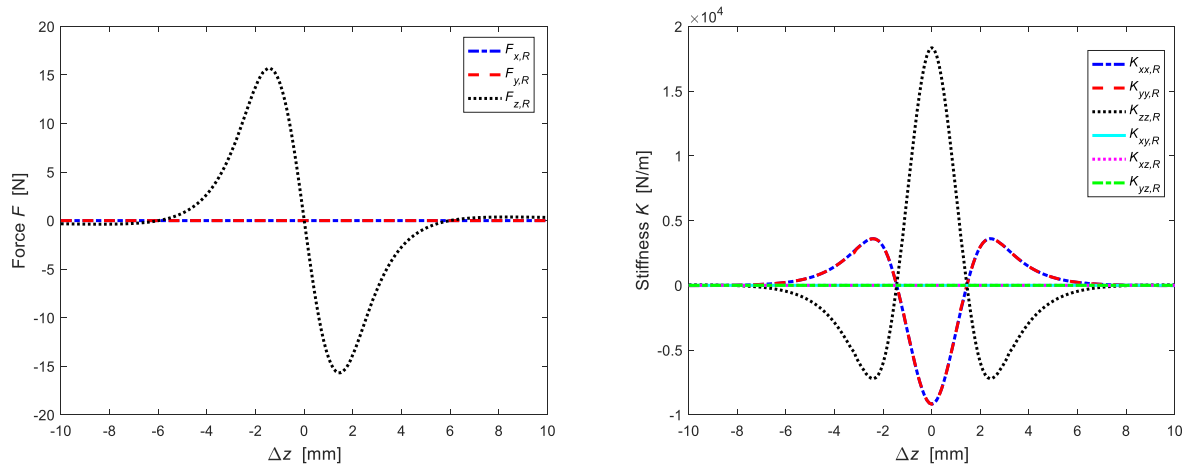- stator magnet moved along the z axis,
- no offset.

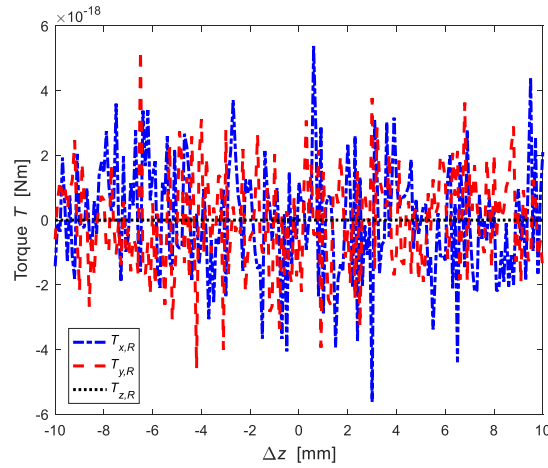Figure 4.1.1.1 – Initial configuration between two prismatic magnetic rings.

Figure 4.1.1.2 – Forces, stiffnesses and torques of magnetic interaction between two rings.

4.1.2 Analysis of the possible work areas

One of the peculiar characteristics of the magnetic rotor planned, is the presence of the minimum contribution of the weight force on the vertical axis. This is made possible by applying two axial forces in an opposite direction to the weight force acting on the rotor magnets generated by the magnetic fields of the stator magnets.

For this reason, the negative traits of the curve (the areas in red) will be excluded because they produce axial forces that agree with the weight force.
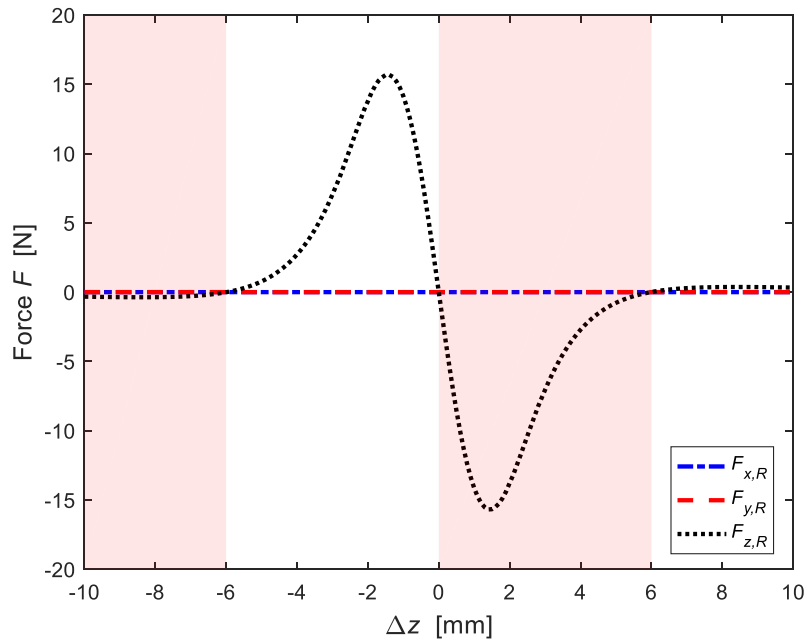
Figure 4.1.2.1 – Work areas in case 1.

The stability of the system also places limits on the positioning of the stator rings with respect to the rotor rings. Moreover, in order to obtain a considerable reduction of the vertical component, it is necessary to work in axial instability and radial stability.

To analyse instability, we use the Earnshaw theorem [2] where:

$$\nabla^2 B = 0 \tag{4.1}$$

$$\frac{\partial^2 B_x}{\partial x^2} + \frac{\partial^2 B_y}{\partial y^2} + \frac{\partial^2 B_z}{\partial z^2} = 0 \tag{4.2}$$

This equation can be rewritten as the sum of the stiffness along the three main directions.

$$k_{xx} + k_{yy} + k_{zz} = 0 \tag{4.3}$$

It is possible to notice how the stability condition occurs with stiffnesses less than zero. Therefore, the axial instability zones can be identified in those in which the stiffness along the vertical axis is positive and therefore the other stiffnesses are negative.
This reduces the possible areas in which to position the stator (in the green areas there is axial stability).
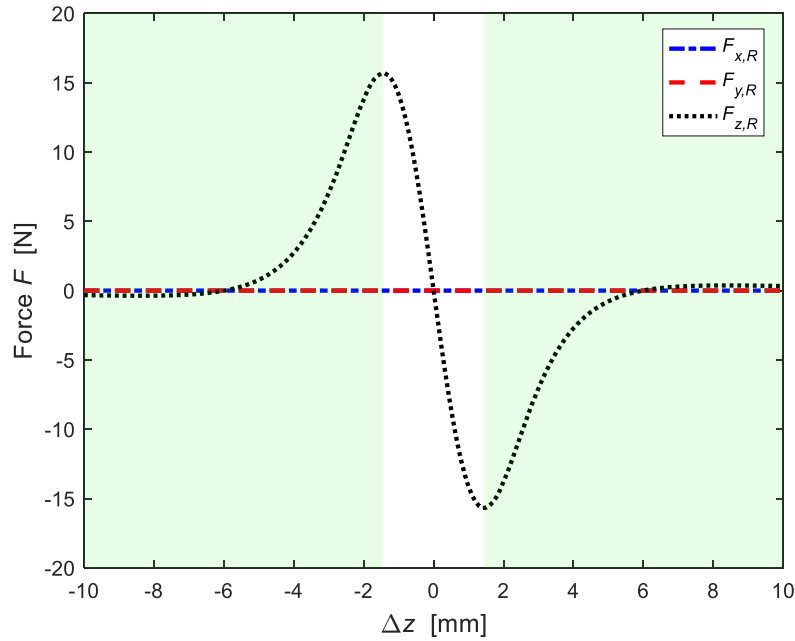
Figure 4.1.2.2 – Zone of the possible positioning of the rotor ring.

With the use of only one magnet, there are no limitations due to the space requirements and therefore almost all the path available on the stator could be used.
In conclusion, it is possible to position the stator only in the white part of the graph in Figure 4.1.2.3, i.e. in a range between [-1.45 ÷ 0] mm.
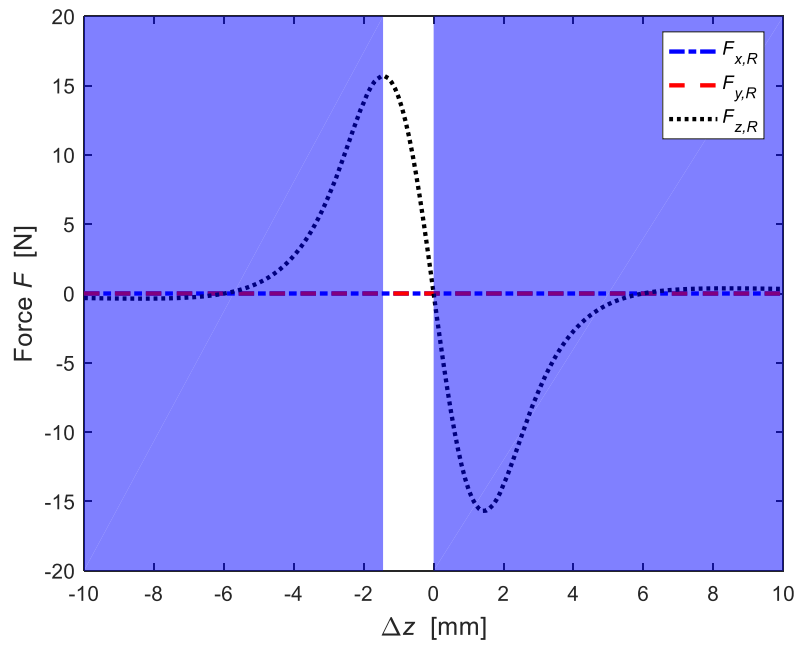
Figure 4.1.2.3 – Positioning areas of stator ring.

4.2 Case 2 - Simulation of four magnets with axial displacement

4.2.1 Magnets with magnetizing axis in the same direction

Simulation features:
- prismatic magnetic rings,
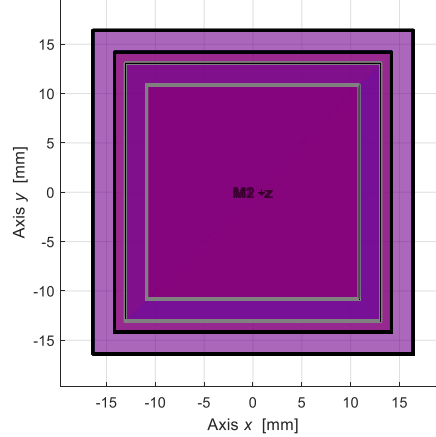- stator magnet moved along the z axis,
- no offset.
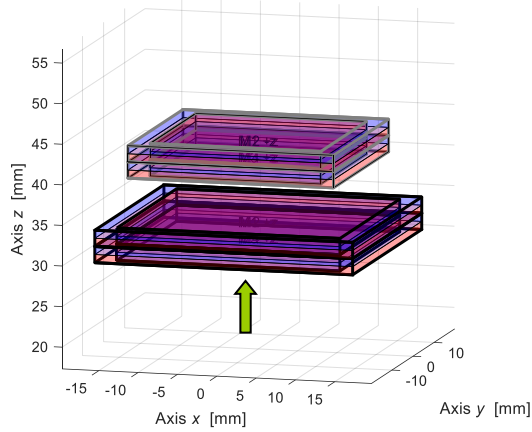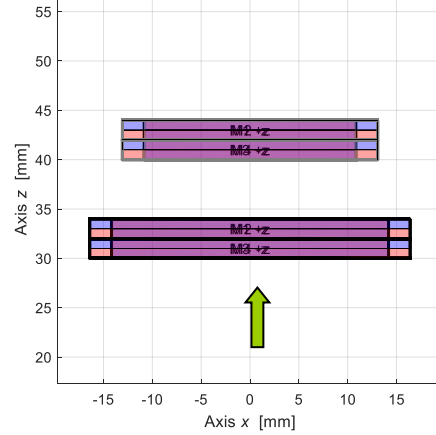
Figure 4.2.1.1 – Initial configuration between two rotor rings and two stator rings.
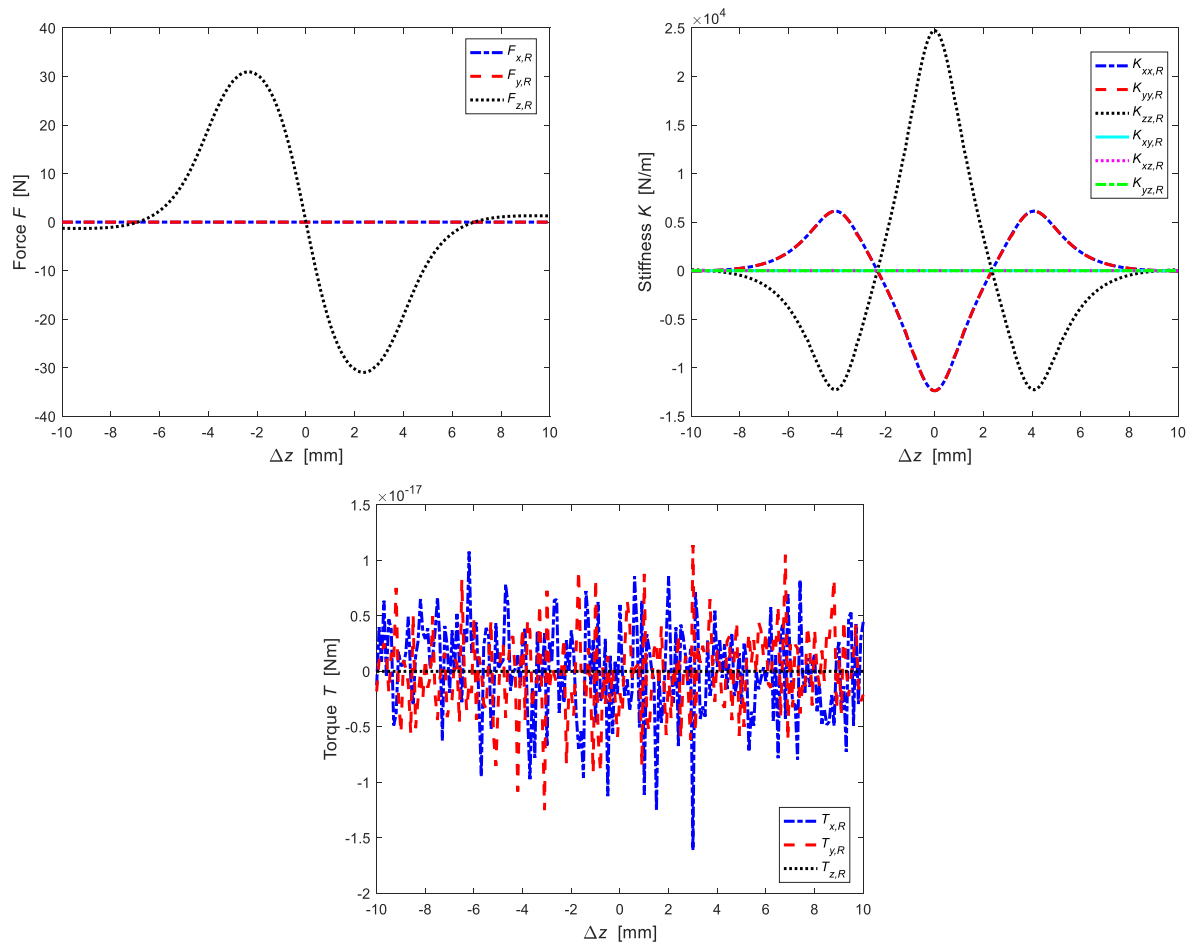
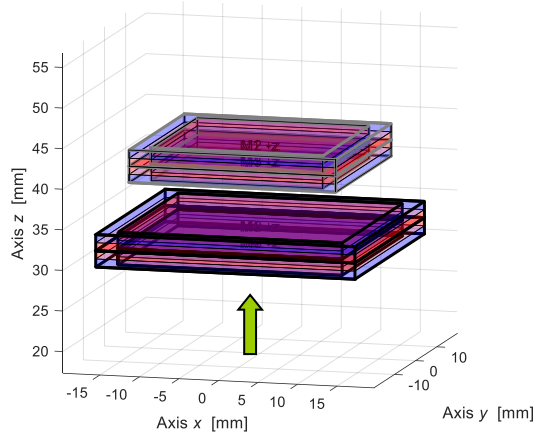Figure 4.2.1.2 – Forces, stiffnesses and torques for case 2.

4.2.2 Magnets with magnetizing axis with alternating direction

Simulation features:
- prismatic magnetic rings,
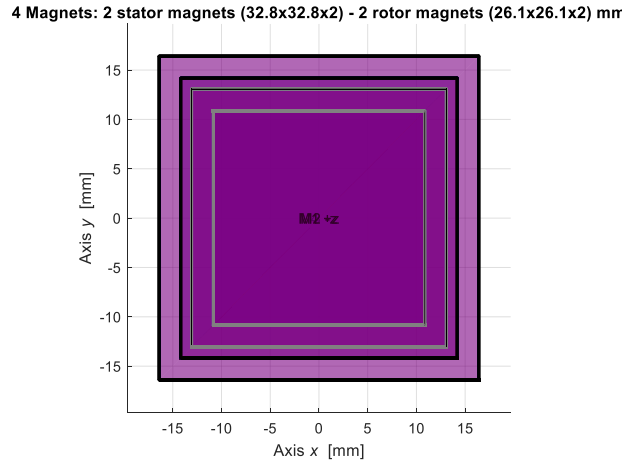- stator magnet moved along the z axis,
- no offset.
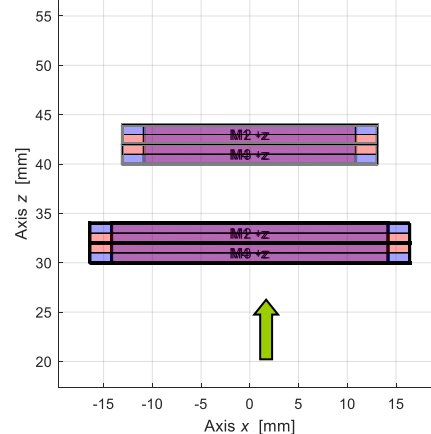
Figure 4.2.2.1 – Initial configuration between two rotor rings and two stator rings.
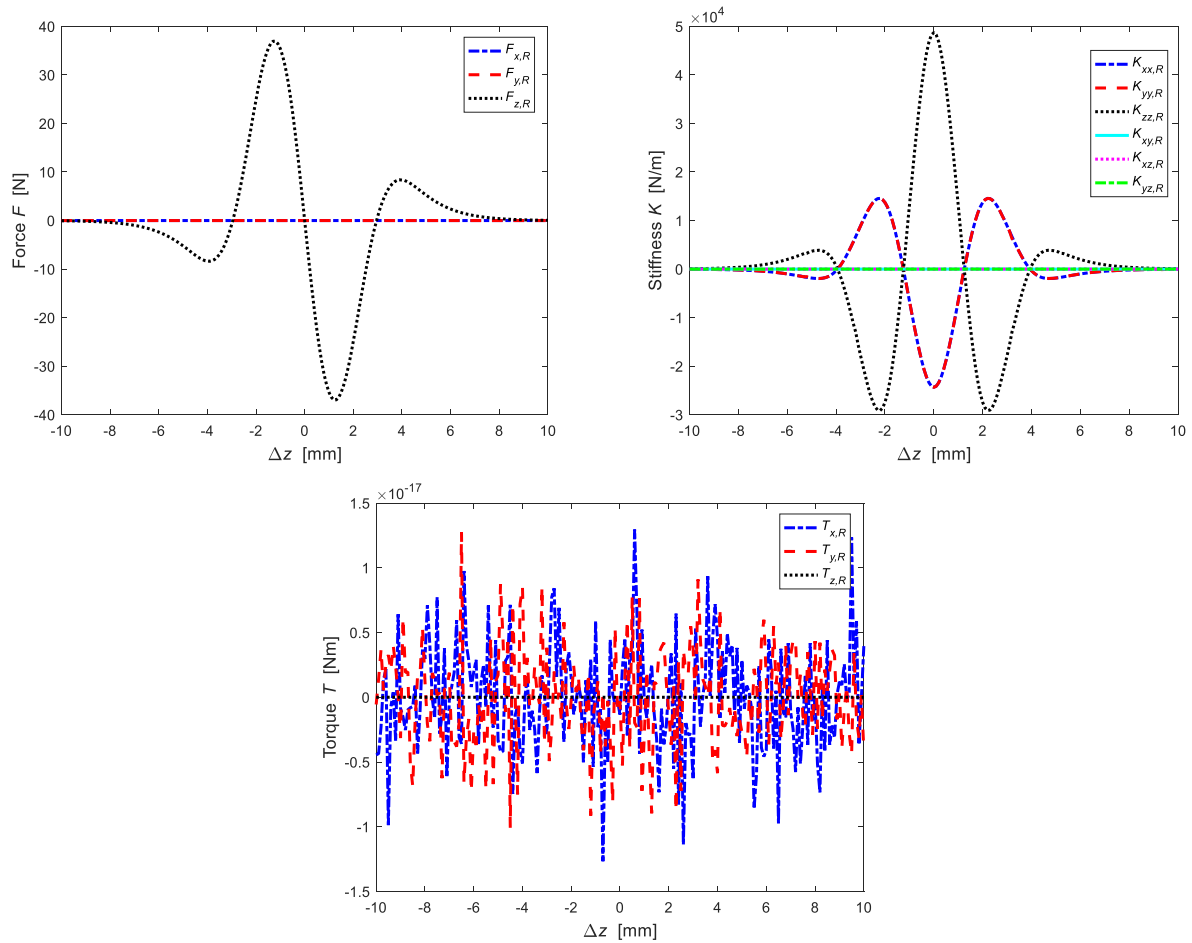

Figure 4.2.2.2 – Forces, stiffnesses and torques with rings with alternating magnetization axis.

4.2.3 Analysis of the possible work areas

Similarly, to what has been seen previously, the position of the stator rings is chosen following three limitations.

To minimize the weight force only the positive forces are considered as shown in Figure 4.2.3.1
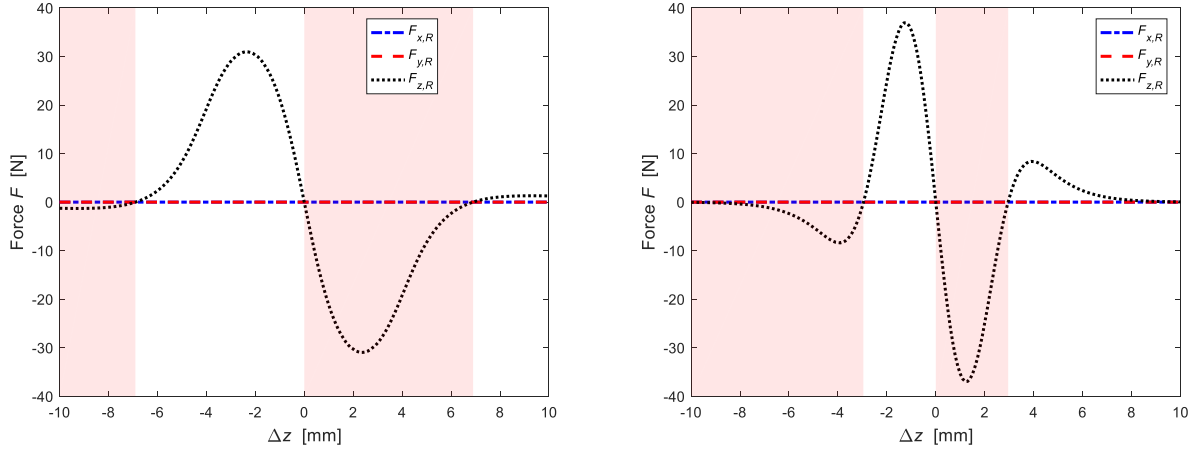
Figure 4.2.3.1 – Work areas in the case of two rings with a residual magnetic induction vector agreement (left) and alternating discordant (right).

It was decided to work in areas where there is an axial instability and for this reason the areas with negative stiffness (green areas in Figure 4.2.3.2) are not considered.
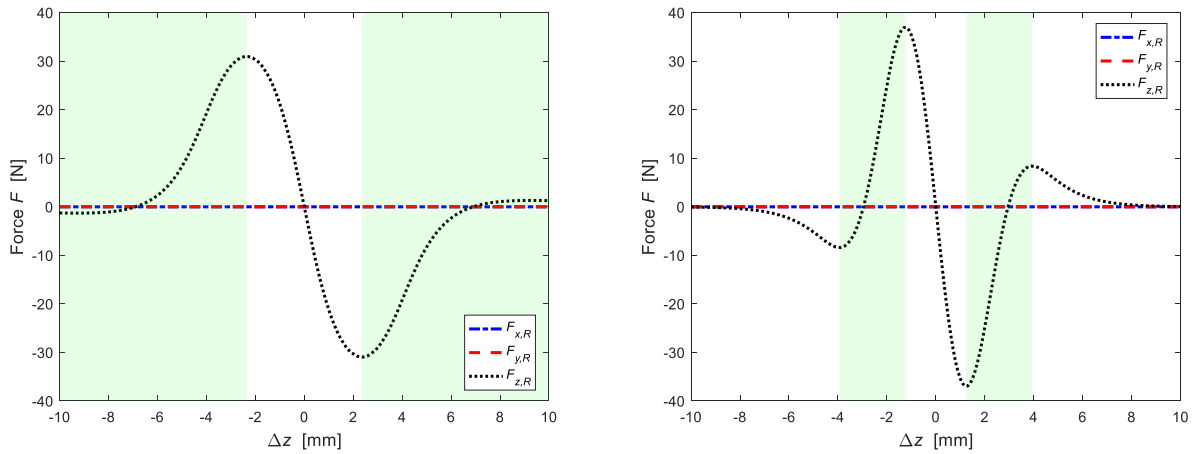

Figure 4.2.3.2 – Zones where it is possible to position the rotor in the case of rings with the vector residual magnetic induction agreement (left) and alternating discord (right).

With the configuration of two stator and rotor rings, there are no geometric limitations. Therefore, the optimal zones where to place the stator rings are given by the overlapping of the two previous graphs. Therefore, we obtain the graph in Figure 4.2.3.3 where the blank areas are the only ones usable.

There are different working ranges for the different orientation of the magnetic rings. If the magnets are all arranged with the residual magnetization vector in the same direction, there is a zone between [-2.35 ÷ 0] mm; while if the magnets arranged in alternate direction there are two ranges between [-1.24 ÷ 0] mm and [3.94 ÷ 10] mm where there is only a small contribution of axial force.
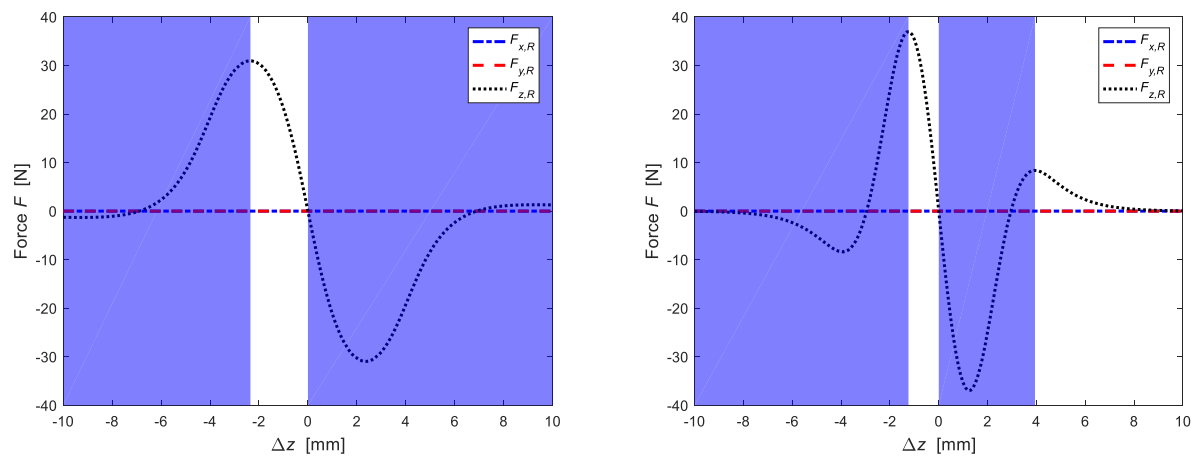
Figure 4.2.3.3 – Positioning zones of the stator ring in two cases under examination.

4.3 Case 3 - Simulation of six magnets with axial displacement

4.3.1 Magnets with magnetizing axis in the same direction

Simulation features:
- prismatic magnetic rings,
- stator magnet moved along the z axis,
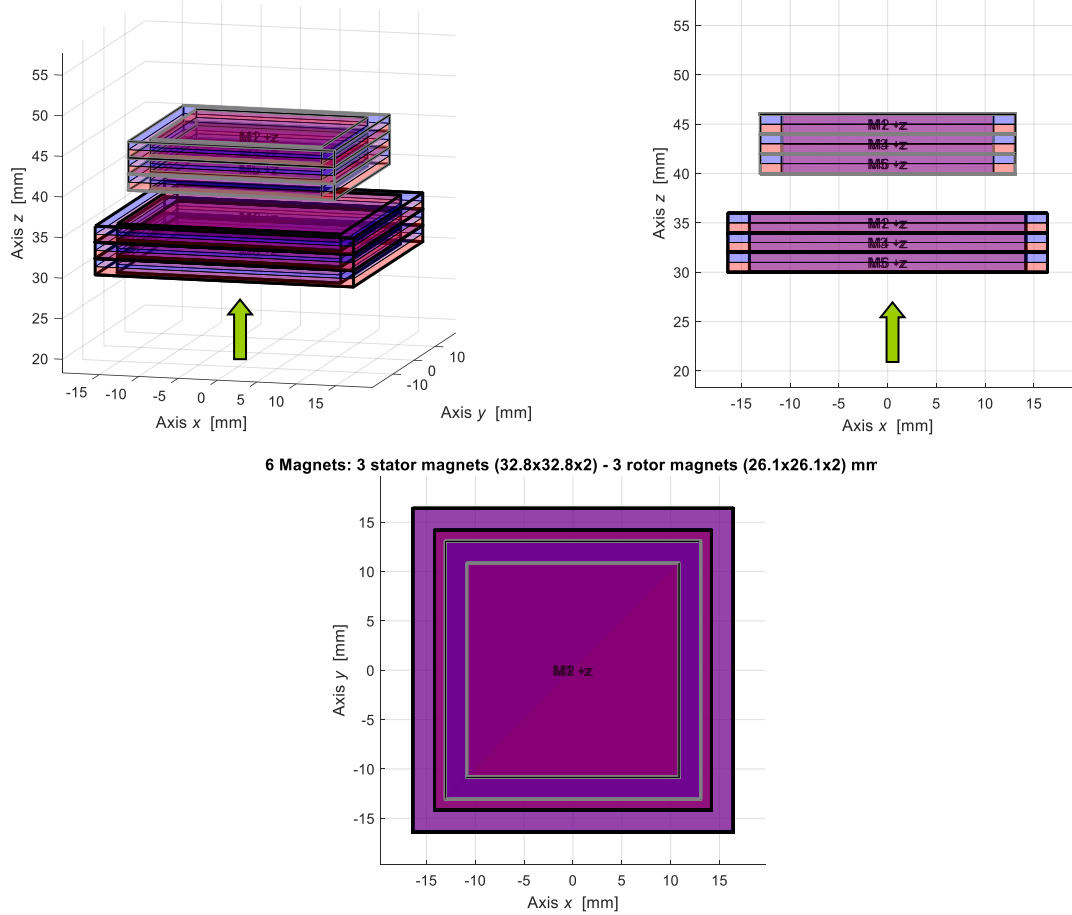- no offset.

Figure 4.3.1.1 – Initial configuration between three rotor rings and three stator rings.
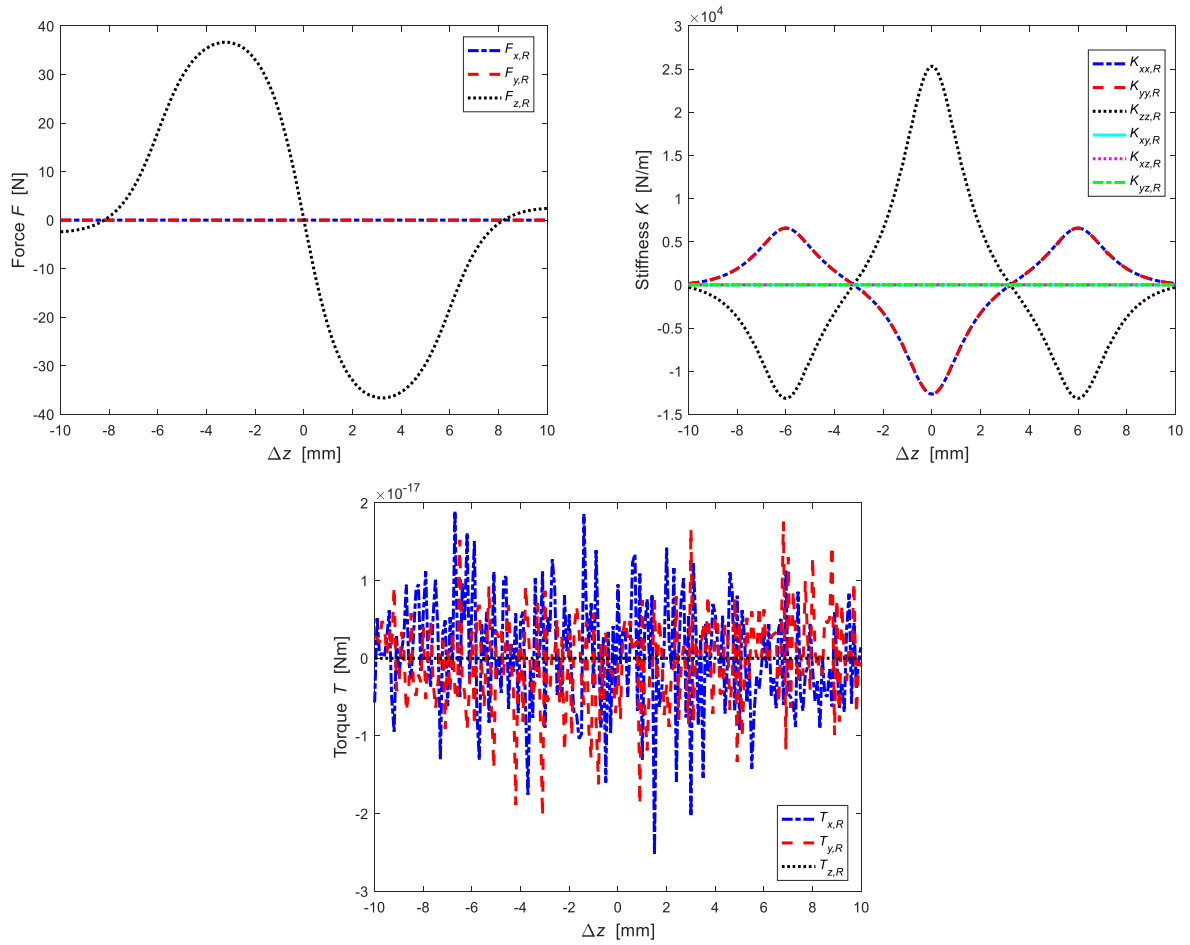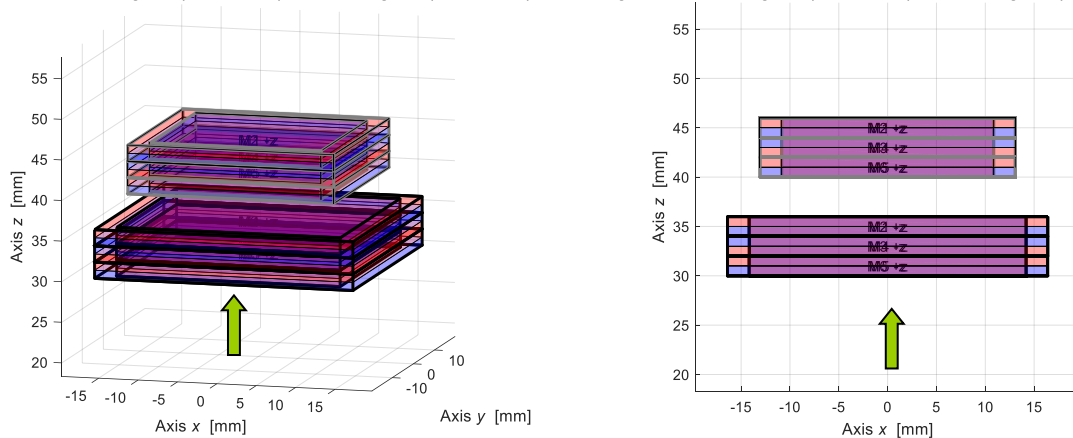
Figure 4.3.1.2 – Forces, stiffnesses and torques.

4.3.2 Magnets with magnetizing axis with alternating direction

Simulation features:
- prismatic magnetic rings,
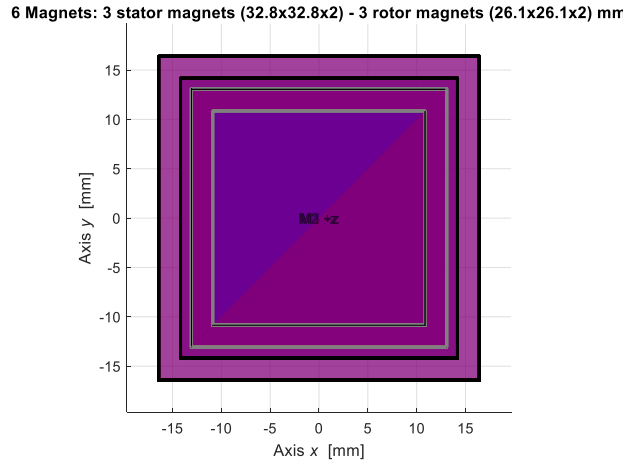- stator magnet moved along the z axis,
- no offset.

Figure 4.3.2.1 – Initial configuration between three rotor rings and three stator rings.
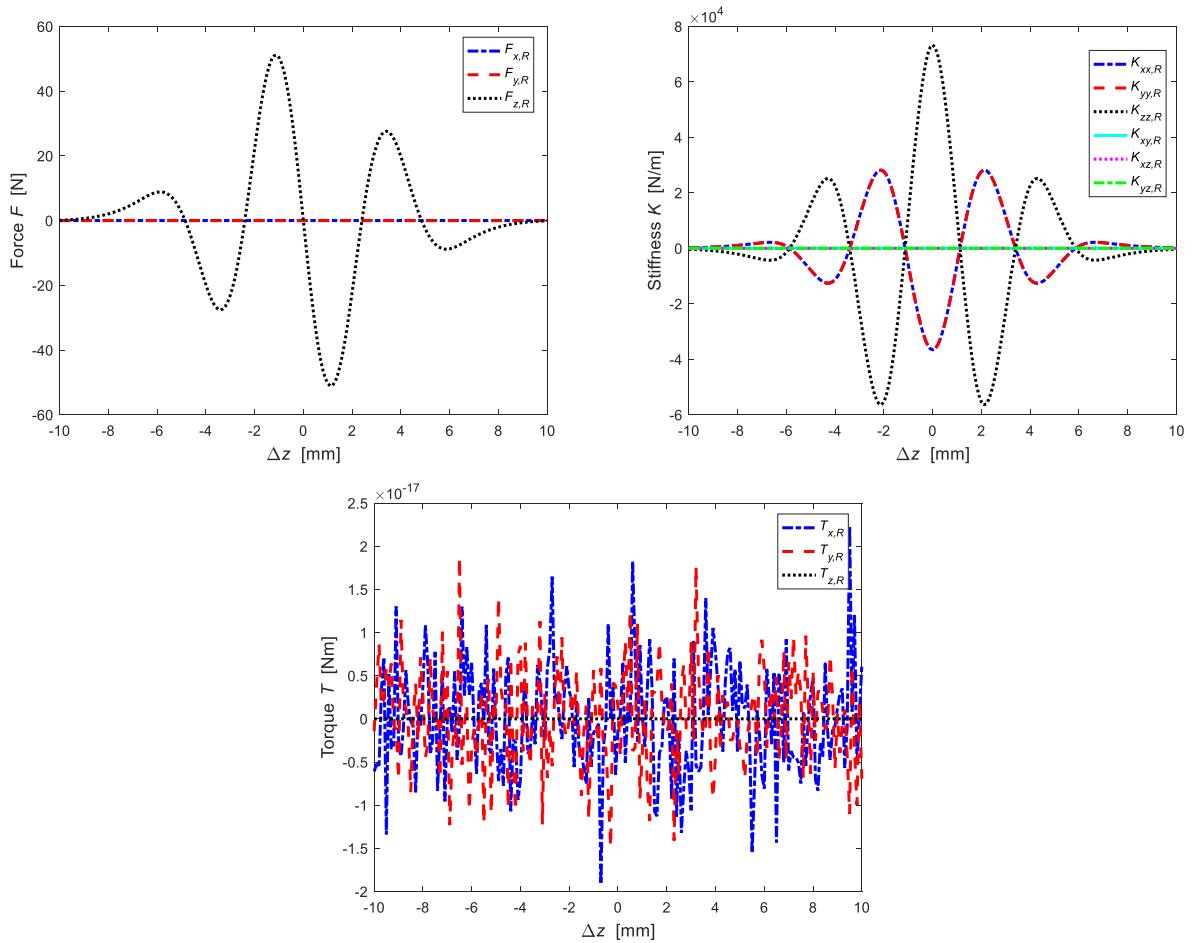

Figure 4.3.2.2 – Forces, stiffnesses and torques.

4.3.3 Analysis of the possible work areas

We proceed with the analysis of the optimal point where it's possible to position the stator rings respect to the rotor rings in order to obtain the optimal combination between strength and stiffness.

As discussed above there are some limitations. It was decided not to consider axial forces down (red zone Figure 4.3.3.1).
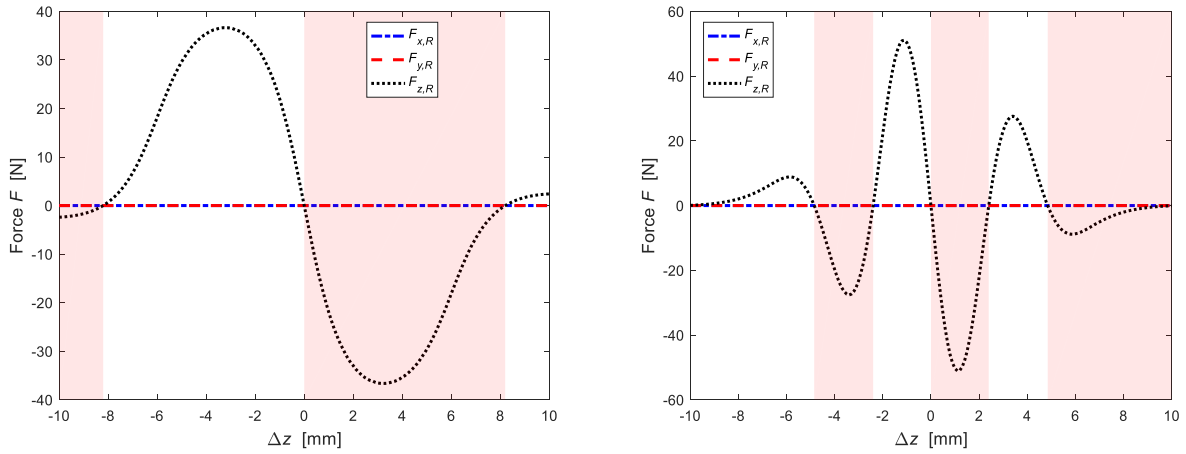

Figure 4.3.3.1 – Work zones in the case of three rings with a residual magnetic induction vector agreement (left) and alternating discordant (right).

The graph in Figure 4.3.3.2 did not take into consideration the areas in which the relative position between the two magnets led to axial stability.
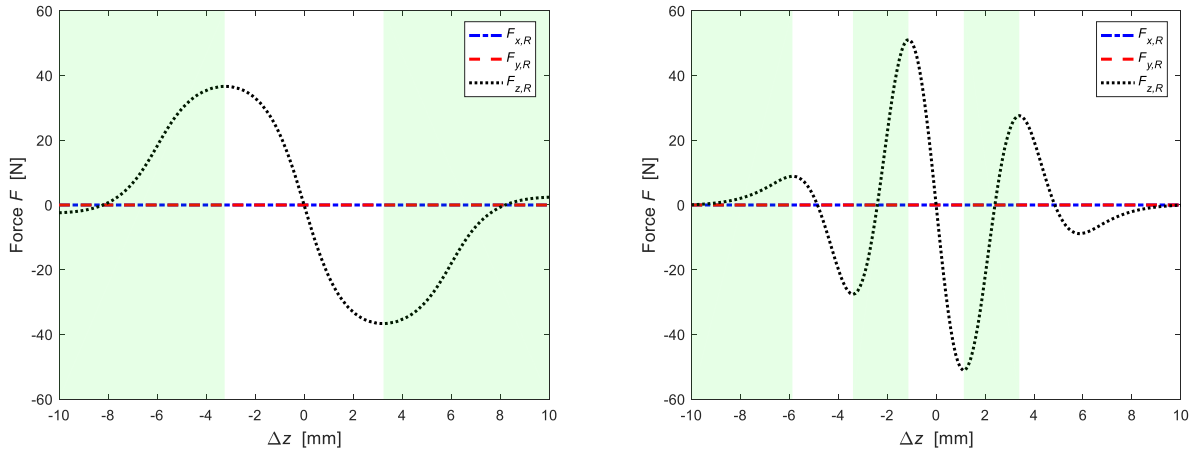

Figure 4.3.3.2 – Areas of possible to positioning in the case of rings with the vector residual magnetic induction agreement (left) and alternating discord (right).

By overlapping the zones where the presence of the magnetic stator rings is not possible, only the white areas in Figure 4.3.3.3 are obtained.

In the event that the rings are all positioned with a residual magnetization vector in the same direction, we obtain a range between [-3.24 ÷ 0] mm; while if the magnets are arranged alternately, we obtain three different ranges: [-5.87 ÷ -4.85] mm, [-1.13 ÷ 0] mm and between [3.4 ÷ 4.85] mm.

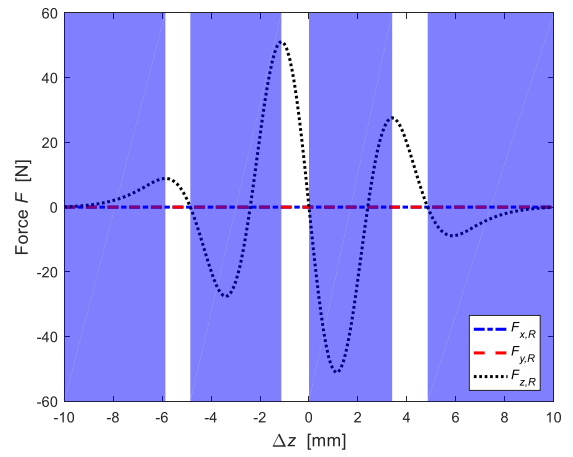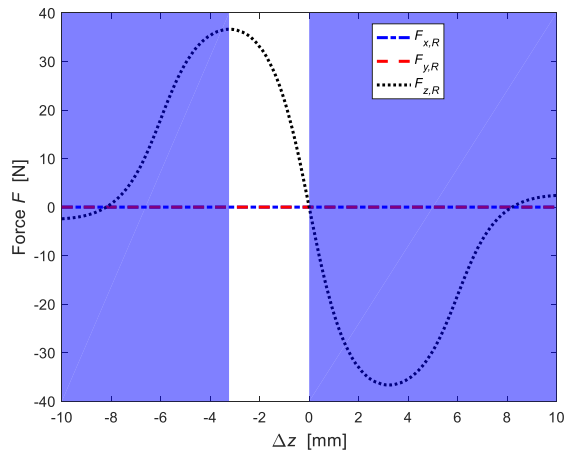Figure 4.3.3.3 – Positioning zones of the stator ring in two cases under examination.

4.4 Case 4 - Simulation of eight magnets with axial displacement

4.4.1 Magnets with magnetizing axis in the same direction

Simulation features:
- prismatic magnetic rings,
- stator magnet moved along the z axis,
- no offset.
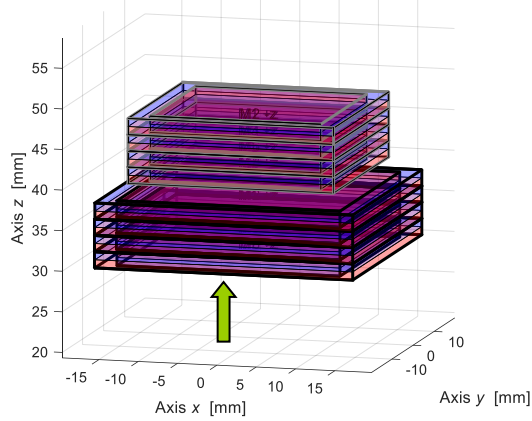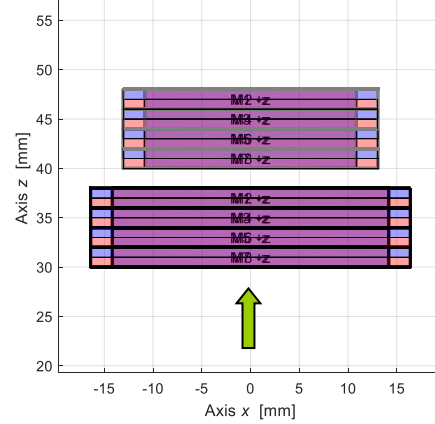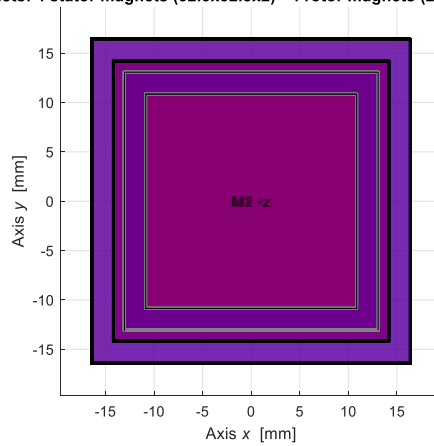
Figure 4.1.1.1 – Initial configuration of magnets with magnetization axis in the same direction.
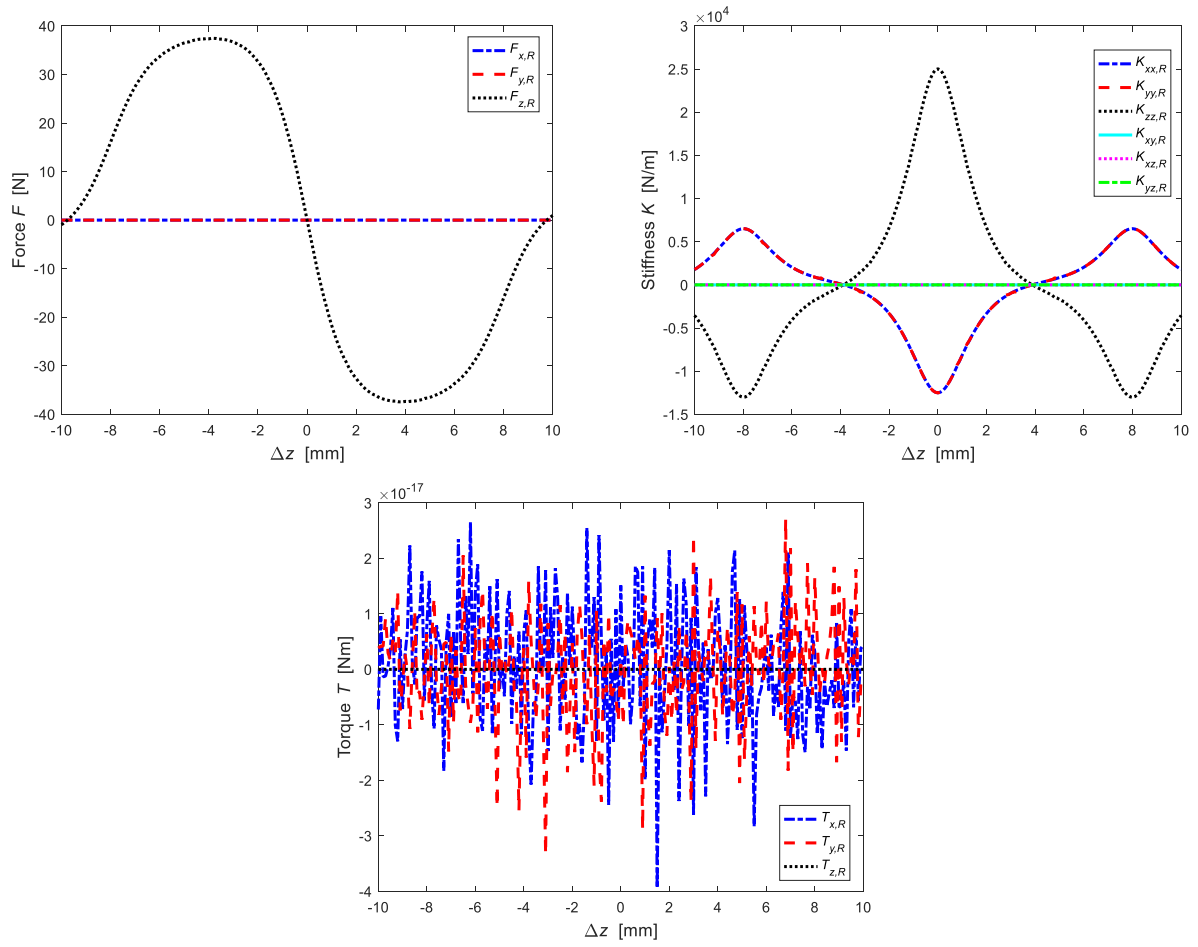
Figure 4.4.1.2 – Forces, stiffnesses and torques.

In this case the interaction between four stator magnets and four rotor magnets with the magnetization axis along the z axis is simulated and all in the same direction. The rotor magnets are fixed while the stator magnets are moved vertically within $\pm$ 10 mm.

The forces, stiffness and torque are those that the rotor magnets feel due to the magnetic field of the stator magnets.

4.4.2 Magnets with magnetizing axis with alternating direction

Simulation features:
- prismatic magnetic rings,
- stator magnet moved along the z axis,
- no offset.
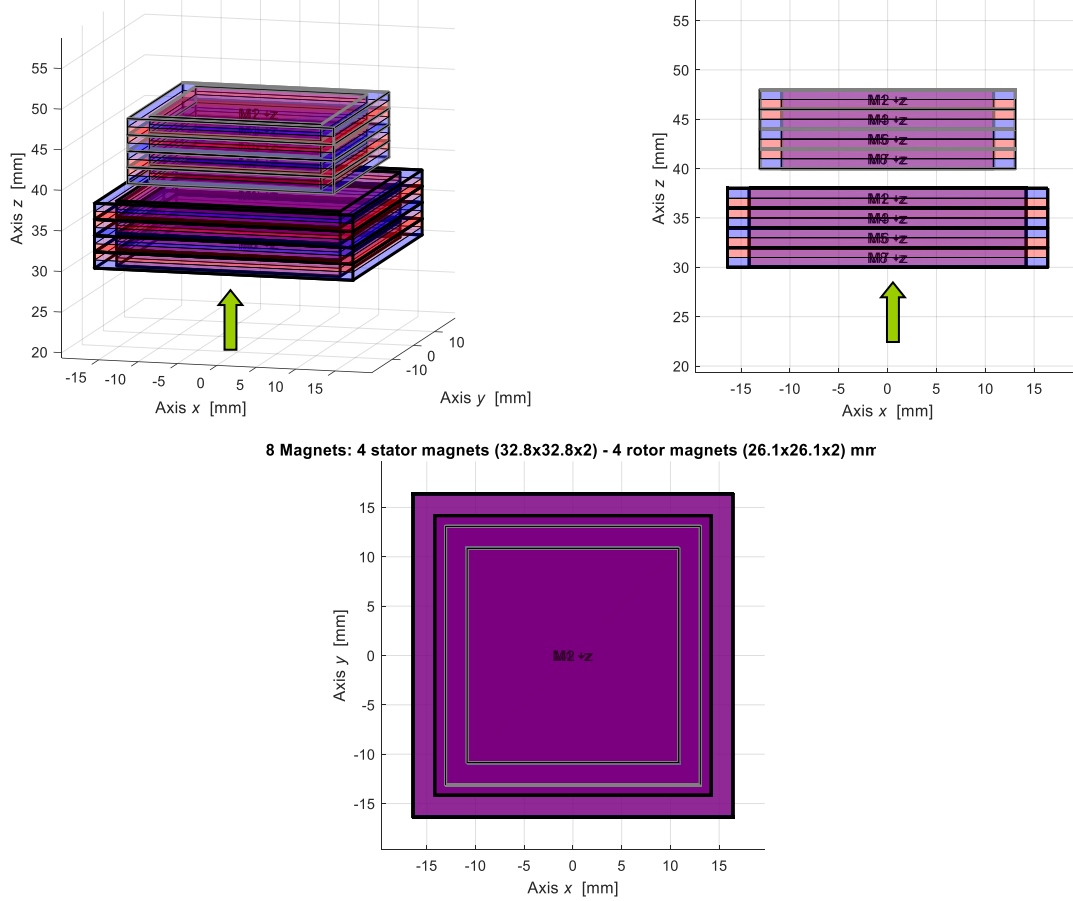
Figure 4.4.2.1 – Initial configuration of magnets with magnets with a reciprocating magnetization axis.
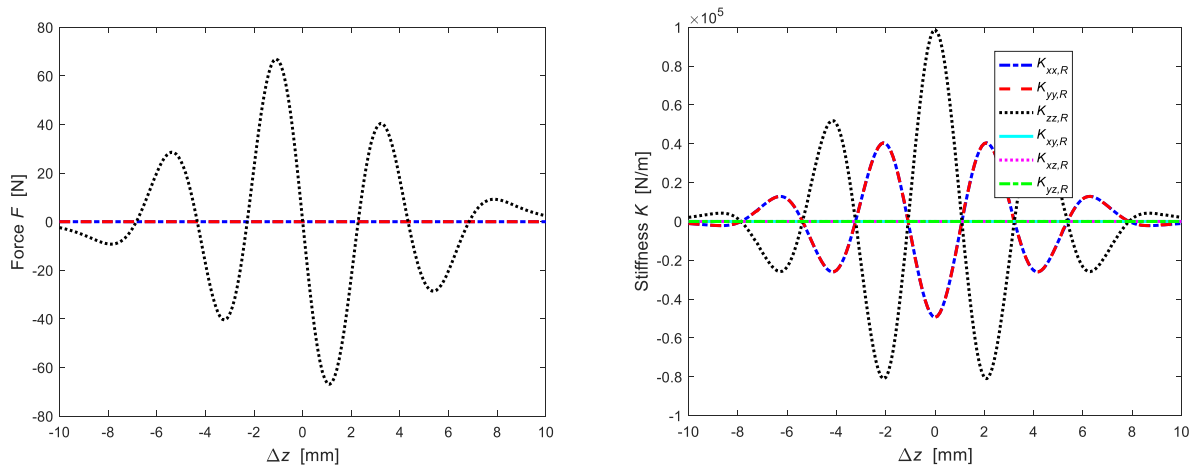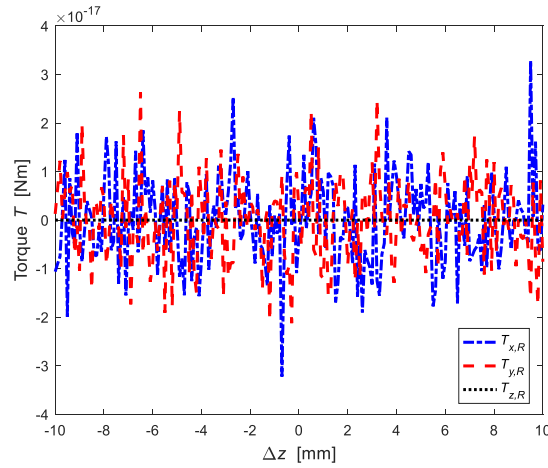
Figure 4.4.2.2 – Forces, stiffnesses and torques.

The forces, stiffnesses and torques are those that the rotor magnets feel due to the magnetic field of the stator magnets. Analysing the graphic of the forces we can see that through the opposition of the residual induction between adjacent magnets, peaks of higher forces are obtained. This behaviour is typical of permanent magnets since the forces depend on the Br gradient and therefore the discontinuities along one direction.
Also, in this case the value of the pairs when the dimension in z is changed is zero.

### 4.4.3   Analysis of the possible work areas

After examining the forces and stiffness of the magnets in the two configurations, we proceed to the analysis of the possible work zones.
Since it is attempted to obtain a magnetic rotor with a minimum contribution of the weight force, the two axial forces are directed in opposite direction to the weight force acting on the rotor magnets generated by the magnetic fields of the stator magnets.
For this reason, we consider the negative traits of the curve (the red areas) to be excluded because they produce axial forces that agree with the weight force.
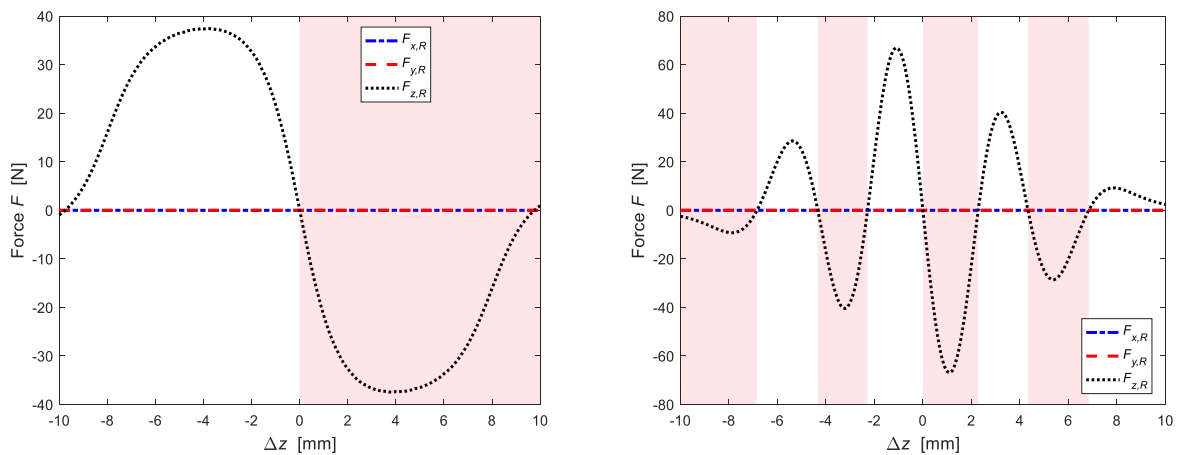
Figure 4.4.3.1 – Work zones in the case of rings with a residual magnetic induction vector agreement (left) and alternating discordant (right).

The second condition necessary to reduce the contribution of the weight force is the axial instability of the rotor. According to the Earnshaw theorem [2], an axial instability corresponds to a positive stiffness.

This reduces the possible positions in which to position the stator (the green areas have axial stability and therefore must be excluded).
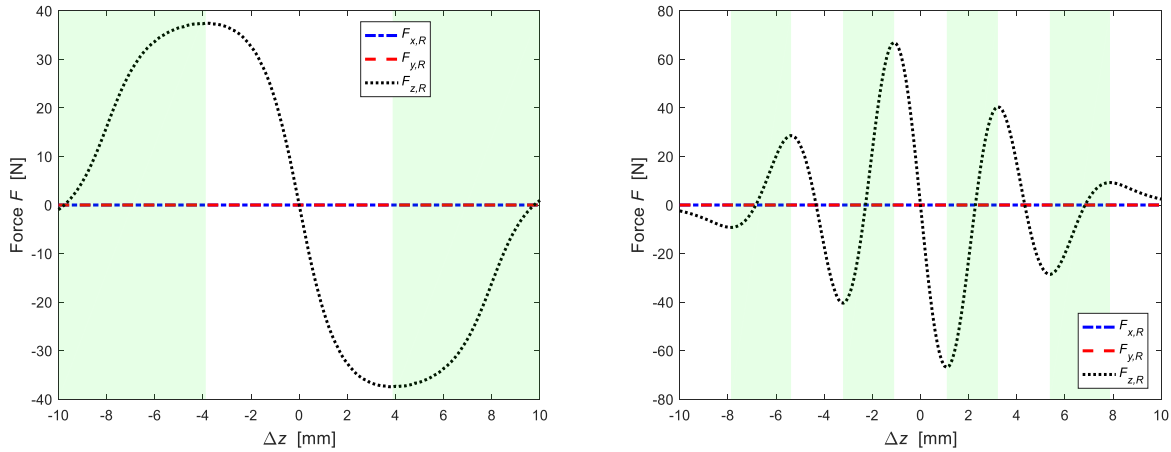
Figure 4.4.3.2 – Areas of possible to positioning in the case of rings with the vector residual magnetic induction agreement (left) and alternating discord (right).

A final limitation of where to place the stator rings is given by the dimensions of the built prototype.
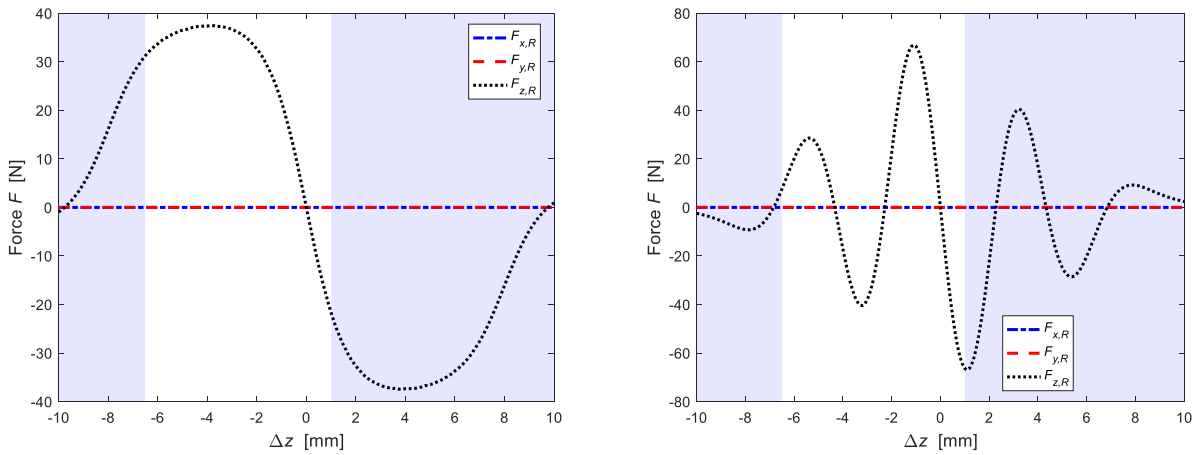
Figure 4.4.3.3 – Areas of a possible positioning of the stator in the two cases examined.

Considering all the various limitations discussed, the areas in which it is possible to position the stator rings with respect to the rotor rings are shown in Figure 4.4.3.4.
In the case where the residual magnetic induction vectors are all in the same direction we obtain a range where it is possible to position the stator rings between [-3.88 ÷ 0] mm; while in the case in which it is decided to arrange the magnets with the alternation of the direction of the residual magnetic induction, we obtain two very small ranges. The first is between [-5.37 ÷ -4.33] mm while the other is between [-1.09 ÷ 0] mm.
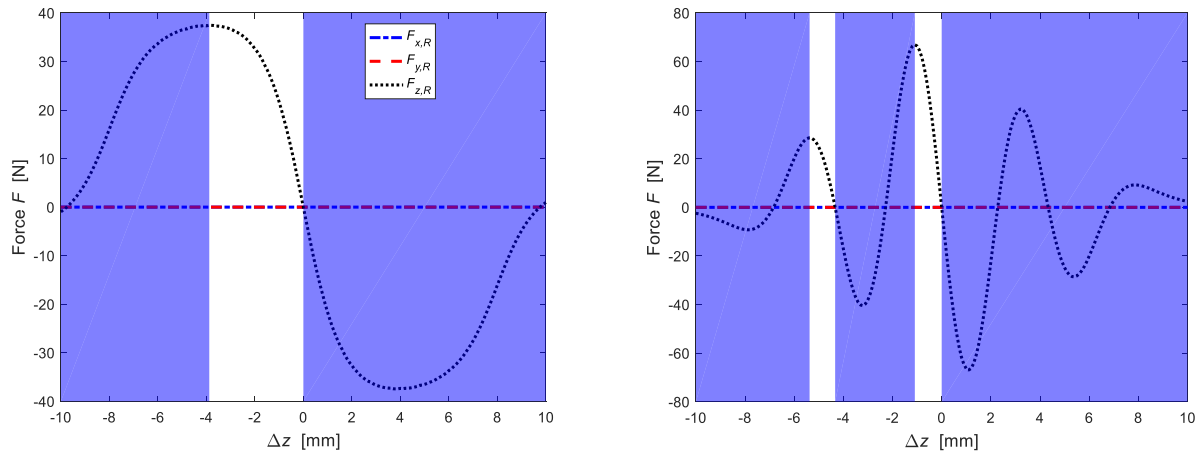
Figure 4.4.3.4 – Positioning zones of the stator ring in two cases under examination.

To understand where to place the stator rings respecting the rotor rings, the weight force exerted by the rotor assembly on the thrust bearing must be analysed.

The rotor assembly has a weight of 4.8 kg and exerts a downwardly directed downward force of about 47 N. In order to achieve a reduction in weight force, the two forces generated by the two rotor-stator couplings are used. We also suppose that these forces are equal.

Table 4.4.3.1 compares the probable positioning of the stator rings for the various cases studied.

Table 4.4.3.1 – Comparison between the forced developed for the different ranges.

Number of magnets	B_r orientation	Range [mm]	Optimal force developed [N]
1	Indifferent direction	-1.45 ÷ 0	11.3
2	Same direction	-2.35 ÷ 0	21.2
	Alternating direction	-1.24 ÷ 0	26
		3.94 ÷ 10	6.4
3	Same direction	-3.24 ÷ 0	22
	Alternating direction	-5.87 ÷ -4.85	7.9
		-1.13 ÷ 0	33.4
		3.4 ÷ 4.85	19.8
4	Same direction	-3.88 ÷ 0	21.7
	Alternating direction	-5.37 ÷ -4.33	22.5
		-1.09 ÷ 0	28.6

The choice of the number of magnets is not influenced by the maximum stiffness value. In fact, as the number of magnets increases, at first there is an increase in stiffness to then reach a stall value. However, we can see an increase in the radial stability zone.

4.5   Choice configuration
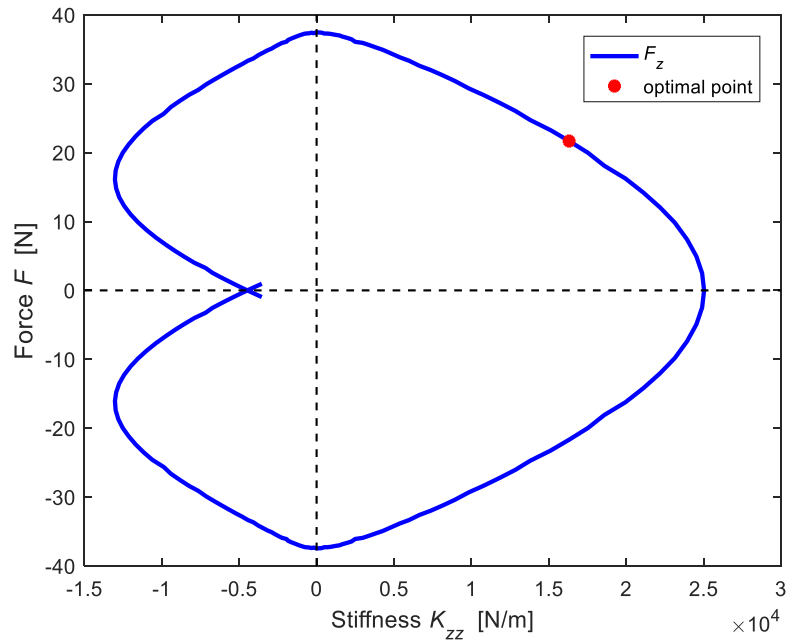
4.5.1 – Strength of the forces as the vertical stiffness changes.

In Figure 4.5.1 we can see how the axial force varies with increasing stiffness. In the case of our interest, we will consider only the first quadrant, where both the force and the axial stiffness are positive.

In order to have easier positioning chances, it has been decided to assemble all the rings with the residual magnetic induction vectors in the same direction by positioning the stator rings one millimetre under the rotor rings. This configuration was chosen as a compromise between the high magnetic upward force enough to reduce the weight force and a positive axial stiffness, index of axial instability.

Furthermore, it was decided to use a different number of magnets between the upper part (2 magnets) and the lower one (4 magnets) of the rotor because of the dimensions that reduced the areas of possible positioning of the rings. Table 4.5.1 shows the characteristics of the selected configuration.

Table 4.5.1 – Forces and stiffness of magnetic groups.

Number of magnets	B_r orientation	Optimal force developed [N]	Axial stiffness [N/m]	Radial stiffness [N/m]
2	Same direction	21.2	$1.54 \cdot 10^4$	-7707
4	Same direction	21.7	$1.63 \cdot 10^4$	-8159

5. Radial displacement

After choosing the positioning dimension of the stator rings, it was decided to analyse the behaviour of the forces, stiffnesses and torques to a displacement along the y axis. This study will produce completely analogous results to that of circular magnetic rings moved in any radial direction.

5.1 Lower bearing

For the lower bearing, the chosen configuration has four stator magnets and four rotor magnets. The direction of the displacement on which to evaluate the forces and magnetic torques is indifferent due to the axial symmetry of the rotor.

Simulation features:
- prismatic magnetic rings,
- stator magnet moved along the y axis,
- offset of 1 mm.
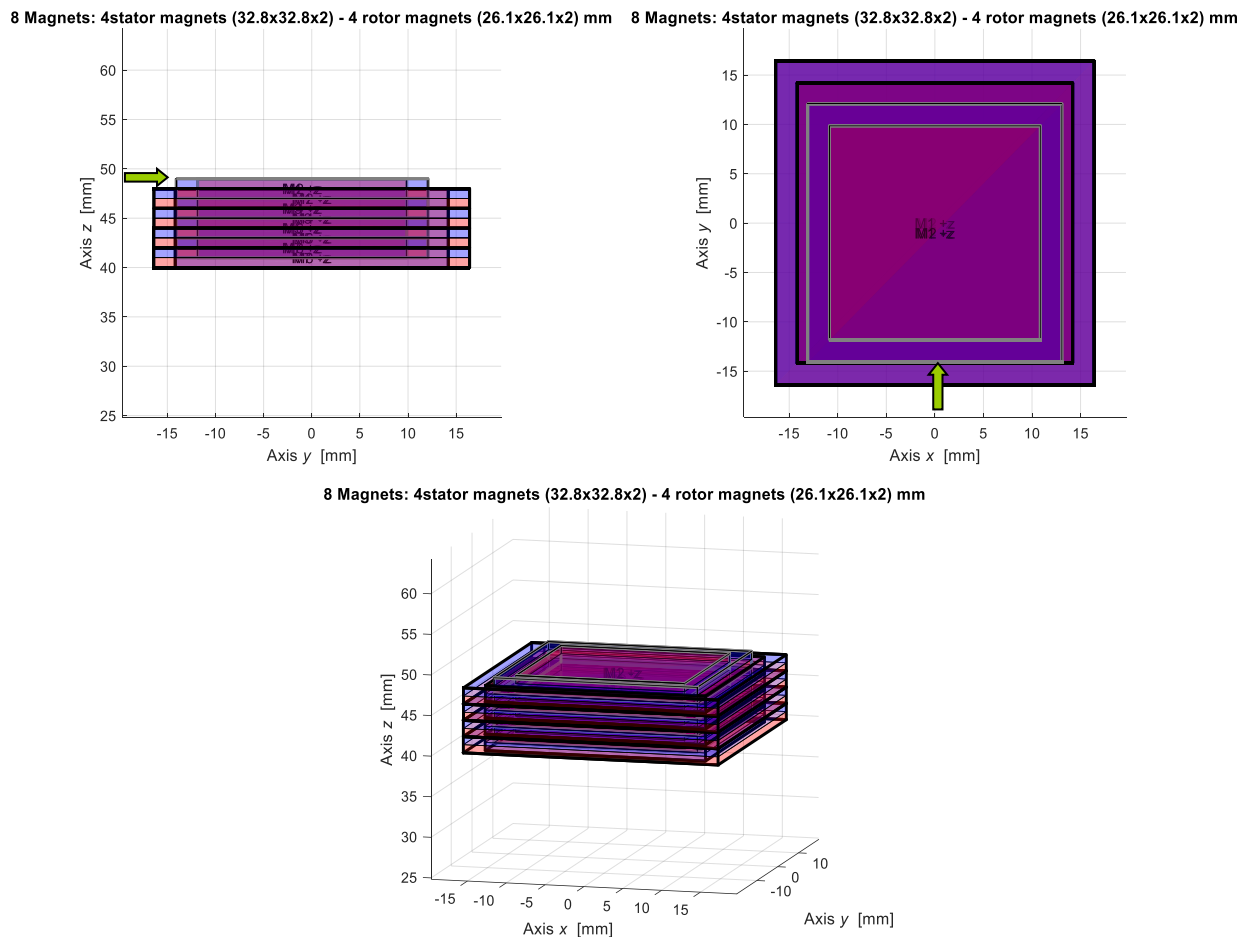
5.1.1 – Initial configuration with movement of the rotor magnets along y.
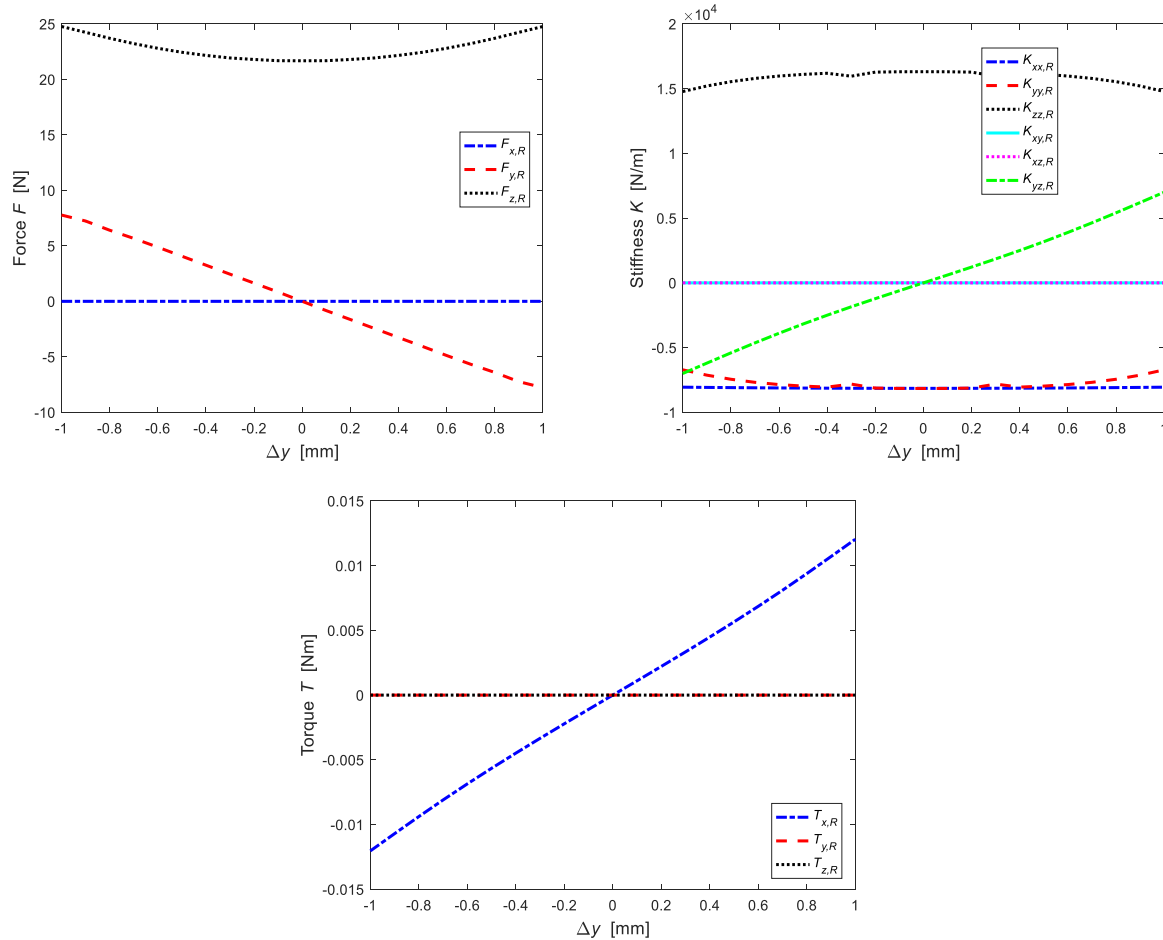
5.1.2 – Forces, stiffnesses and torques for a radial displacement.

Due to the small displacement imposed on the rotor magnets, the characteristic of the axial force is almost flat, a positive feature since there are no high peaks of forces when the two magnets come into contact.

5.2 Upper bearing

Similarly, to what was done for the lower bearing, the forces and torques obtained from a radial displacement of the rotor magnets for the upper bearing are analysed.

Simulation features:
- prismatic magnetic rings,
- stator magnet moved along the y axis,
- offset of 1 mm.

4 Magnets: 2 stator magnets (32.8x32.8x2)- 2 rotor magnets (26.1x26.1x2) mm **4 Magnets: 2 stator magnets (32.8x32.8x2)- 2 rotor magnets (26.1x26.1x2) mm**
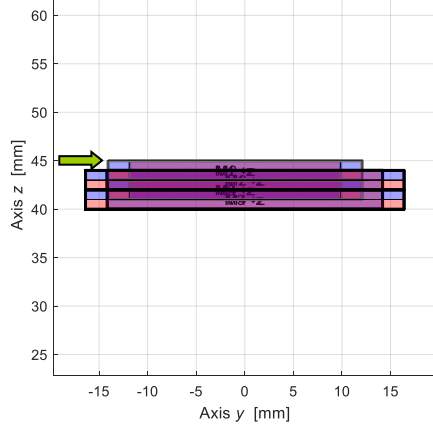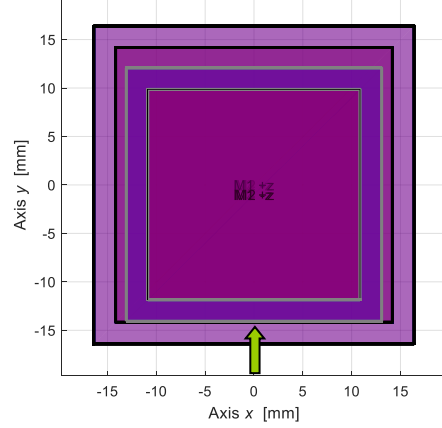
4 Magnets: 2 stator magnets (32.8x32.8x2)- 2 rotor magnets (26.1x26.1x2) mm
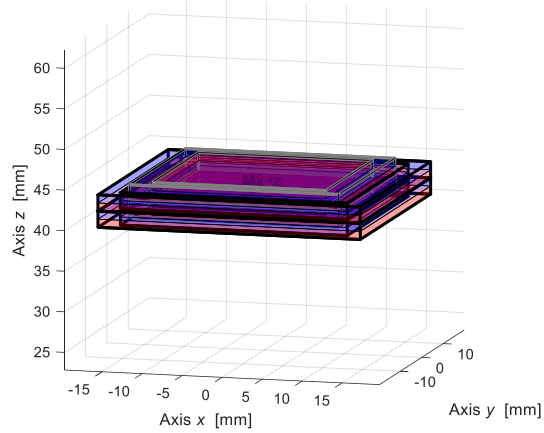
Figure 5.2.1 – Initial configuration with movement of the rotor magnets along y.
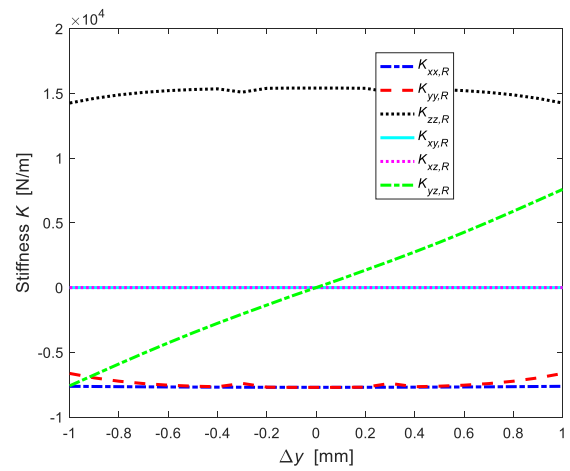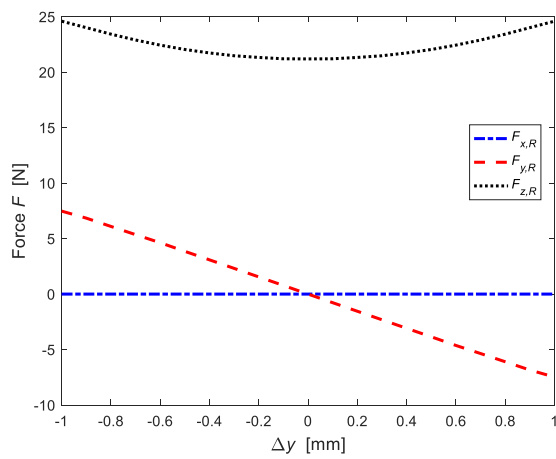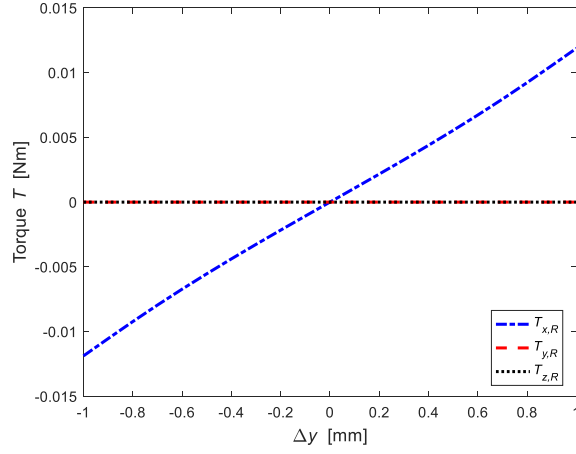
Figure 5.2.2 – Forces, stiffnesses and torques for a radial displacement.

Considering the study just carried out, it was decided to place the stator rings 1 mm below the rotor rings and with the residual magnetization vectors all oriented in the same direction. This decision guarantees a good radial stability and a great axial instability, exploited for the reduction of the weight force acting on the thrust bearing.

6. Equations of motion – Linear behaviour

The study of the behaviour of a system that is under the action of dynamic forces is crucial for the identification of its dynamic characteristics.
In the case of linear dynamic system, the following must be analysed:
- natural frequencies;
- deformed modal corresponding to the natural frequencies.

These can be determined both from damping model and from model without damping: in the first case we have complex modal deformations, while in the second case real modal deformations.
The equations of motion of a rotor can be obtained by the Lagrange approach or the Eulerian approach. The two methods are equivalent, and we arrive at a system of n equations in n degrees of freedom.
What most characterizes the analysis of the rotors compared to other no-rotating dynamical systems is the presence of the gyroscopic effects. So, the matrix equation of the dynamics of a rotor must consider these effects by introducing a gyroscopic matrix that multiplies the velocity vector.
The matrix equation becomes:

$$\mathbf{M}\ddot{\mathbf{x}} + \left(\mathbf{C} + \Omega\mathbf{G}\right)\dot{\mathbf{x}} + \mathbf{K}\mathbf{x} = \mathbf{F} \tag{6.1}$$

where:
- $\mathbf{M}$ is the mass matrix $(n \times n)$;
- $\mathbf{C}$ is the damping matrix $(n \times n)$;
- $\mathbf{G}$ is the gyroscopic matrix $(n \times n)$;
- $\mathbf{K}$ is the stiffness matrix $(n \times n)$;
- $\mathbf{F}$ is the external forces matrix $(n \times 1)$
- $\mathbf{x}, \dot{\mathbf{x}}, \ddot{\mathbf{x}}$ are respectively the generalized displacements, the velocities and accelerations of the only active degrees of freedom.

In this case, the generical vector q has six component (n=6) that correspond at six degrees of freedom. The first three elements are the displacements along the axes, while the other elements are the three main rotations.

$$\mathbf{x} = \begin{Bmatrix} x \\ y \\ z \\ r_x \\ r_y \\ r_z \end{Bmatrix} \tag{6.2}$$

For the evaluation of natural frequencies and modal deformations the homogeneous equation associated with the dynamic system equation without damping must be considered

$$\mathbf{M}\ddot{\mathbf{x}} + \left(\mathbf{C} + \Omega\mathbf{G}\right)\dot{\mathbf{x}} + \mathbf{K}\mathbf{x} = 0 \tag{6.3}$$

and then look for the eigenvalues of the associate matrix. To this aim, let assume that solutions can be expressed in the form:

$$\mathbf{x} = \mathbf{x_0} e^{st} \tag{6.4}$$

where:

$$s = \sigma + i\lambda \tag{6.5}$$

are the complex frequencies of the system that can be computed as the eigenvalues of the matrix associated to the dynamic equations.

In particular, the imaginary and real part of s represent respectively:
- the whirl frequency $\lambda = \text{Im}(s)$, which corresponds to the natural frequencies of the free motion;
- the decay rate $\sigma = \text{Re}(s)$, which corresponds to the rate at which the amplitude decreases (or increases) in time.

To further simplify the modal analysis of the magnetic rotor, it is decided to analyse the gyroscopic matrix in a later stage and then the equation of motion is reduced:

$$\mathbf{M\ddot{x} + C\dot{x} + Kx} = 0 \tag{6.6}$$

6.1 Modal analysis without damping

To further simplify the modal analysis of the magnetic rotor, it is decided to analyse the gyroscopic matrix in a later stage and as first analysis we consider the un-damped system represented by the equation:

$$\mathbf{M}\ddot{\mathbf{x}} + \mathbf{K}\mathbf{x} = 0 \tag{6.1.1}$$

The modal analysis of the rotor without damping, defined by the equation 2.3, is evaluated using LUPOS. The LUPOS model is an m-file that contains all the elements necessary to create the model. This software runs in the MATLAB environment, and we can set analysis options using a graphical interface.

The first step in creating a model in Lupos is the definition of the geometry to be analysed. For this reason, the matrix containing the positions of the nodes taken all along the vertical axis of the rotor is inserted. The geometry of the shaft can be simplified as a succession of cylinders with faces adjacent to one another. For this reason, there will be a new node at each change of the orthogonal section to the axis. The point of contact between the shaft and the thrust ball was chosen as the first node.
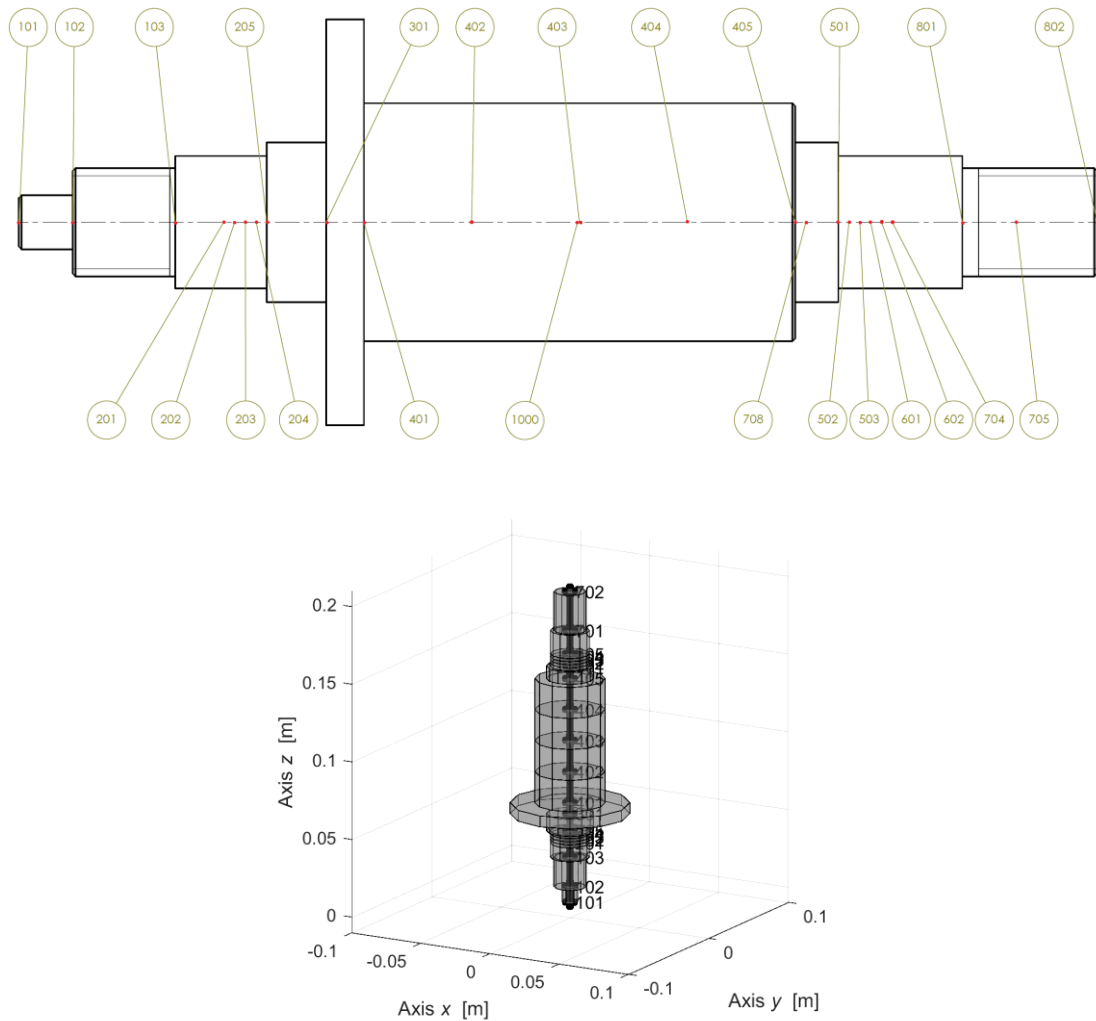

Figure 6.1.1 – Nodes position on the shaft.

As can be seen in the Figure 6.1.1, the number of nodes used is enough to determine the position in which the hubs and the magnets will be positioned.

Beyond the geometry of the shaft, the hubs and the rotor magnets have been modelled and new nodes have been added to it, similarly to what has just been seen.

The nodes used to determine the geometry of the hubs and magnets will be constrained with some nodes of the shaft to obtain a rigid joint.

The second matrix used in LUPOS generates the geometries through the rod elements.

The rod element is defined as a circular or elliptical tube between two nodes. The cross-section of the element can be solid or annular.

Here the Timoshenko approach is used, as the model considers the shear deformation and the rotational bending effects, making it suitable for the description of the rotor under examination.

With the modelling of all the elements the complete geometry in Figure 6.1.2 was obtained which will be analysed in LUPOS.
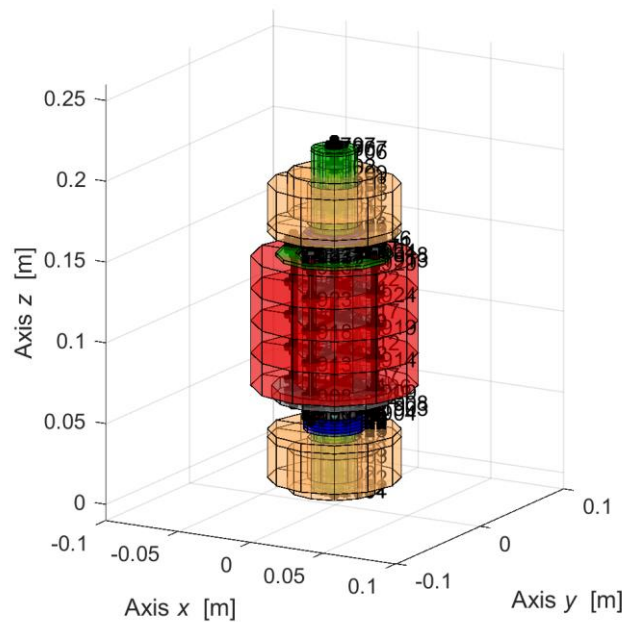
Figure 6.1.2 – Rotor geometry in LUPOS.

6.1.1 Mass matrix

The mass matrix can take two forms: a lumped matrix mass that assumes values different from zero on the main diagonal only and the other consistent which uses a method consistent with the internal displacement field assumed.

In the present case a lumped mass matrix is used where the point mass is in one of the nodes of the model, with rotational and translational inertia properties.

$$\mathbf{M} = \begin{bmatrix} m_x & & & & & \\ & m_y & & & & \\ & & m_z & & & \\ & & & J_t & & \\ & & & & J_t & \\ & & & & & J_p \end{bmatrix} \tag{6.1.1.1}$$

The mass matrix has been obtained through the LUPOS analysis. This matrix is a 6x6 and as you can see in the Figure 6.1.1.1 the most relevant elements are those along the diagonal. The off-diagonal elements are machine zeros.
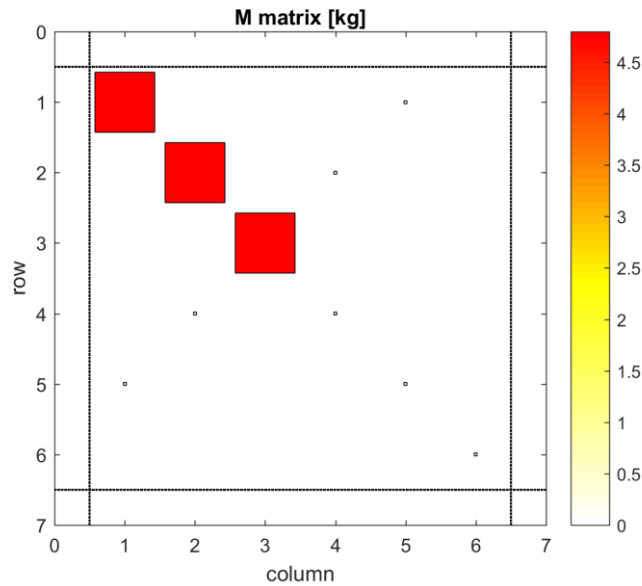
Figure 6.1.1.1 – Distribution of the mass matrix.

6.1.2 Stiffness matrix

Similarly, to what was done for the mass matrix, the stiffness matrix was generated. Generally, it is not a diagonal matrix, although it usually has a band structure. In this case is a 6x6 matrix and as you can see in the Figure 6.1.2.1, the element $k_{3,3}$ are greater than the others. This represents the rigidity along the z axis and is much greater than that in the other directions because.

Figure 6.1.2.1 – Distribution of the stiffness matrix.

6.1.3 Rotor modes

The approach is based on the modal analysis generally focused on the most important low order methods, but in no way limited in principle to these modalities.
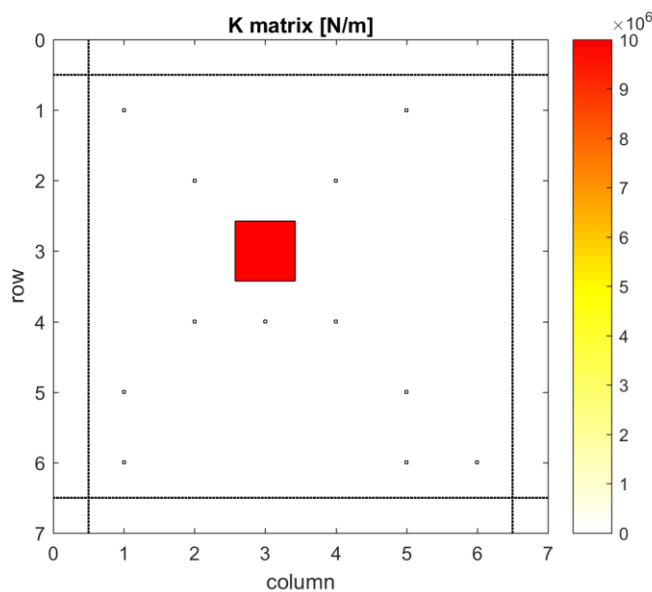
In classical mechanics a "mode" is a description of movement. There are various types of modes, such as the "principal", "bending" or "torsional" or "coupled" modes.

For the study of the rotor, we will not consider the flexural and torsional modes of the shaft because is treated as a rigid body.

All describe a particular manner of movement. The modes, associated with the natural frequencies of the system, are the most important features of all mechanical vibratory systems.

At natural frequency, a vibrating system moves in "principal" or "natural" mode of free vibration.

The modal analysis will be performed at zero rotation speed and only at a later time will we take into account the gyroscopic component.

6.1.3.1 Mode 1

The first mode found is the null frequency, as can be seen in the Figure 6.1.3.1.1. Since the rotor has not damping (Equation 2.5), the first critical speed corresponds to the natural frequency. This mode produces a rotation of the rotor along the z axis.
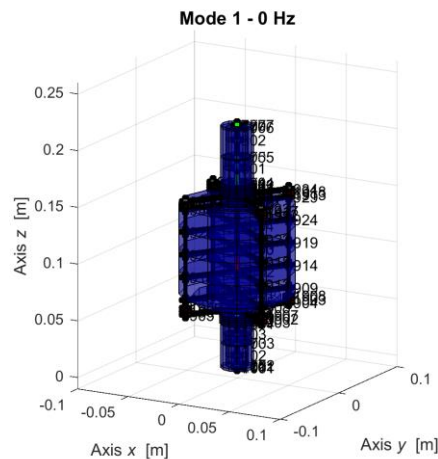
Figure 6.1.3.1.1 – First mode.

6.1.3.2 Mode 2 end mode 3

It is of interest to point out that a rigid shaft on flexible supports can undergo different modes, known as rigid body modes.

In Figure 6.1.3.2.1, the second and the third mode are shown. These two modes are called bounce modes and they correspond to a cylindrical whirl for which the deflection at each bearing is in phase are paired and develop orthogonal to each other. We both get them for a frequency of 9.114 Hz.

Figure 6.1.3.2.1 – Mode 2 and mode 3.

6.1.3.3 Mode 4 and mode 5
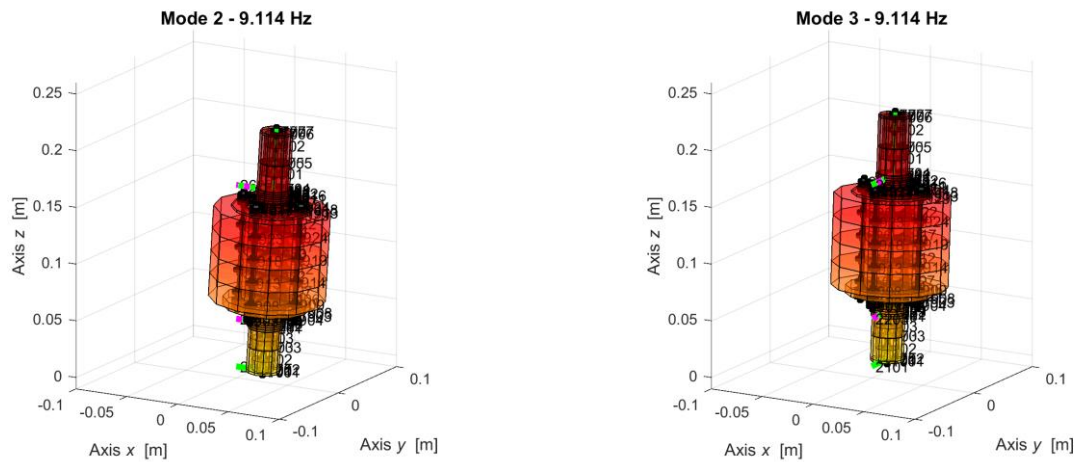
In Figure 6.1.3.3.1 shows the pitch mode, which is characterised by a conical whirl, for which the deflection at each bearing is 180 degrees out of phase.
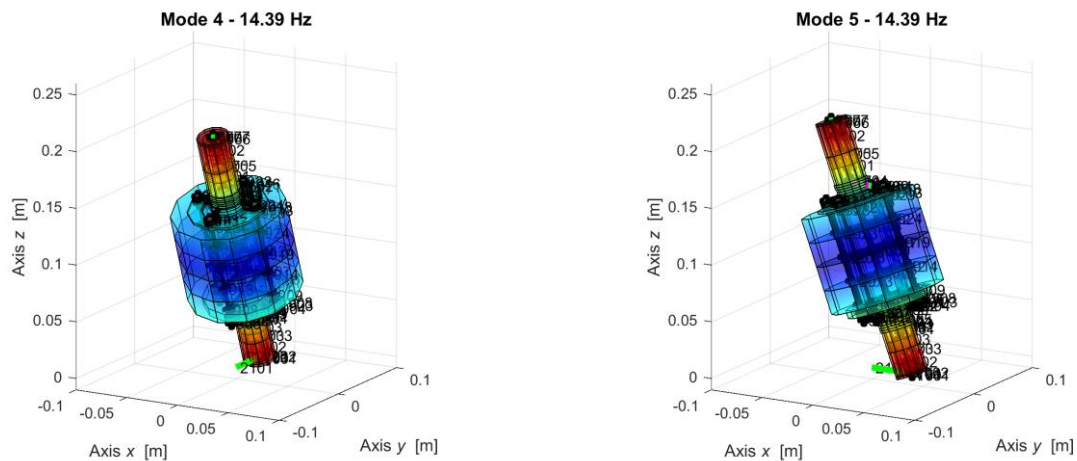
Figure 6.1.3.3.1 – Mode 4 and mode 5.

Remembering that the system is axially symmetrical (both the rotor and the stator), there are two modes, connected with the mainly conical vortex, but since there are not conditions of symmetry between the upper and inferior magnetic bearings it is not possible to have modes conical. We both get them for a frequency of 14.39 Hz.

6.1.3.4 Mode 6

The last way found with the fem analysis is a 229.8 Hz (Figure 6.1.3.4.1) and represents an oscillating shift along the rotation axis.

Figure 6.1.3.4.1 – Mode 6.

6.1.4 Simulation model

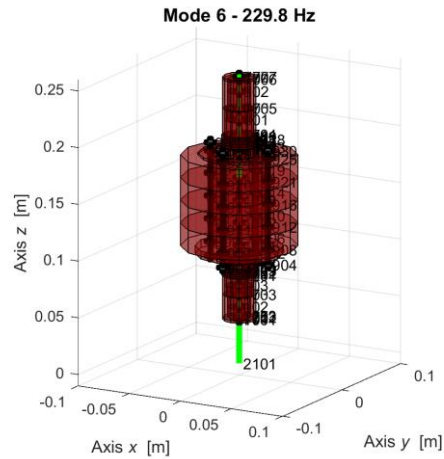With the mass matrix and with the matrix of stiffness obtained with the fem analysis in LUPOS, we have moved to the simulation of the magnetic rotor in Simulink.
To implement the equation 2.1, it is necessary to define the gyroscopic matrix.

6.1.4.5 Gyroscopic matrix

The gyroscopic matrix contains the polar moments of inertial, and hence conservative, terms that, in the case of rotodynamic, are strictly linked with the gyroscopic moments acting on the rotating parts of the machine. If the equation is written with reference to a no inertial frame, terms linked with Coriolis acceleration also are present in the gyroscopic matrix.

$$
\mathbf{G} = \begin{bmatrix} 0 & 0 & 0 & 0 & 0 & 0 \\ 0 & 0 & 0 & 0 & 0 & 0 \\ 0 & 0 & 0 & 0 & 0 & 0 \\ 0 & 0 & 0 & 0 & J_p & 0 \\ 0 & 0 & 0 & -J_p & 0 & 0 \\ 0 & 0 & 0 & 0 & 0 & 0 \end{bmatrix} \tag{6.1.4.5.1}
$$

6.1.4.6 Numerical analyses

The system of equations 2.5 can be solved only after establishing initial conventions for speeds and displacements (Table 6.1.4.6.1).

Table 6.1.4.6.1 – Initial conditions.

Initial condition	Value
$\dot{r}_{z0}$	314 [rad/s]
x_0	$5 \cdot 10^{-4}$ [m]

To make the model as realistic as possible, it was assumed a resistant torque in the air rotation direction equal to 0.001 Nm.
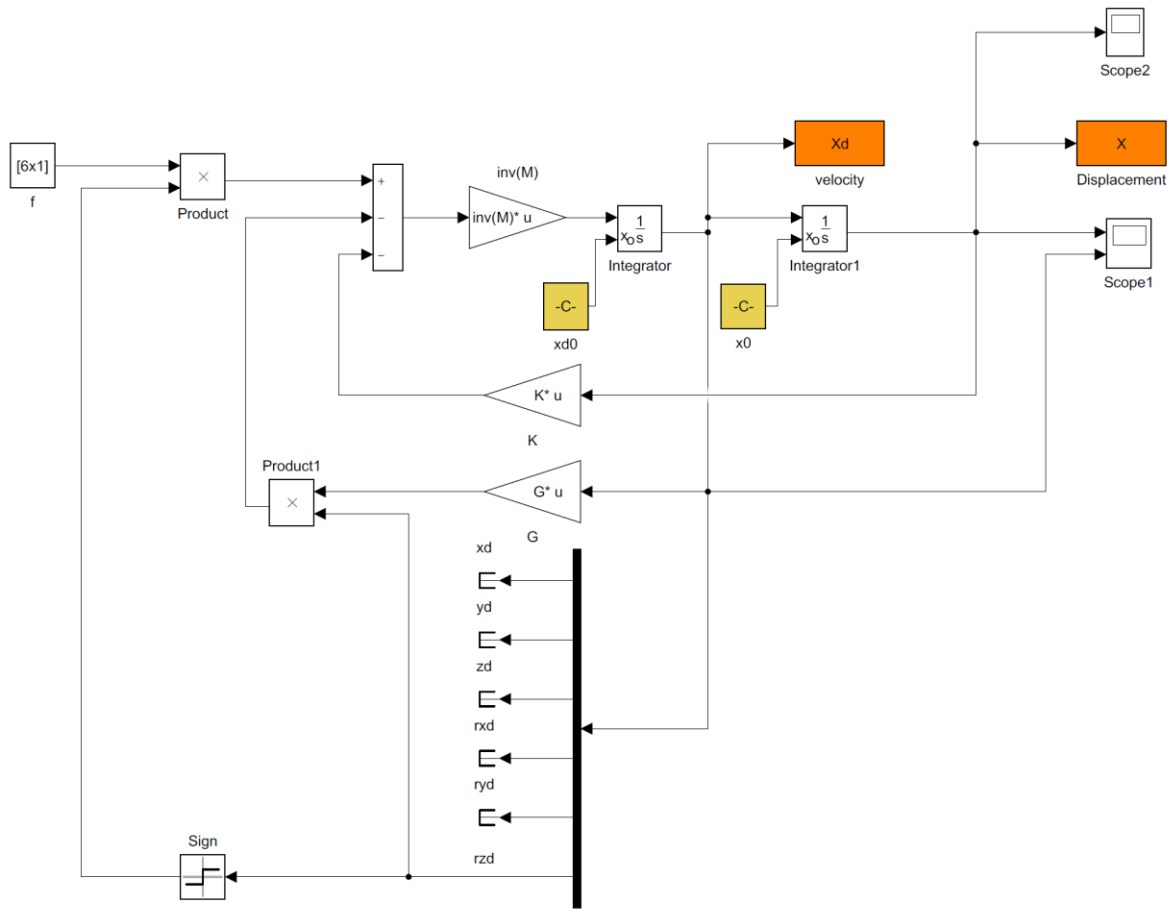

Figure 6.1.4.6.1 – Model of equation 2.5 without damping.

With the simulation model we want to analyse the various aspects of the rotor at the decrease of the rotation speed. Since there is no damping and for this reason the rotation speed will be linear as shown in the Figure 6.1.4.6.2.
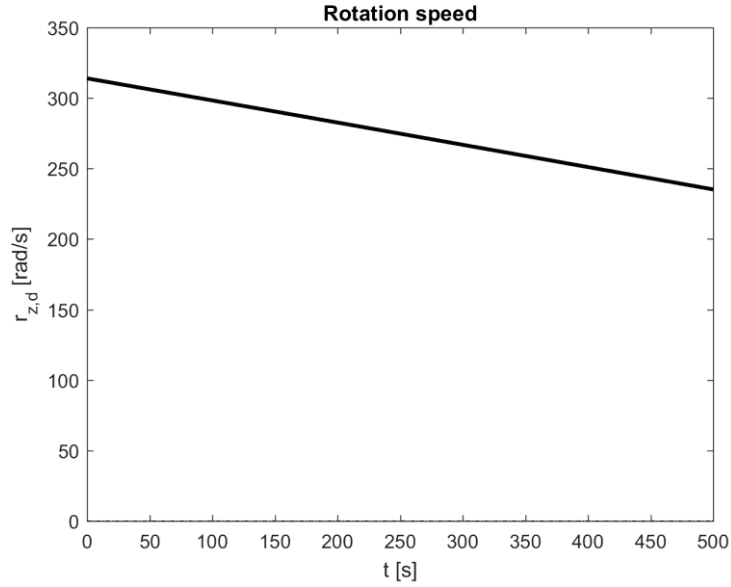
Figure 6.1.4.6.2 – Speed trend.

Among the parameters in analysis are the displacements and rotations of the centre of mass of the rotor in the three main directions. The Figure 6.1.4.6.3 shows the displacement over time of the centre of mass along the rotation axis. This oscillatory trend will grow over time due to the lack of damping, but since the displacements are infinitely small, we can consider the position of the rotor along z constant.
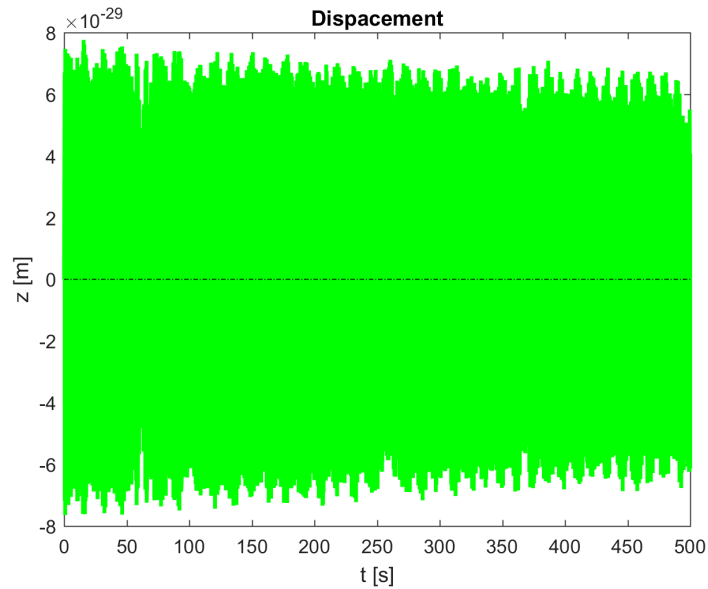

Figure 6.1.4.6.3 – Movement along the rotation axis.

It is also interesting to analyse the trajectory of the rotor in the XY plane when an imbalance of half millimetre is given in one of the two directions. In the Figure 6.1.4.6.4 it can be deduced the typical trajectory where the rotor goes from one end to the other.
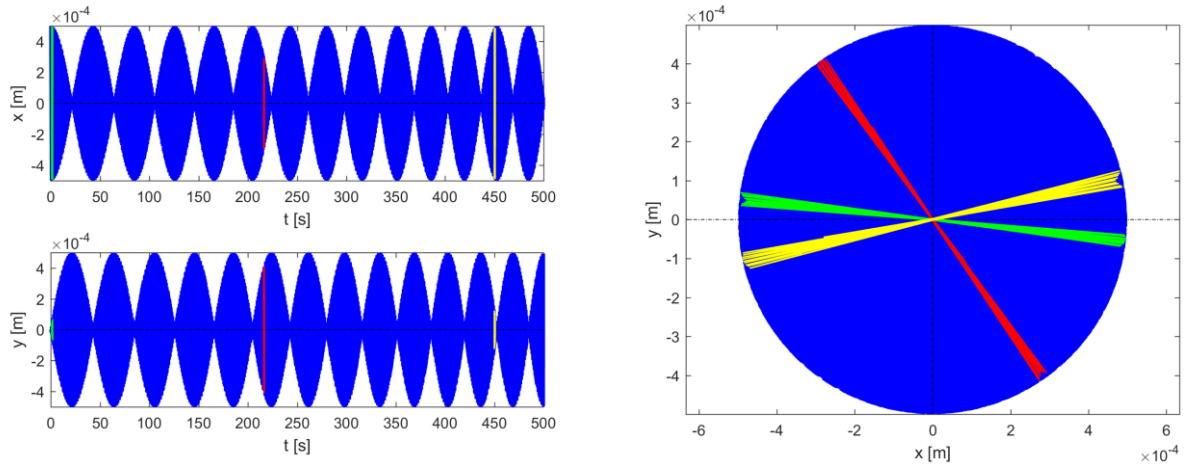
Figure 6.1.4.6.4 – Displacement x-y.

This movement will continue over a very long period because there is not a damping.
During the decay of the rotation speed, small rotary oscillations can be noticed that occur in the other two main directions. This behaviour of the rotor is shown in the Figure 6.1.4.6.5 where there are the two temporal trends of the rotations and the interaction of one with the other.
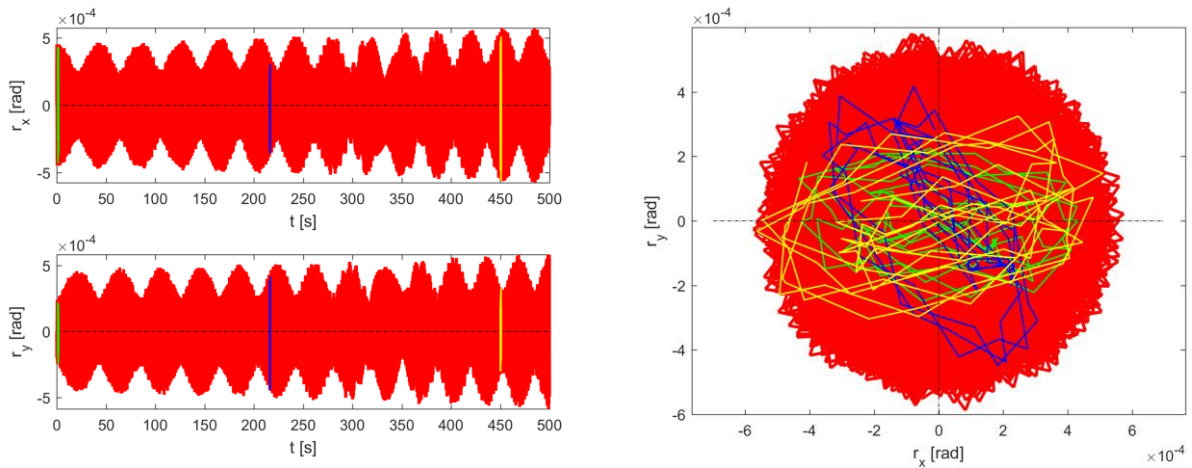

Figure 6.1.4.6.5 – Rotations in x and y directions.

6.2 Modal analysis with damping

Also considering the presence of viscous damping supports, we proceed to the study of dynamic analysis in the most complete form represented by the equation 2.1.

6.2.1 Damping matrix

The damping matrix of the system can be obtained by applying in the nodes that correspond to the magnetic bearings the viscous dampers and in this way the main elements are positioned on the diagonal. This way of evaluating the damping of the system is clearly an approximation that can, in many cases, be very rough. However, it is often used in practice because there are no simple alternatives.
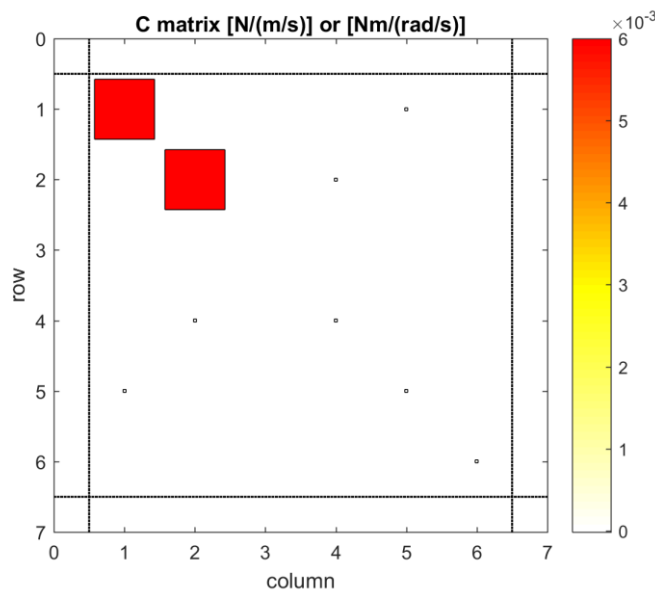
Figure 6.2.1.1 – Distribution of the damping matrix

As can be seen in the Figure 6.2.1.1, the damping elements have been added that simulate the damping behaviour of magnetic bearings and one that simulates air damping.

6.2.2 Rotor modes

Similarly, to what was done for the case without damping, we proceed to modal analysis of the rotor and using LUPOS again. Twelve modes of vibrating at six different frequencies have been found.
Since that the damping of the system is lower than the critical damping, the system is said underdamped and leads to pair of complex-conjugate solutions.
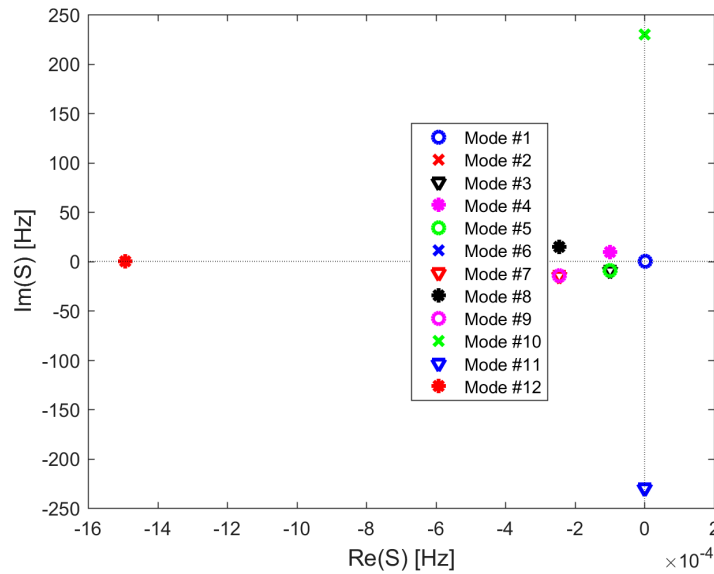
Figure 6.2.2.1 – Representation of the modes in the plane complex.

6.2.2.1 Rigid mode

The first and the last modes of vibration found are those represented in Figure 6.2.2.1.1 at 0 Hz and correspond to the rigid rotation of the rotor on its own axis. These are the overdamped mode.
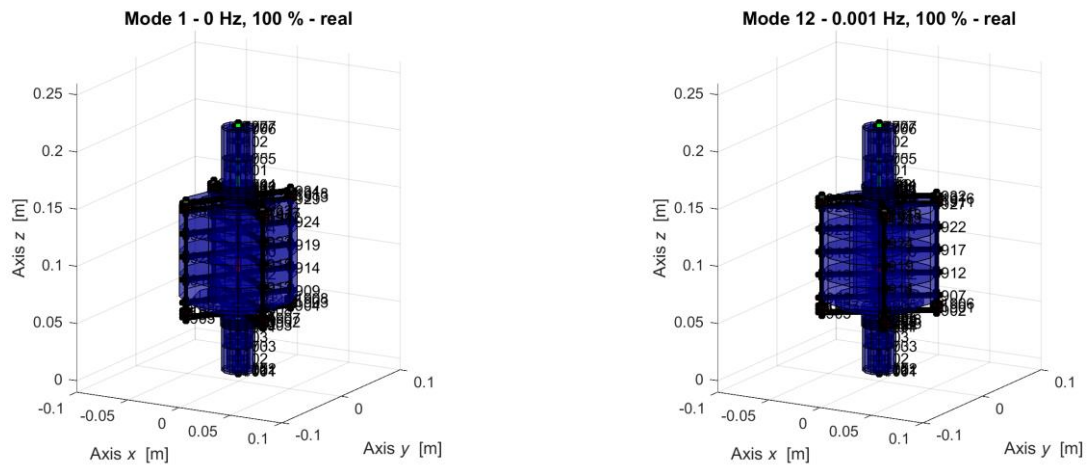
Figure 6.2.2.1.1 –Rotation modes.

6.2.2.2 Cylindrical whirl

At the critical frequency of 9.114 Hz there are four modes, i.e. two different pairs. These modes are called cylindrical because they describe this figure in space (Figure 6.2.2.2.).
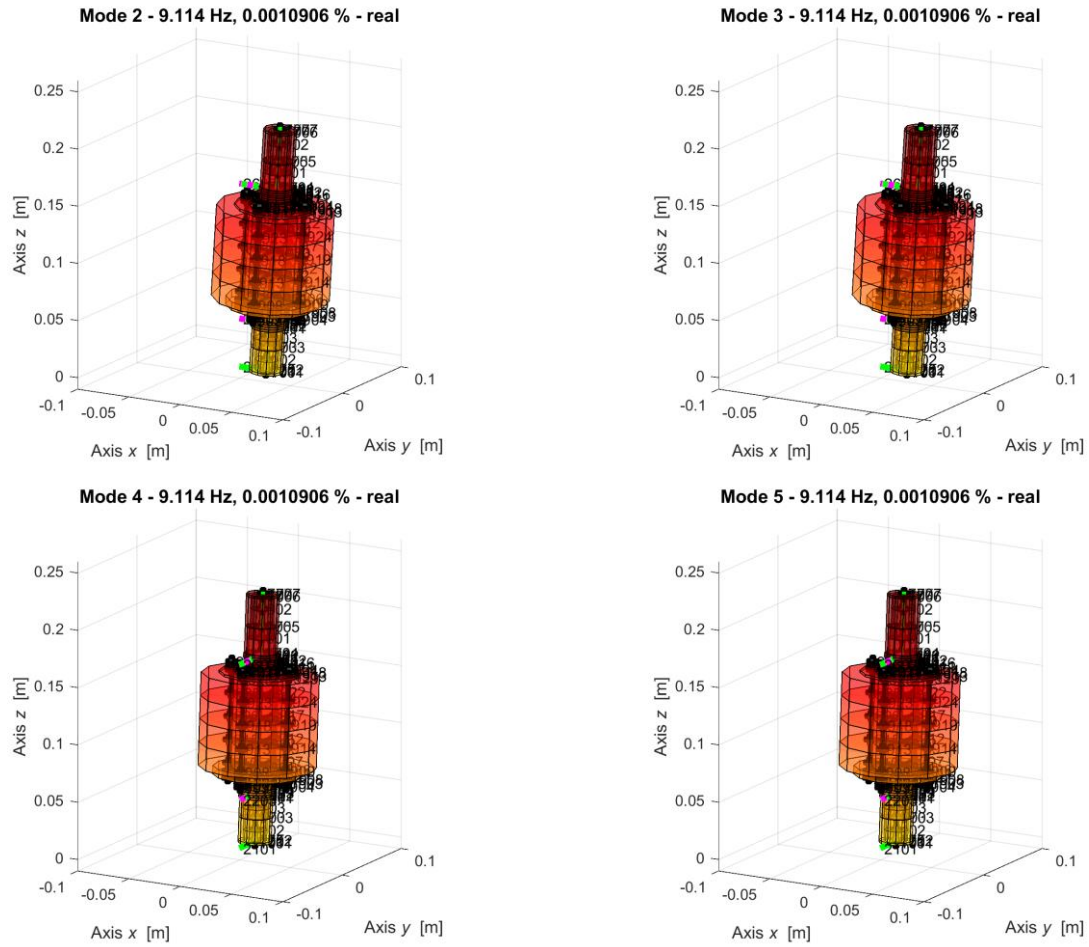
Figure 6.2.2.2.1 – Bounce modes.

Also, in this case the two different pairs develop in orthogonal directions between them (Figure 6.2.2.2.2) and moreover the critical frequency of these modes is slightly increased due to the damping.

Figure 6.2.2.2.2– Bounce modes in XY plane.

6.2.2.3 Conical whirl

Similarly, to what has been said for the cylindrical modes, there are two couples of the modes at a frequency of 14.39 Hz (Figure 6.2.2.3.1). The modes found are conical and develop in two different orthogonal directions (Figure 6.2.2.3.2).
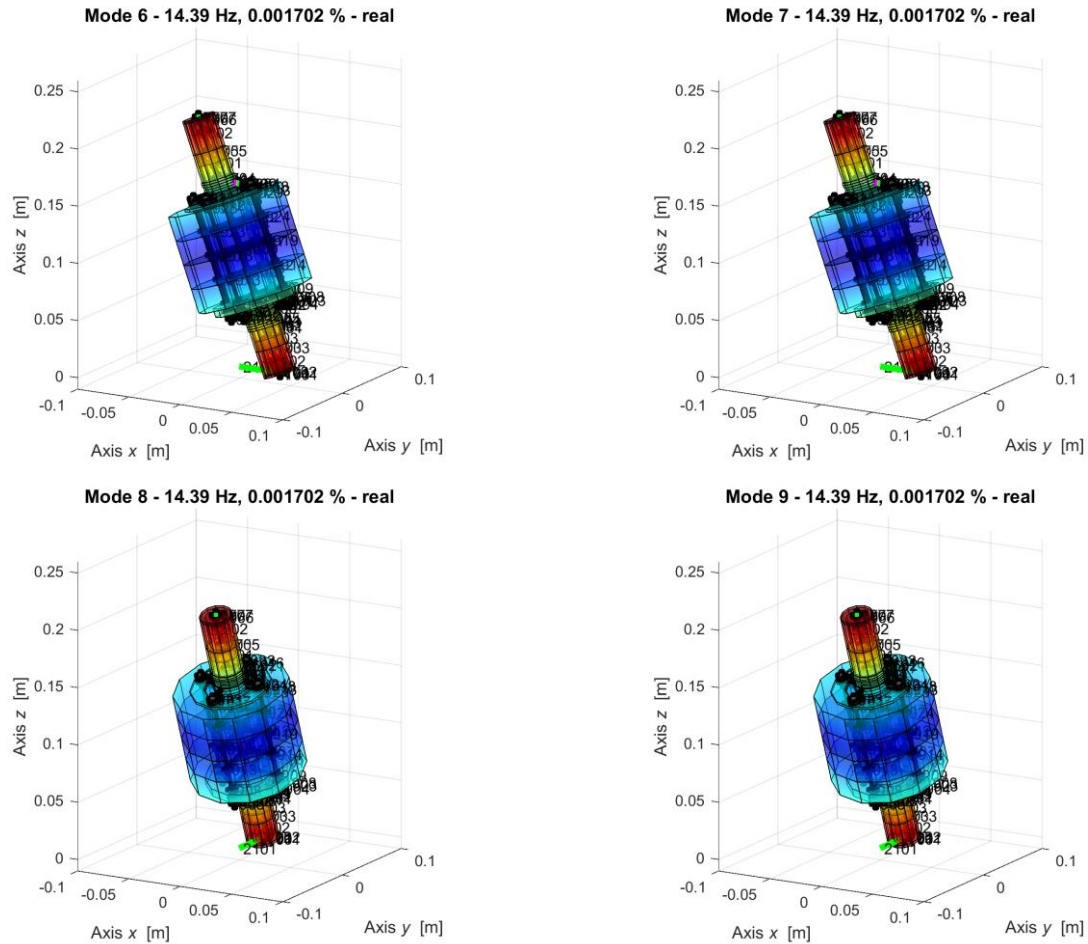
Figure 6.2.2.3.1 – Conical modes.
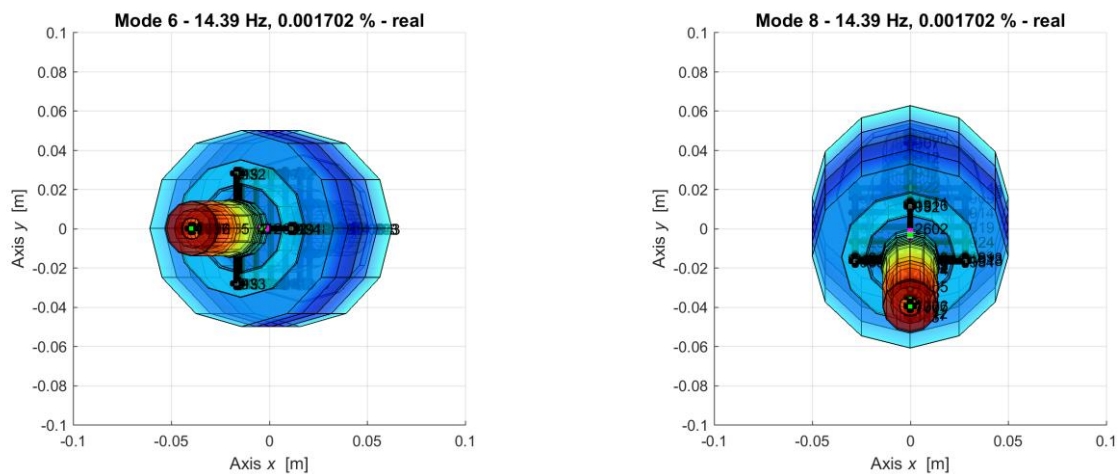
Figure 6.2.2.3.2 – Conical modes in XY plane.

6.2.2.4 Underdamped modes

At high speeds of rotation, we can encounter two different ways which represent an under-damping of the rotor. These occur at a frequency of 229.8 Hz.
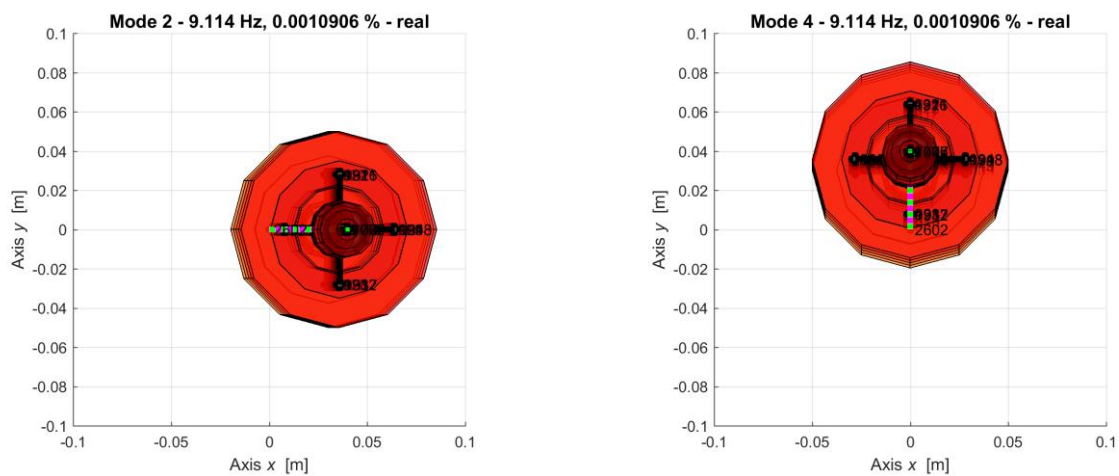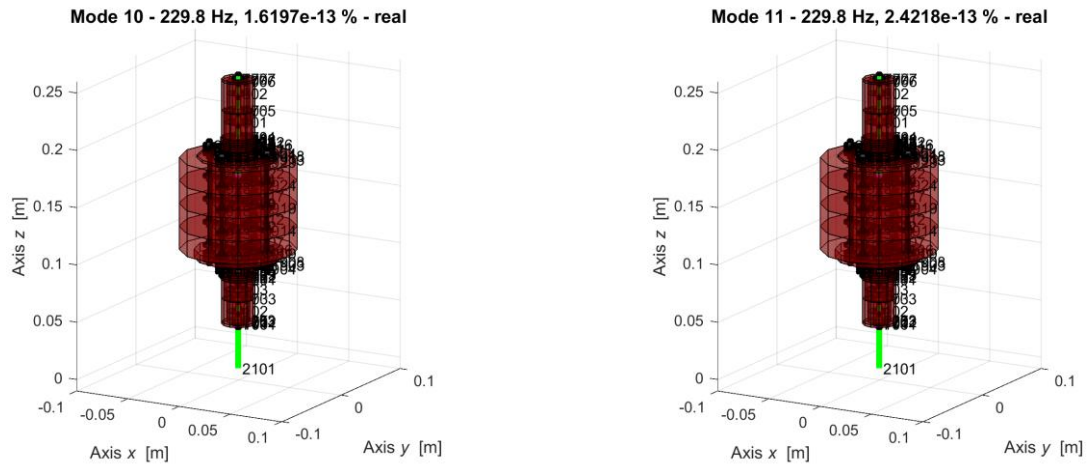

Figure 6.2.2.4.1 – Shaking modes.

As seen previously, they correspond to a shaking of the rotor in the direction of rotation speed. The Table 6.2.2.4.1 shows the critical speeds and frequencies for each mode.

Table 6.2.2.4.1 – Critical speeds.

Modes	Ω [rad/s]	f_n [Hz]
1	0	0
2	57.26	9.114
3	57.26	9.114
4	57.26	9.114
5	57.26	9.114
6	90.42	14.39
7	90.42	14.39
8	90.42	14.39
9	90.42	14.39
10	1443.88	229.8
11	1443.88	229.8
12	0	0

6.2.3 Numerical integration of linear equation of motion

As seen above with the mass matrix, with stiffness matrix, with damping matrix and with that of gyroscopic, defined in the paragraph 6.1.4.5, obtained with the fem analysis in LUPOS, we have moved to the simulation of the magnetic rotor in Simulink.

Figure 6.2.3.1 – Model of equation 2.5 with damping.

With the same boundary conditions as in the non-damped case, we want to analyse the various aspects of the rotor as the rotational speed decreases. In this case the reduction of the rotation speed has an exponential trend as shown in Figure 6.2.3.2.
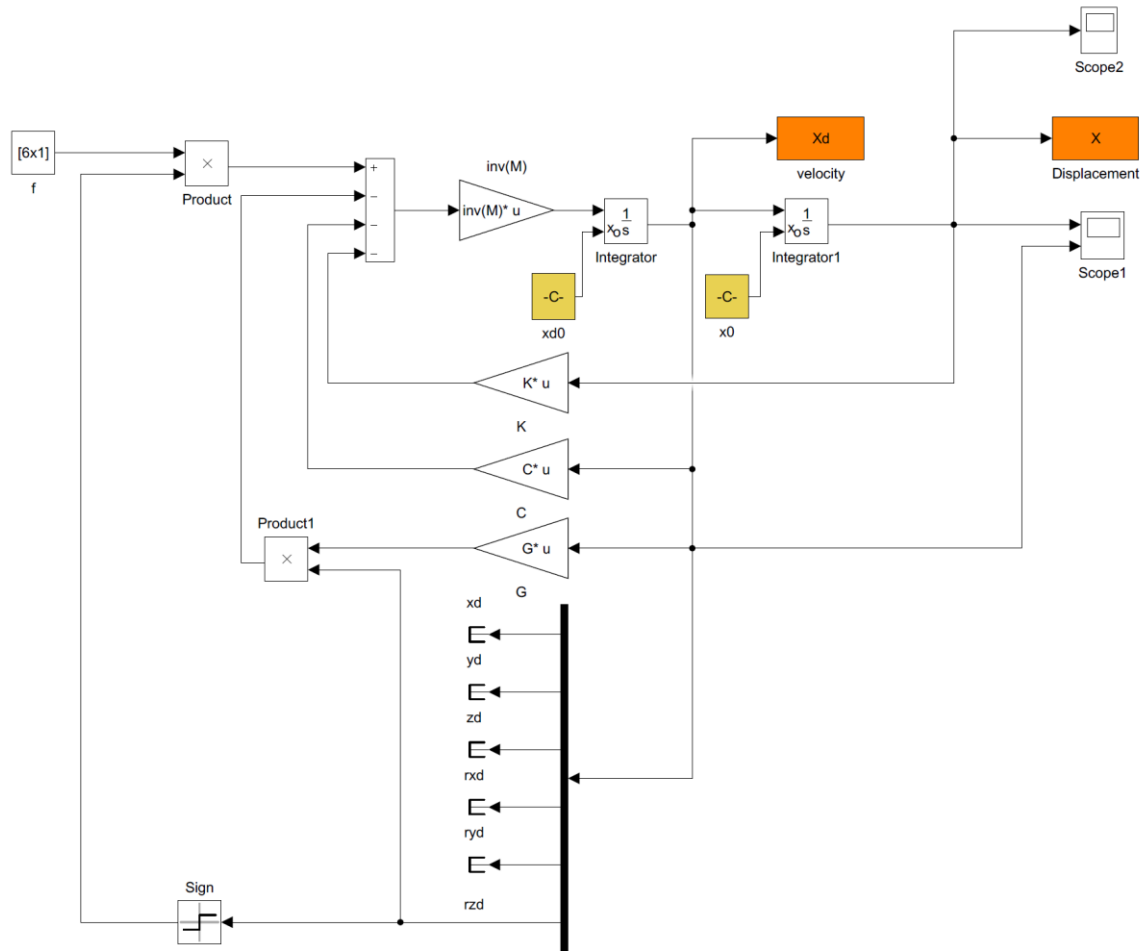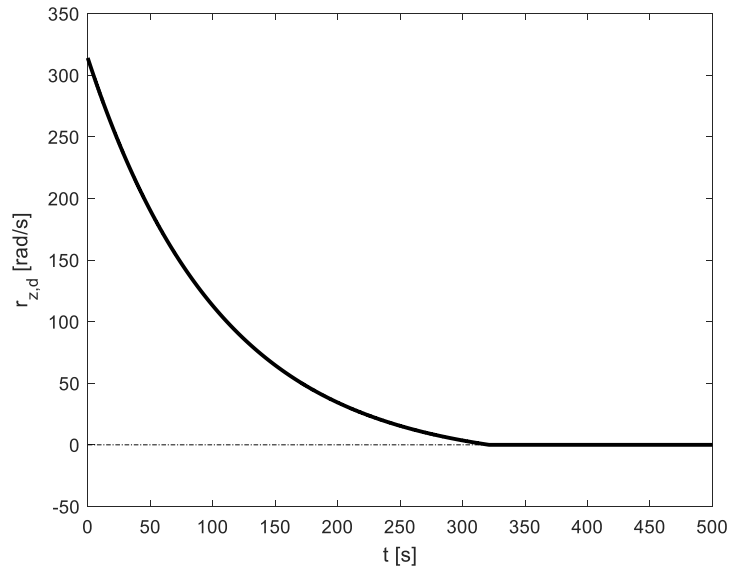
Figure 6.2.3.2 – Speed trend.

If we analyse the time displacement of the centre of mass along the rotation axis as can be seen in this case (Figure 6.2.3.3), the oscillatory tendency will decrease over time due to damping. The displacements are infinitely small and therefore we can consider the position of the rotor along z constant.
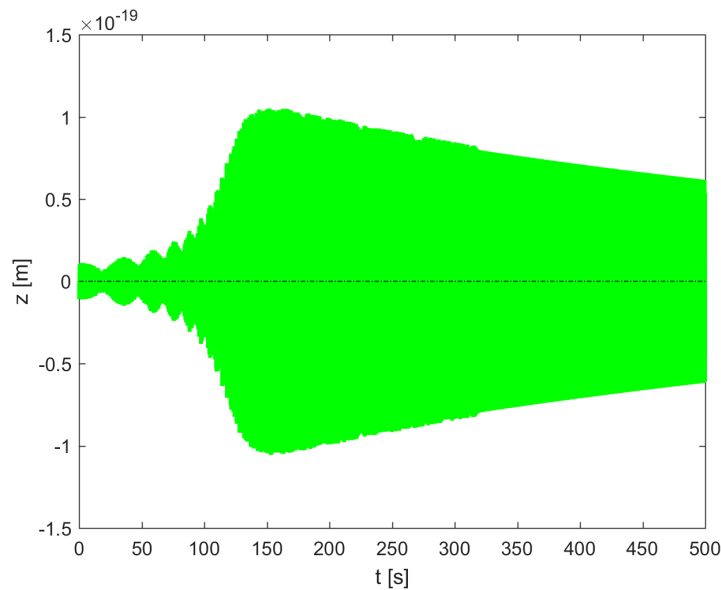
Figure 6.2.3.3 – Displacement of the centre of mass over time.

With the addition of damping, the trajectory of the rotor in the XY plane produces the typical trajectory in which the rotor goes from one end to the other, but as the Figure 6.2.3.4 shows, the number of displacements is much smaller than in the case without damping and therefore the rotor is destined to stabilize. Furthermore, the figure shows the trajectory in three different moments. In green the trajectory is at the beginning of the simulation and the movement of the rotor can be noticed from one position to the other with a minimum rotational component. As time passes and the speed decreases, the figure shows the typical flower petals trajectory.
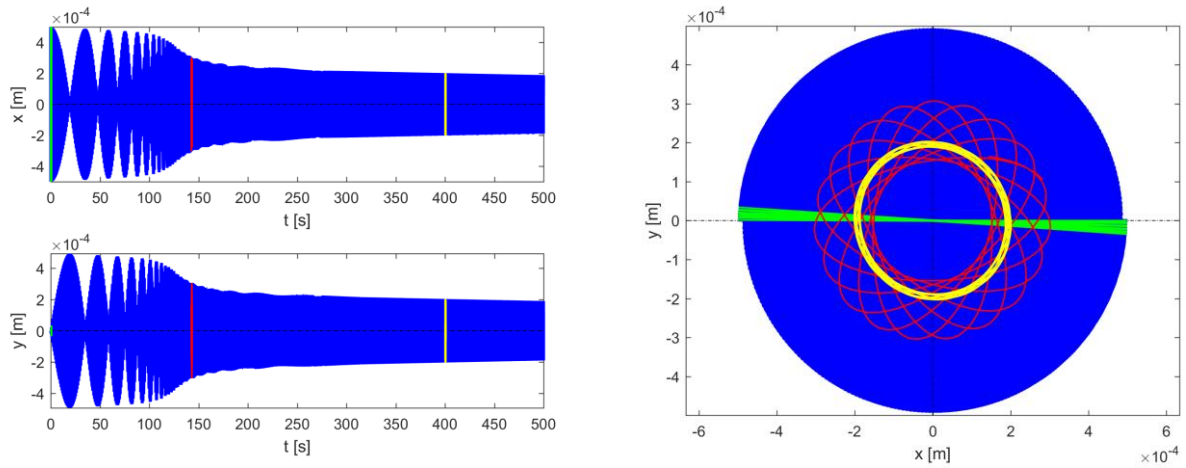
Figure 6.2.3.4 – Displacement x-y.

With the damping of the system, the small rotating oscillations that occur in the other two main directions are reduced over time as shown in Figure 6.2.3.5.
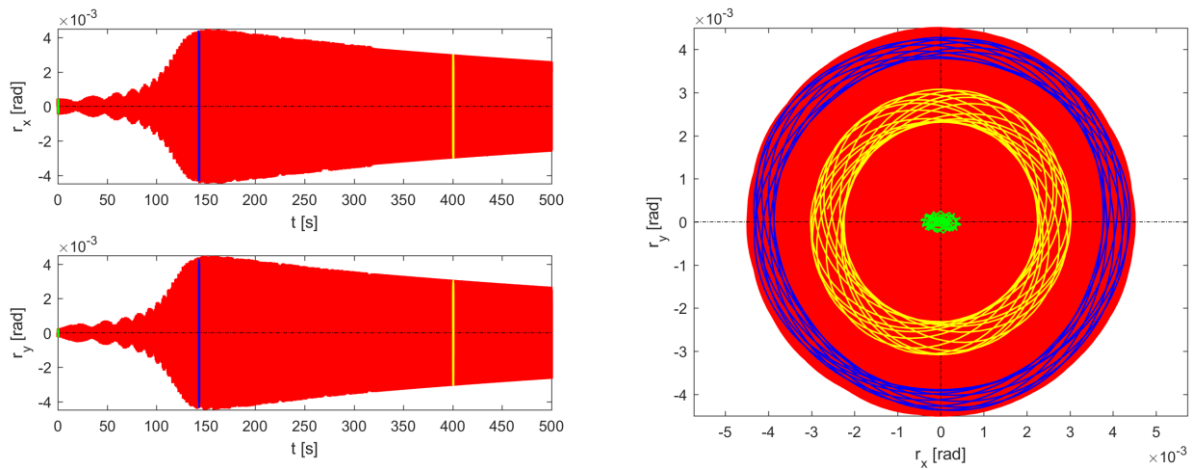
Figure 6.2.3.5 – Rotation rx-ry.

At 156 seconds we can see the maximum peak of rotation in both directions. This value is found in correspondence with one of the modes of vibration. In fact, at 156 seconds the rotor has a rotation speed of about 61.3 rad / s corresponding to 9.114 Hz.

6.3 Campbell diagram

Usually, the dynamic study of rotors is performed under the assumption that the angular velocity about the axis of rotation, usually referred to as spin speed, is constant, at least in its average value. Because the natural frequencies of a rotor can depend on the spin speed, the dynamic behaviour of such systems is usually summarized by a plot of the natural frequencies as functions of the rotational speed, obtaining what is generally known as a Campbell diagram.

The cylindrical whirl is not possible to see it because with respect to the centre of mass it corresponds to a rotation. Furthermore, this is supported by the graph in the Figure 6.3.1.

This represents the Campbell diagram where it is a plot of the real and imaginary part of eigenvalues s versus the rotor speed Ω.

With the analysis of these two parts, it is possible to analyse the stability of the rotor and to identify forward whirl and backward whirl motion, which correspond to the case of precession having the same sign or opposite sign respect to the rotor spin velocity ω respectively.

Stability depends on the sign of the real part of **s** if:

- $\sigma \leq 0$ – rotor is stable;
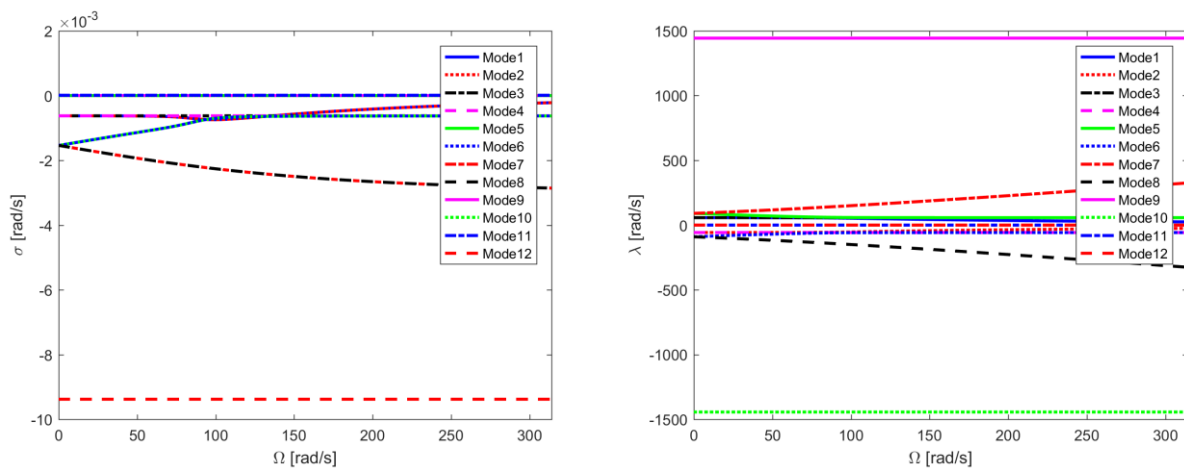- $\sigma > 0$ – rotor is unstable.

Figure 6.3.1 – Real (left) and imaginary (right) parts of the complex whirl frequency as functions of the spin speed in nondimensional form.
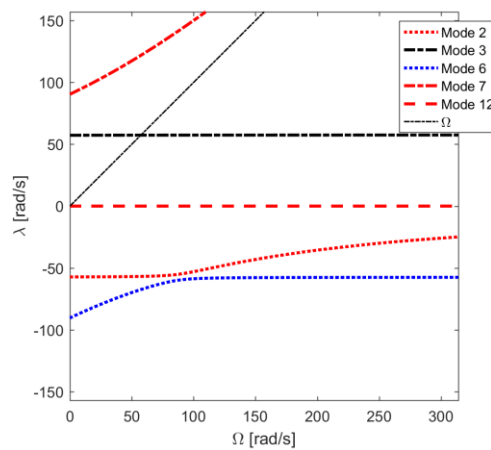
Figure 6.3.2 – Imaginary parts of the complex whirl frequency and spin speed.

It is interesting to note how the line representing the course of angular velocity crosses the diagram in a single curve at the point corresponding to a rotation speed equal to 57.26 rad / s and this will be the only visible vibrational mode. (Figure 6.3.2).

It is interesting to note how the vibrating modes change their frequency as the rotor speed increases.
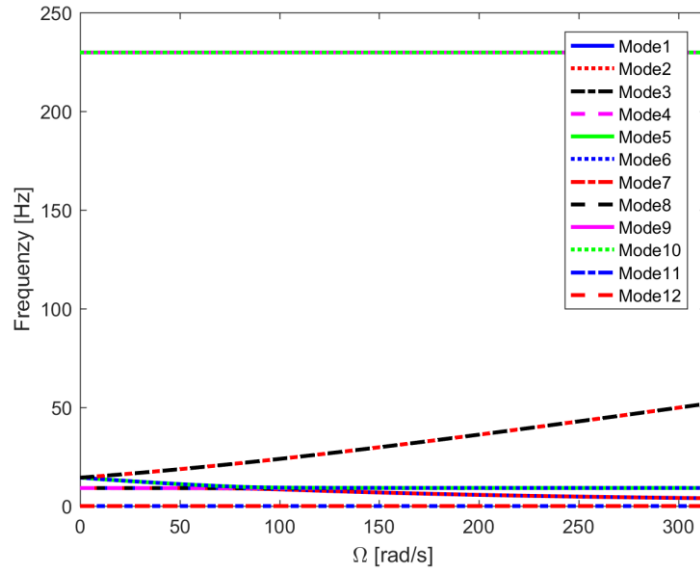
Figure 6.3.3 – Whirl frequency and spin speed.

Through the implementation of LUPOS with the gyroscopic model, we were able to easily notice the phenomenon of veering between two different pairs of modes. This phenomenon is due to a strong coupling between modes 1 and 2 and those 5 and 6, whereas the speed of rotation increases the modes feel the presence of the others and interact by exchanging that is, the cylindrical ones become conical and vice versa.
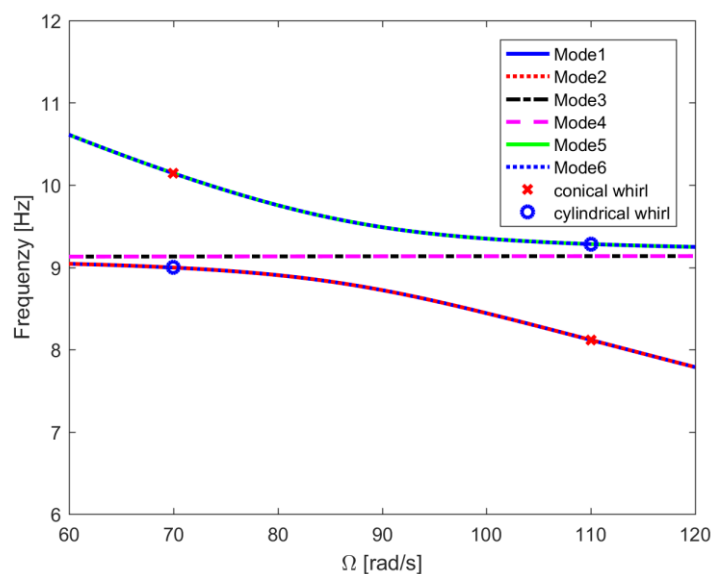
Figure 6.3.4 – Veering phenomena.

Mode 1 and 2 which at low rotation speeds correspond to two cylindrical modes (Figure 6.3.5), at speeds greater than 90 rpm they become conical modes (Figure 6.3.6).
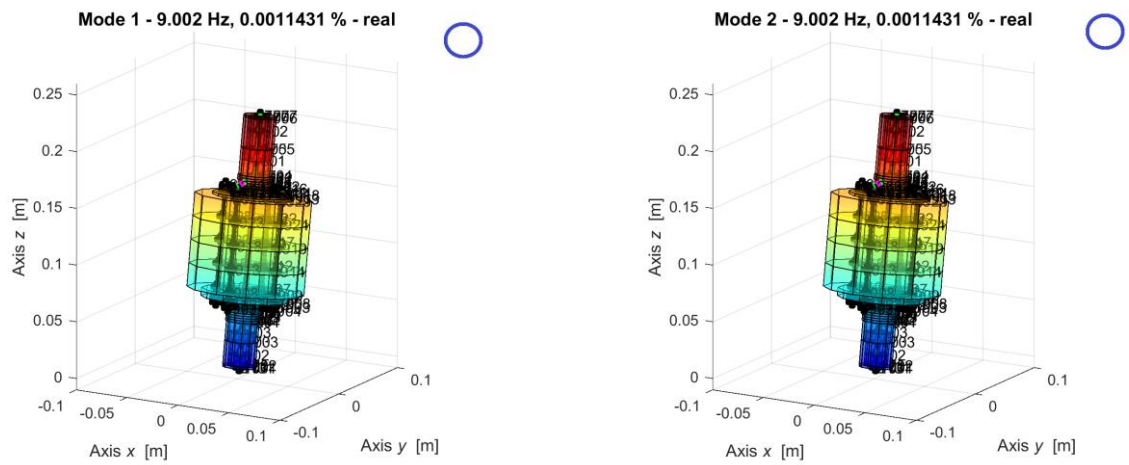
Figure 6.3.5 – Mode 1 and mode 2 at 70 rpm (cylindrical mode).
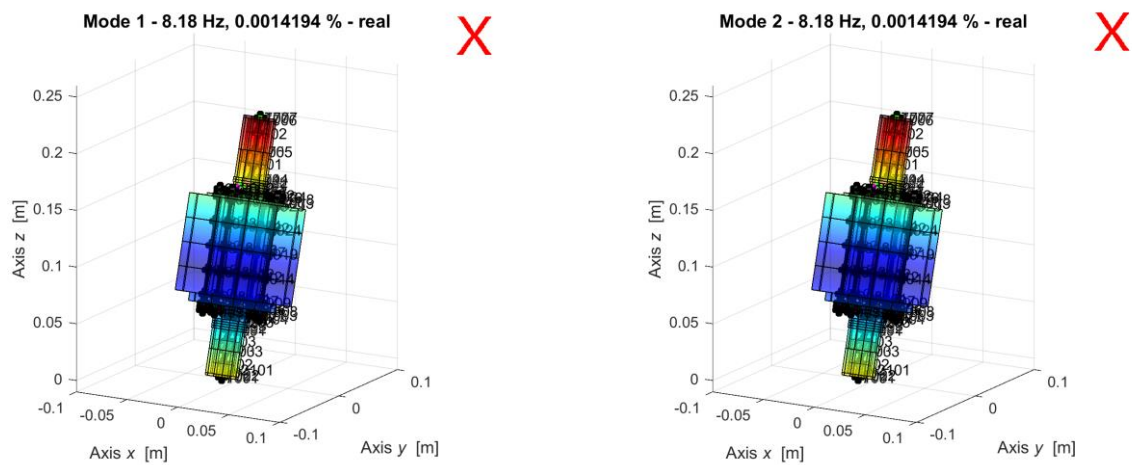
Figure 6.3.6 – Mode 1 and mode 2 at 110 rpm (conical mode).

On the contrary, modes 5 and 6 at low speeds correspond to conical modes (Figure 6.3.7) which at high-speed turn becoming cylindrical (Figure 6.3.8).
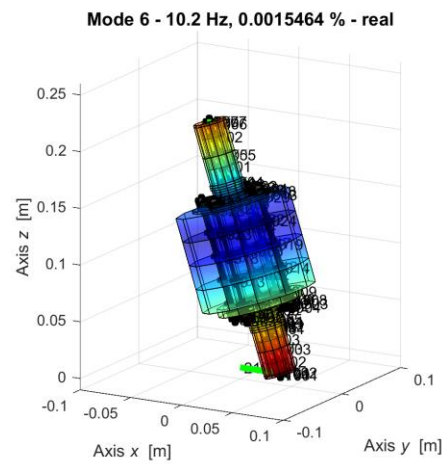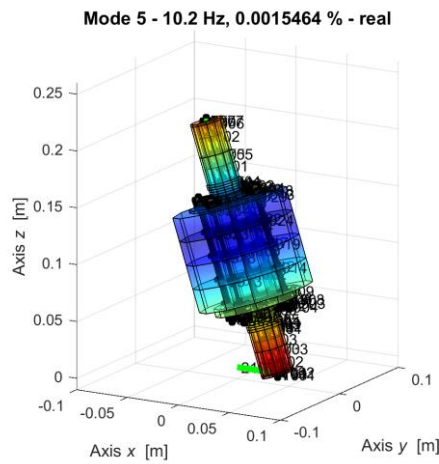
Figure 6.3.7 – Mode 5 and mode 6 at 70 rpm (conical mode).

Figure 6.3.8 – Mode 5 and mode 6 at 110 rpm (cylindrical mode).

It is interesting to note that modes 3 and 4 have no interaction with the others although they have a conical whirl and therefore remain so as the rotor speed increases.

7. Equations of motion – Linear behaviour

The real world is, however, generally non-linear, and the use of linear models is always a source of approximation.

The behaviour of a non-linear system can be qualitatively different from that of the corresponding linearized system, and therefore the behaviour in the large can differ significantly from the behaviour in the small.
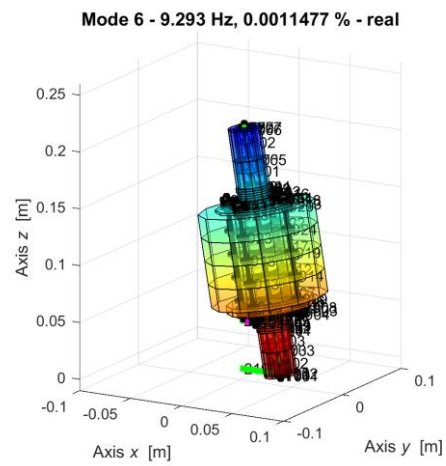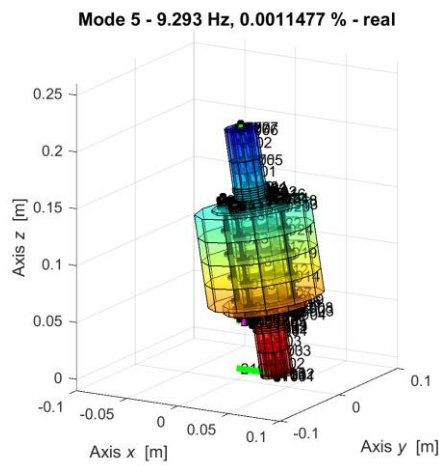
In this second phase, to obtain the real behaviour of the rotor motion, these forces have been considered with a non-linear behaviour.

The equation of the matrix becomes:

$$\mathbf{M\ddot{x}} + \left(\mathbf{C} + \Omega\mathbf{G}\right)\mathbf{\dot{x}} + \mathbf{Kx} + \mathbf{F_{nl}} = \mathbf{F} \tag{7.1}$$

where:

- **M** is the mass matrix $(n \times n)$;
- **C** is the damping matrix $(n \times n)$;
- **G** is the gyroscopic matrix $(n \times n)$;
- **K** is the stiffness matrix $(n \times n)$;
- **$\mathbf{F_{nl}}$** is the non-linear forces matrix $(n \times 1)$;
- **F** is the external forces matrix $(n \times 1)$;
- **$\mathbf{x, \dot{x}, \ddot{x}}$** are respectively the generalized displacements, the velocities and accelerations of the only active degrees of freedom.

7.1 Non-linear forces and torques

7.1.1 Lower magnetic bearings

By applying the laws of magnetic interaction, the forces and torques exchanged between the stator magnets and the rotor ones along the three directions have been calculated.

The modulus of forces depends on the relative distance between the centres of the two groups of magnets. Therefore, after having established the value of this distance along the rotor's axis of rotation, it has passed to the evaluation of the forces in the plane.
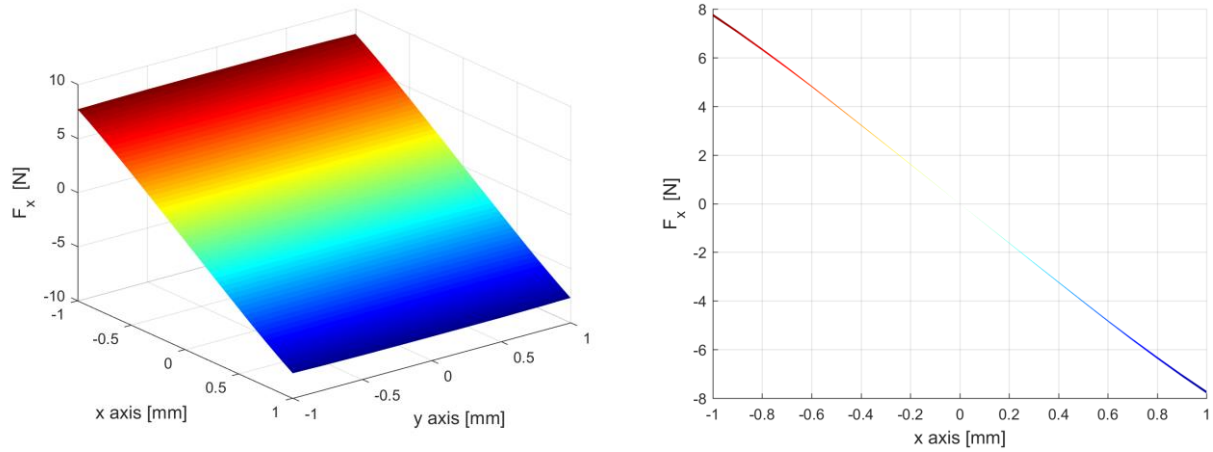
Figure 7.1.1.1 – Force along the x axis.
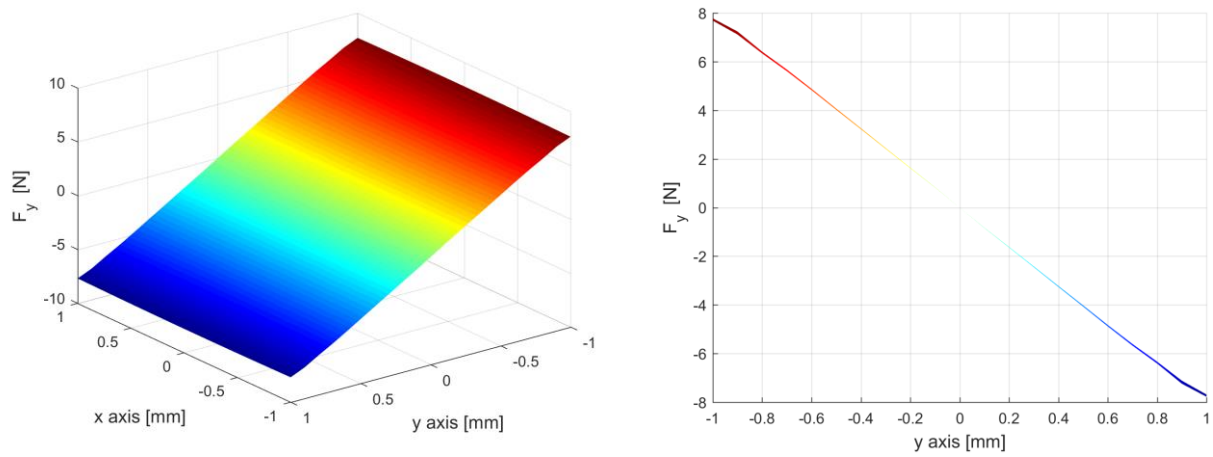
Figure 7.1.1.2 – Force along the y axis.

In the case of our interest, due to the axial symmetry of the magnetic rotor, the forces evaluated along one of the two main directions will be equal to the force evaluated along any generic direction. So, as you can see in the Figure 7.1.1.3 the strength module will be the same at any point that is at the same distance from the centre.
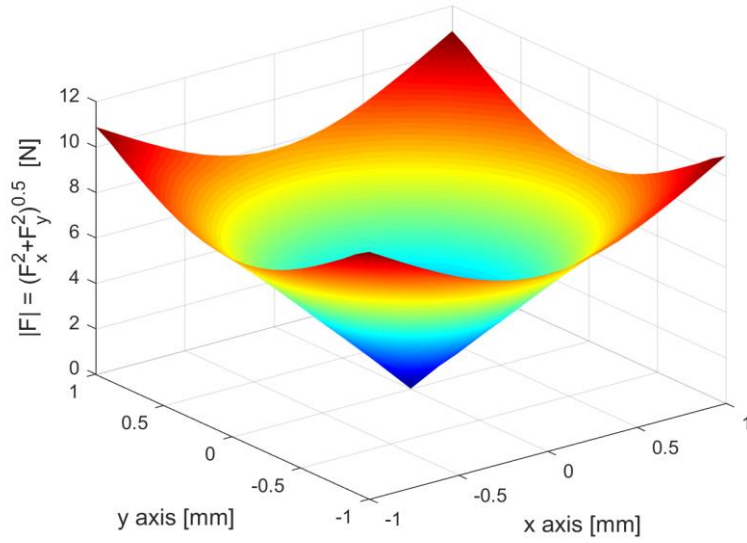
Figure 7.1.1.3 – Radial force of lower bearing.

Analysing the component of the magnetic interaction forces obtained along the vertical axis, this is also dependent on the relative position of the magnets in the plane. With the approach of the rotor rings to the stator ones, the modulus of the upward thrust force increases.
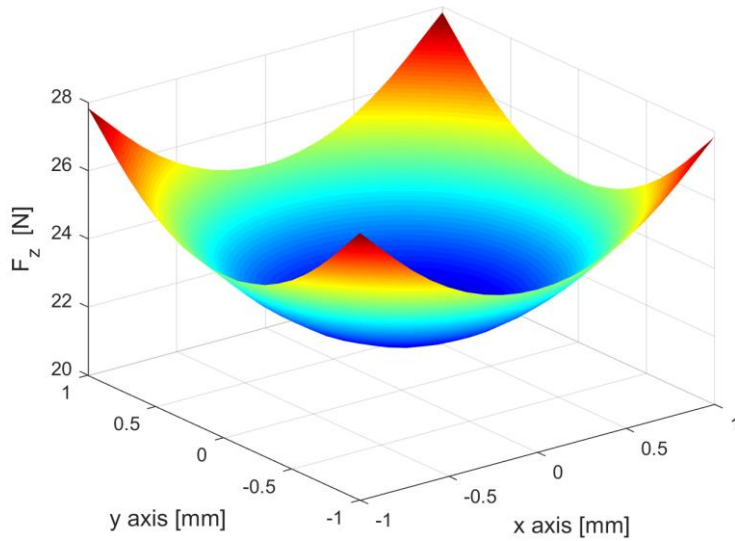
Figure 7.1.1.4 – Force along the z axis.

Similarly, to what we have seen for the forces, also the torques in the three main directions depend on the relative position of the two centres of the magnetic groups. The more the two centres will be distant from each other, the greater the modulus of the torque in the direction orthogonal to the displacement occurred. In fact, as shown in the Figure 7.1.1.5 and Figure 7.1.1.6 the module of the pair T_x grows at a distance in two centres in the y direction and vice versa.
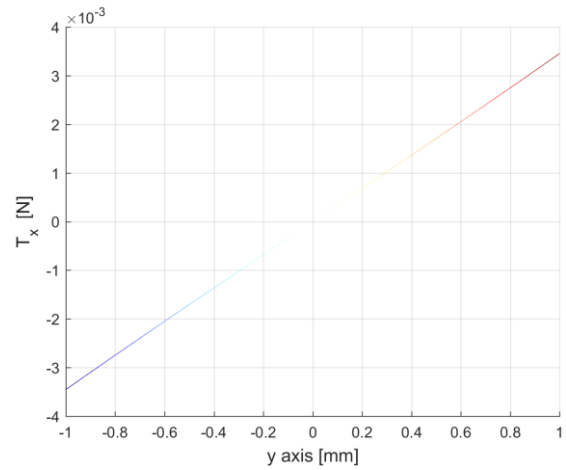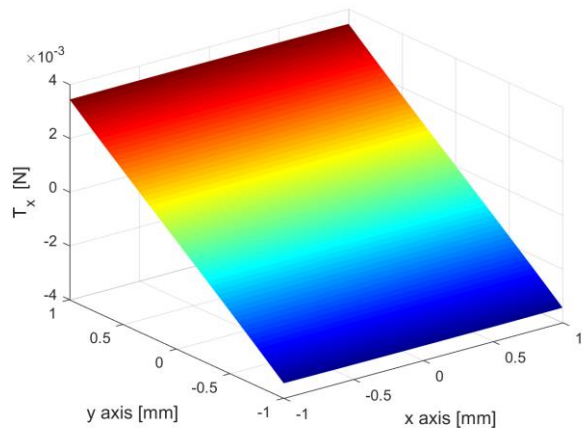
Figure 7.1.1.5 – Torque along the x axis.
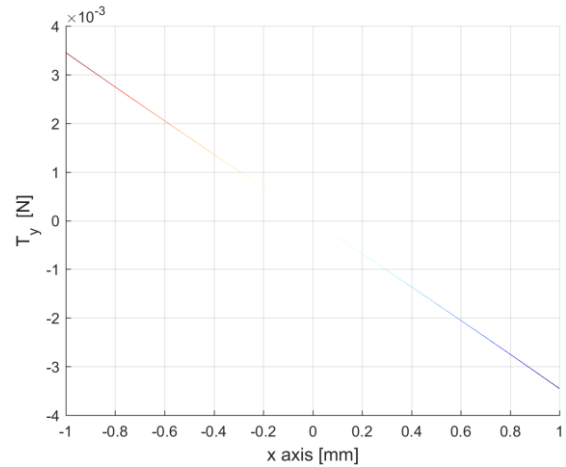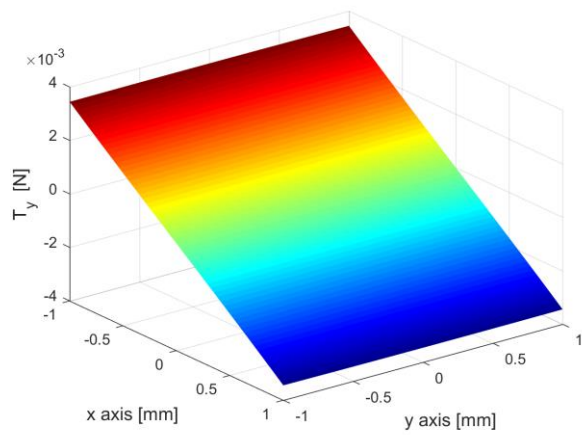
Figure 7.1.1.6 – Torque along the y axis.

The Figure 7.1.1.7 also shows the pairs along the vertical axis. As can be seen, these do not depend on the displacement of the centres of the magnets in the plane and are all null.
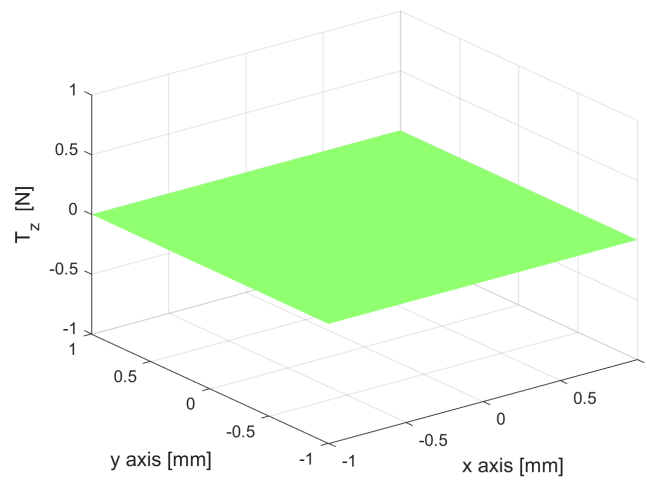
Figure 7.1.1.7 – Torque along the z axis.

7.1.1.1 Fit a polynomial surface

In order to consider, the non-linearity of the magnetic forces in the rotor bearings, we proceeded with a non-linear regression.
As a first approach a generic formulation of the force was considered with a polynomial of the fifth order of the equation 7.2 that is represented by the surface in Figure 7.1.1.1.1.

$$
\begin{aligned}
F(x, y) = {} & k_{0,0} + k_{1,0} \cdot x + k_{0,1} \cdot y + k_{2,0} \cdot x^2 + k_{1,1} \cdot xy + k_{0,2} \cdot y^2 + k_{3,0} \cdot x^3 + k_{2,1} \cdot x^2 y + \\
& + k_{1,2} \cdot xy^2 + k_{0,3} \cdot y^3 + k_{4,0} \cdot x^4 + k_{3,1} \cdot x^3 y + k_{2,2} \cdot x^2 y^2 + k_{1,3} \cdot xy^3 + k_{0,4} \cdot y^4 + \\
& + k_{5,0} \cdot x^5 + k_{4,1} \cdot x^4 y + k_{3,2} \cdot x^3 y^2 + k_{2,3} \cdot x^2 y^3 + k_{1,4} \cdot xy^4 + k_{0,5} \cdot y^5
\end{aligned}
\tag{7.2}
$$
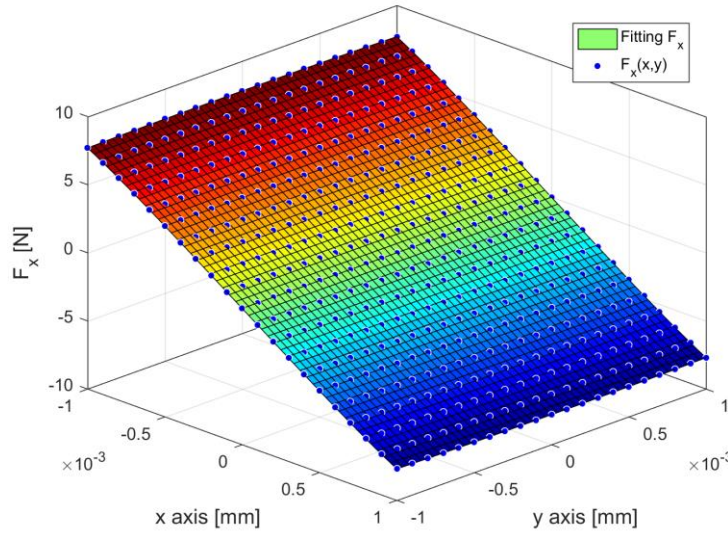
Figure 7.1.1.1.1 – Fit a polynomial surface.

The stiffness coefficients found in the Table 7.1.1.1.1 are those related to odd order terms. The coefficient of the stiffness of the term of the first order is the same one found considering the linearized magnetic force, while the other coefficients are those that underline the dependence of the magnetic force both on the distance in x and on the distance in y.

Table 7.1.1.1.1 – Coefficients of force along x direction.

Stiffness coefficients			
$k_{0,0}$	$-8.13 \cdot 10^{-17}$	$k_{3,1}$	-0.00029
$k_{1,0}$	-8141	$k_{2,2}$	0.00038
$k_{0,1}$	$4.881 \cdot 10^{-13}$	$k_{1,3}$	$5.025 \cdot 10^{-5}$
$k_{2,0}$	$5.233 \cdot 10^{-9}$	$k_{0,4}$	0.00228
$k_{1,1}$	$1.014 \cdot 10^{-10}$	$k_{5,0}$	$2.152 \cdot 10^{14}$
$k_{0,2}$	$-1.598 \cdot 10^{-9}$	$k_{4,1}$	2.37

$k_{3,0}$	$1.246 \cdot 10^8$	$k_{3,2}$	$2.946 \cdot 10^{13}$
$k_{2,1}$	$-2.207 \cdot 10^{-6}$	$k_{2,3}$	0.1869
$k_{1,2}$	$3.393 \cdot 10^7$	$k_{1,4}$	$4.353 \cdot 10^{13}$
$k_{0,3}$	$-1.317 \cdot 10^{-6}$	$k_{0,5}$	1.023
$k_{4,0}$	-0.00632		

Through the generalized polynomial, we could note the dependence of magnetic forces only on the odd order terms and for this reason we formulated the equation 7.3 that represents the polynomial with which the fitting will be performed. It is constituted by all the possible combinations of terms in x, y and $\rho^2 = \left(x^2 + y^2 \right)$ which represent the distance between the two magnetic groups.

The first subscript represents the degree of the term x, the second subscript the degree of the term y, while the third that of ρ.

$$
\begin{aligned}
F(x,y) = {} & k_{100} \cdot x + k_{010} \cdot y + k_{300} \cdot x^3 + k_{030} \cdot y^3 + k_{210} \cdot x^2 y + k_{120} \cdot xy^2 + k_{101} \cdot x \left(x^2 + y^2 \right) + \\
& + k_{011} \cdot y \left(x^2 + y^2 \right) + k_{500} \cdot x^5 + k_{410} \cdot x^4 y + k_{320} \cdot x^3 y^2 + k_{301} \cdot x^3 \left(x^2 + y^2 \right) + k_{230} \cdot x^2 y^3 + \\
& + k_{211} \cdot x^2 y \left(x^2 + y^2 \right) + k_{140} \cdot xy^4 + k_{121} \cdot xy^2 \left(x^2 + y^2 \right) + k_{102} \cdot x \left(x^2 + y^2 \right)^2 + k_{050} \cdot y^5 + \\
& + k_{031} \cdot y^3 \left(x^2 + y^2 \right) + k_{012} \cdot y \left(x^2 + y^2 \right)^2
\end{aligned}
\tag{7.3}
$$

Figure 7.1.1.1.2 – Fitting with a new surface polynomial.
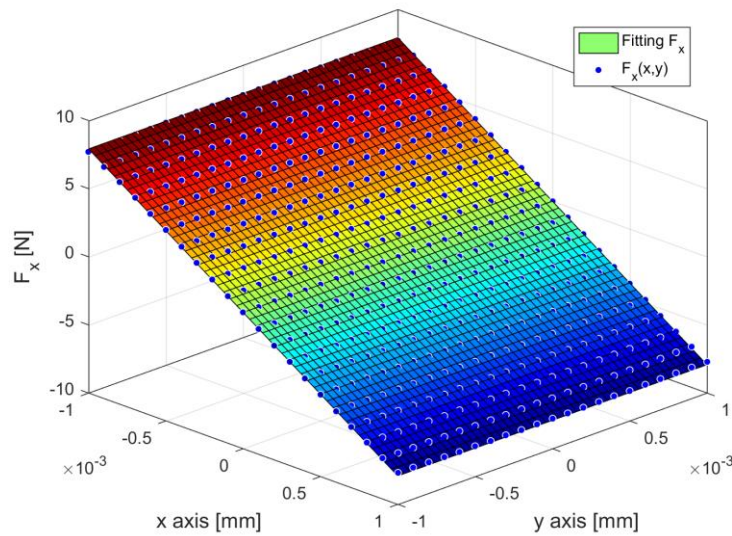
Since with this formulation there is the redundancy of some terms, the polynomial with which the curve fitting has been done contains only the terms present in Table 7.1.1.1.2

Table 7.1.1.1.2 – Coefficients of generic force.

Stiffness coefficients			
k_{100}	-8148	k_{211}	0
k_{010}	$-2.299 \cdot 10^{-9}$	k_{121}	0

k_{101}	$2.237 \cdot 10^8$	k_{102}	0
k_{011}	0.00224	k_{031}	$9.52 \cdot 10^{-12}$
k_{301}	0	k_{012}	$9.52 \cdot 10^{-12}$

The goodness of the fit can be assessed through four parameters:

- The sim of squares due to error (SSE);
- R-square;
- Adjusted R-square;
- Root mean squared error (RMSE).

The SSE is a statistical measure of the total deviation of the response values from the fit to the response values. A value closer to 0 indicates that the model has a smaller random error component, and that the fit will be more useful for prediction.

R-square is the square of the correlation between the response values and the expected response values. R-square can take on any value between 0 and 1, with a value closer to 1 indicating that a greater proportion of variance is accounted for by the model.

This statistic uses the R-square statistic defined above, and adjusts it based on the residual degrees of freedom. The adjusted R-square statistic can take on any value less than or equal to 1, with a value closer to 1 indicating a better fit.

This statistic is also known as the fit standard error and the standard error of the regression. It is an estimate of the standard deviation of the random component in the data. Just as with SSE, an RMSE value closer to 0 indicates a fit that is more useful for prediction.

The Table 7.1.1.1.3 shows the values of the fitting performed.

Table 7.1.1.1.3 – Fitting of radial force.

Goodness of fit	
SSE	0.723
R-square	0.9999
Adjusted R-square	0.9999
RMSE	0.0410

The polynomial of the equation 3.1 is used to determine the rigidity coefficients of forces along y. These coefficients must be equal to those obtained for F_x in the x direction due to the radial symmetry of the rotor.
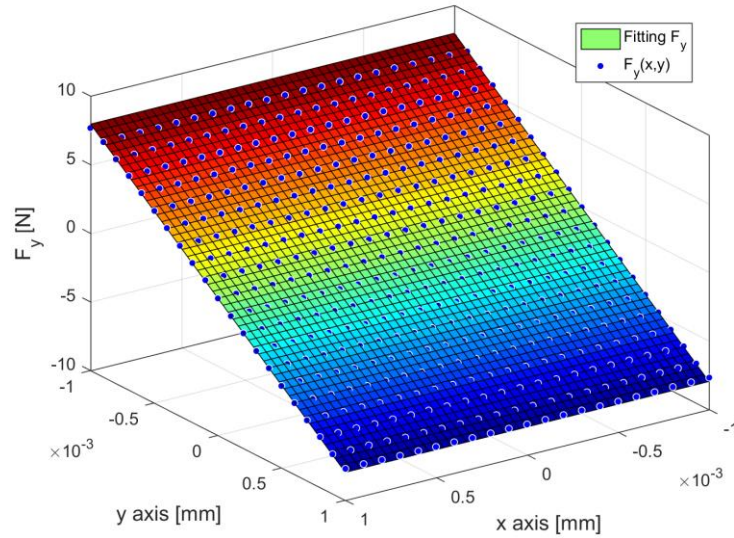
Figure 7.1.1.1.3 – Fitting with a surface polynomial of forces along y.

Table 7.1.1.1.4 – Coefficients of generic force.

Stiffness coefficients			
k_{100}	$-1.735 \cdot 10^{-9}$	k_{211}	0
k_{010}	-7963	k_{121}	0
k_{101}	0.00169	k_{102}	$8.755 \cdot 10^{-20}$
k_{011}	-0.00430	k_{031}	0
k_{301}	$8.755 \cdot 10^{-20}$	k_{012}	0

Comparing Table 7.1.1.1.2 with Table 7.1.1.1.4 the coefficients representing the stiffness along the chosen direction are not equal. For this reason, we evaluate the absolute and relative error between the forces in the two main directions of the plane.

As can be seen in the Figure 7.1.1.1.4, the two surfaces representing radial forces in two different directions are slightly different. This causes the diversity of the stiffness coefficients. Since the error is still very small, it was decided to use the coefficients found with the fitting on the values of the forces along the x direction.
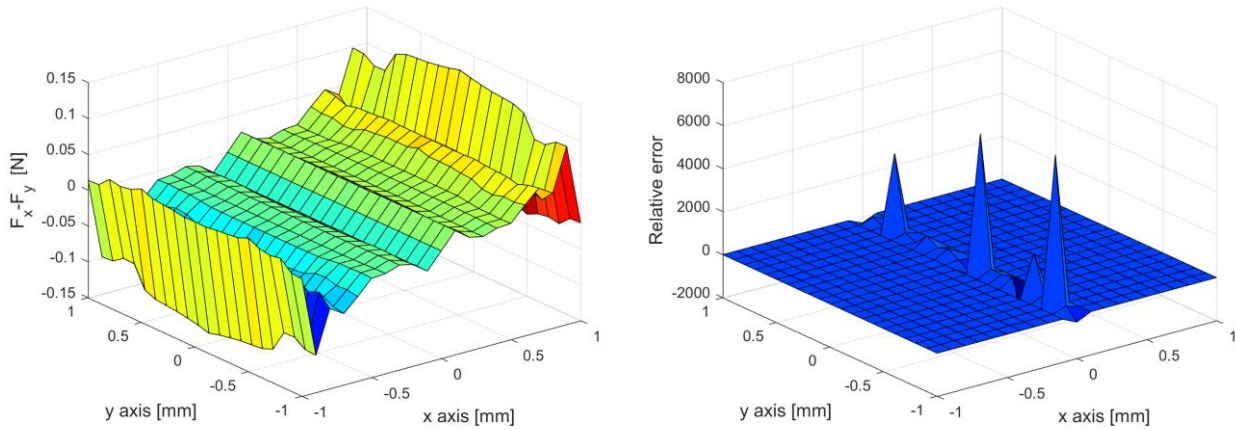
Figure 7.1.1.1.4 – Absolute and relative error between the forces in two directions.

Similarly, to what was done for the exchanged forces of the magnets in the radial direction, we proceeded with a non-linear regression.

In a first approach the complete polynomial was used in the equation. Here it was possible to notice the strong dependence of the axial force with an even order terms of the distance between the two centres of the magnets (Table 7.1.1.1.5).
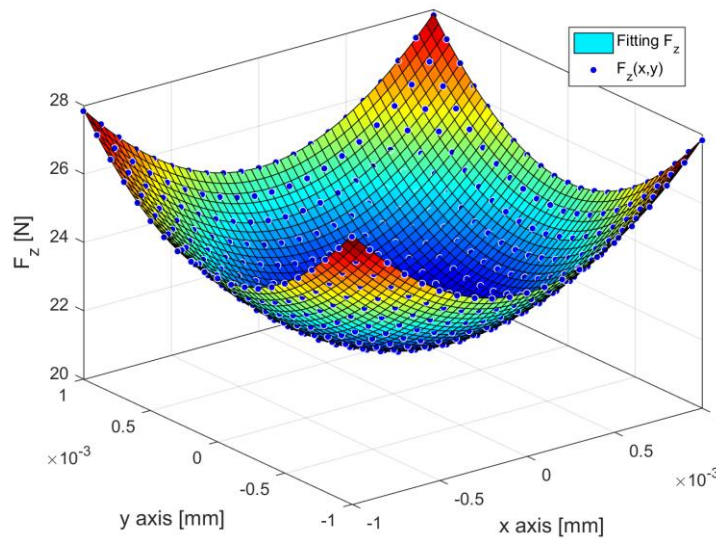
Figure 7.1.1.1.5 – Force along the z axis.

Table 7.1.1.1.5 – Coefficients of force along z direction.

Stiffness coefficients			
$k_{0,0}$	21.64	$k_{3,1}$	0.00898
$k_{1,0}$	$-1.546 \cdot 10^{-11}$	$k_{2,2}$	$-2.857 \cdot 10^{10}$
$k_{0,1}$	$-8.584 \cdot 10^{-12}$	$k_{1,3}$	0.00862
$k_{2,0}$	$3.248 \cdot 10^{6}$	$k_{0,4}$	$-1.473 \cdot 10^{11}$
$k_{1,1}$	$-7.666 \cdot 10^{-9}$	$k_{5,0}$	0.8648

$k_{0,2}$	$3.285 \cdot 10^6$	$k_{4,1}$	-53.08
$k_{3,0}$	$9.405 \cdot 10^{-6}$	$k_{3,2}$	-33.43
$k_{2,1}$	$5.132 \cdot 10^{-5}$	$k_{2,3}$	-14.65
$k_{1,2}$	$4.149 \cdot 10^{-5}$	$k_{1,4}$	-17.96
$k_{0,3}$	$1.145 \cdot 10^{-5}$	$k_{0,5}$	-0.3459
$k_{4,0}$	$-1.206 \cdot 10^{11}$		

Subsequently, for easier calculation and better data processing, the simplified polynomial in the equation 7.4 will be used to perform the regression.

$$F_z(x, y) = k_{000} + k_{110} \cdot xy + k_{200} \cdot x^2 + k_{020} \cdot y^2 + k_{001}\left(x^2 + y^2\right) \tag{7.4}$$

Not considering the coefficients that produce a redundancy in the results we get the values in the Table 7.1.1.1.6, while in the Table 7.1.1.1.7 you can see the goodness of the fitting.

Table 7.1.1.1.6 – Coefficients of force along z direction.

Stiffness coefficients	
k_{000}	21.67
k_{110}	-122.2
k_{001}	$3.131 \cdot 10^6$

Table 7.1.1.1.7 – Fitting of radial axial force.

Goodness of fit	
SSE	0.3474
R-square	0.9996
Adjusted R-square	0.9996
RMSE	0.02813

For the analysis of the transmitted torques the polynomial of equation 7.5 was used, completely analogous to that used for the non-linear regression of radial forces, obtaining the surfaces in Figure 7.1.1.1.6.

Comparing Table 7.1.1.1.8 and Table 7.1.1.1.9, we can see the equalities of the analogous coefficients, due to the perfect radial symmetry of the rotor. This is also demonstrated by the goodness of the fit in the Table 7.1.1.1.10.

$$
\begin{aligned}
T(x, y) = & k_{100} \cdot x + k_{010} \cdot y + k_{300} \cdot x^3 + k_{030} \cdot y^3 + k_{210} \cdot x^2 y + k_{120} \cdot xy^2 + k_{101} \cdot x\left(x^2 + y^2\right) + \\
& + k_{011} \cdot y\left(x^2 + y^2\right) + k_{500} \cdot x^5 + k_{410} \cdot x^4 y + k_{320} \cdot x^3 y^2 + k_{301} \cdot x^3\left(x^2 + y^2\right) + k_{230} \cdot x^2 y^3 + \\
& + k_{211} \cdot x^2 y\left(x^2 + y^2\right) + k_{140} \cdot xy^4 + k_{121} \cdot xy^2\left(x^2 + y^2\right) + k_{102} \cdot x\left(x^2 + y^2\right)^2 + k_{050} \cdot y^5 + \\
& + k_{031} \cdot y^3\left(x^2 + y^2\right) + k_{012} \cdot y\left(x^2 + y^2\right)^2
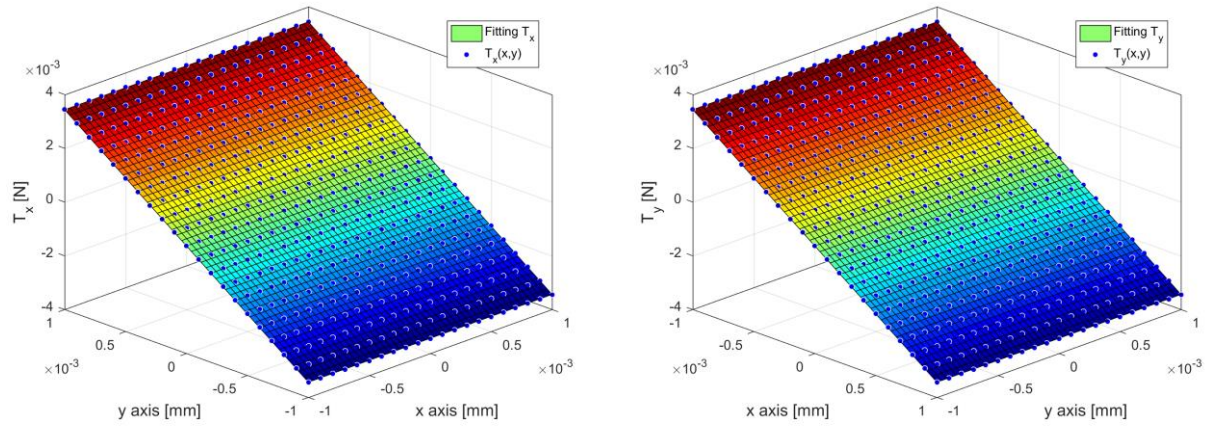\end{aligned} \tag{7.5}
$$

Figure 7.1.1.1.6 – Torques in radial directions.

Table 7.1.1.1.8 – Coefficients for torque along x direction.

Stiffness coefficients			
k_{100}	$6.694 \cdot 10^{-16}$	k_{211}	0
k_{010}	11.31	k_{121}	0
k_{101}	$1.98 \cdot 10^{-10}$	k_{102}	$-8.478 \cdot 10^{-16}$
k_{011}	$3.602 \cdot 10^{5}$	k_{031}	0
k_{301}	$-8.478 \cdot 10^{-16}$	k_{012}	0

Table 7.1.1.1.9 – Coefficients for torque along y direction.

Stiffness coefficients			
k_{100}	-11.24	k_{211}	0
k_{010}	$-3.667 \cdot 10^{-17}$	k_{121}	0
k_{101}	$-1.159 \cdot 10^{-5}$	k_{102}	0
k_{011}	$-6.394 \cdot 10^{22}$	k_{031}	$1.236 \cdot 10^{-29}$
k_{301}	0	k_{012}	$1.236 \cdot 10^{-29}$

Table 7.1.1.1.10 – Goodness of fit for radial torques.

Goodness of fit	
SSE	$8.9582 \cdot 10^{-6}$
R-square	0.9996
Adjusted R-square	0.9996
RMSE	$1.4418 \cdot 10^{-4}$

7.1.2 Upper magnetic bearings

Applying a method like that of the lower magnetic bearing, we analyse first the forces and the pairs of magnetic origin of the upper bearing.

For this reason, two rotor magnets and two stator magnets were used, with the first ones positioned along the vertical axis at 1 mm above the stator ones.

Even if the number of magnets is lower, the magnetic interaction forces between the magnets are of the same order of magnitudes as can be seen in the Figure 7.1.2.1 and Figure 7.1.2.2.
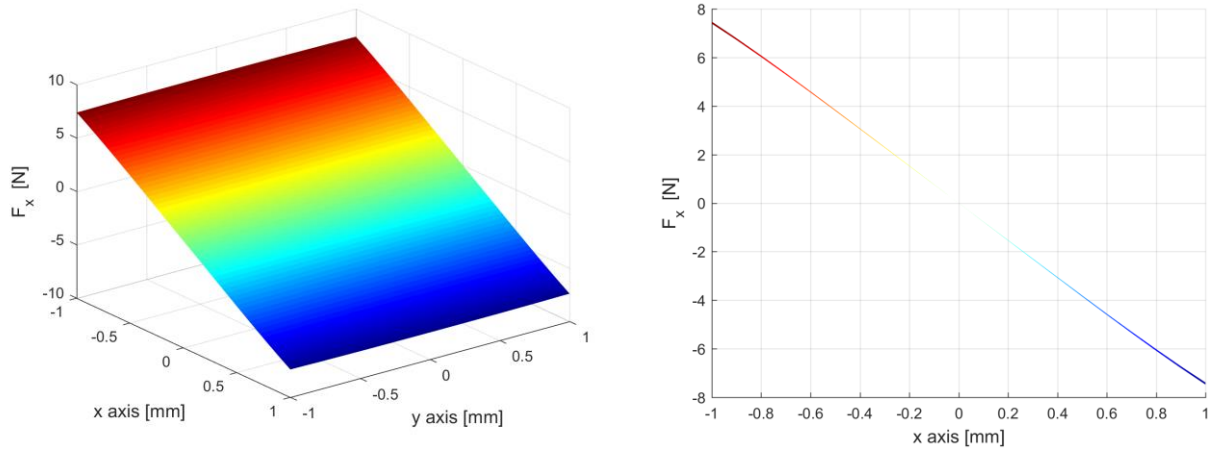

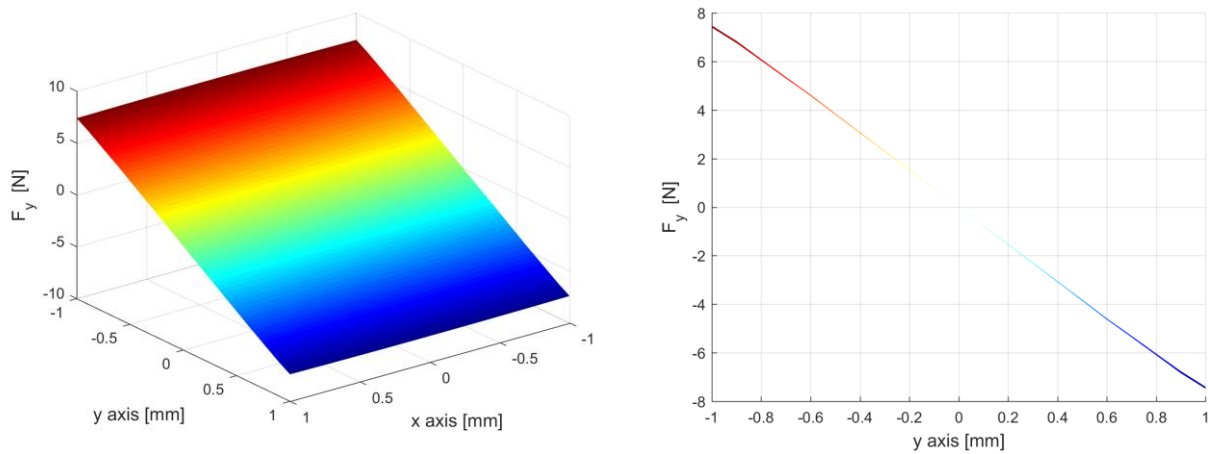Figure 7.1.2.1– Force along the x axis.
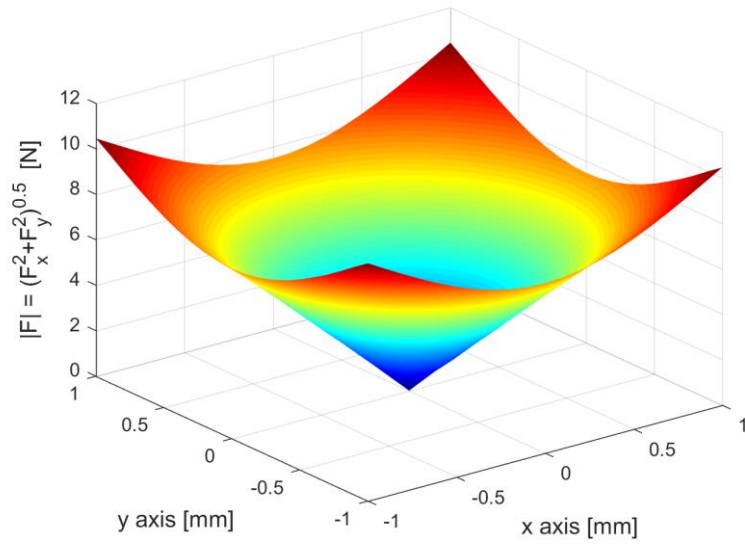

Figure 7.1.2.2 – Force along the y axis.

Figure 7.1.2.3 – Radial force of upper bearing.

Also, in this case, the magnetic interaction forces along the rotation axis are function of the distance in the plane between the two magnets (Figure 7.1.2.4).
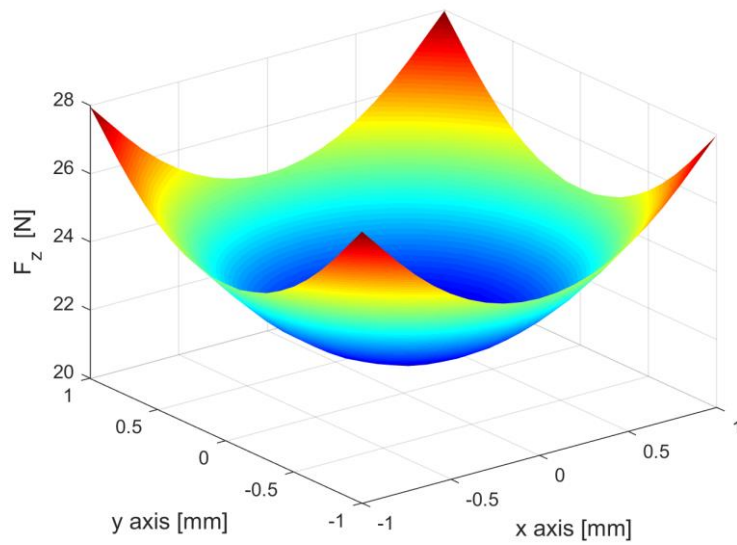

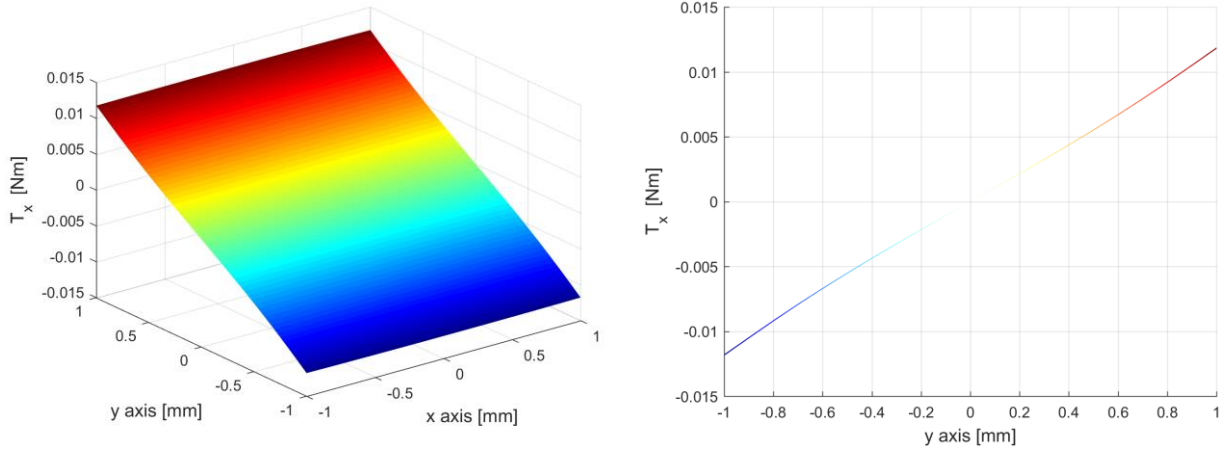Figure 7.1.2.4 – Force along the z axis.

Figure 7.1.2.5 – Torque of upper bearing.
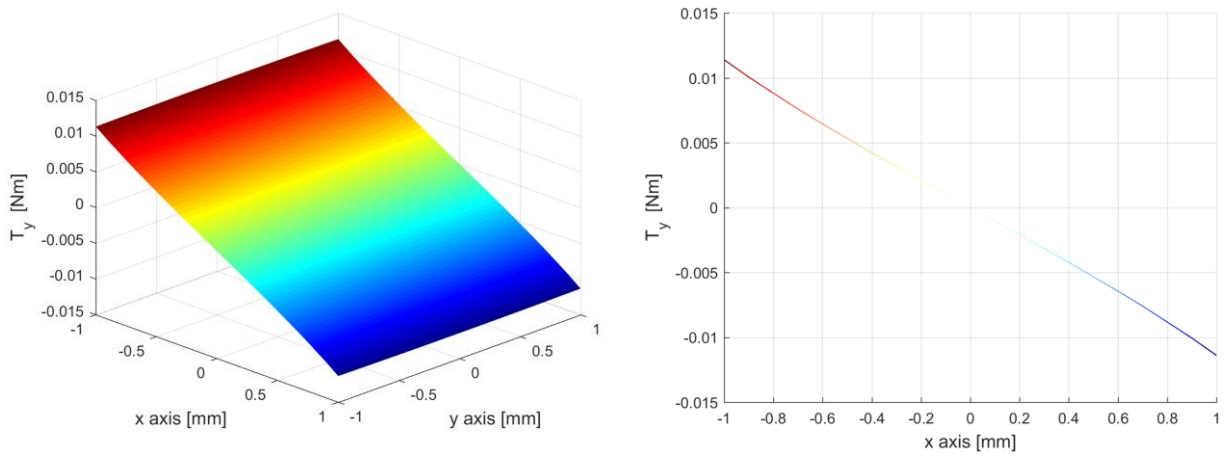

Figure 7.1.2.6 – Torque of upper bearing.

7.1.2.2 Fit a polynomial surface

We proceed to the non-linear regression of the forces using the surface polynomial of equation 3.2 which is represented in the Figure 7.1.2.2.1.
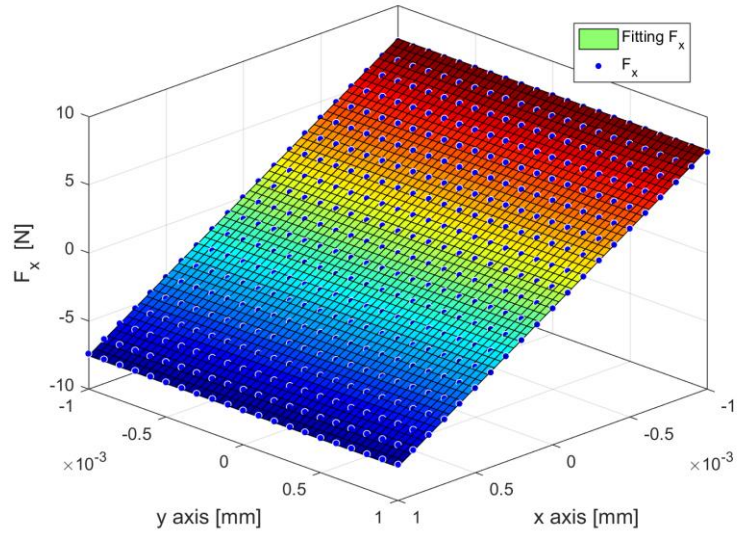
Figure 7.1.2.2.1 – Force along the x axis.

The stiffness coefficients obtained are shown in the Table 7.1.2.2.1.

Table 7.1.2.2.1 – Coefficients for forces along x direction.

Stiffness coefficients			
k_{100}	-7554	k_{211}	0
k_{010}	$4.47 \cdot 10^{-10}$	k_{121}	0
k_{101}	-0.0037	k_{102}	0
k_{011}	-0.00044	k_{031}	$-9.089 \cdot 10^{-20}$
k_{301}	0	k_{012}	$-9.089 \cdot 10^{-20}$

Table 7.1.2.2.2 – Fitting of radial axial force.

Goodness of fit	
SSE	1.116
R-square	0.9999
Adjusted R-square	0.9999
RMSE	0.0509

Also, for the upper bearing considering its radial symmetry and we expect the same stiffness coefficients for a force in any other direction in the plane.
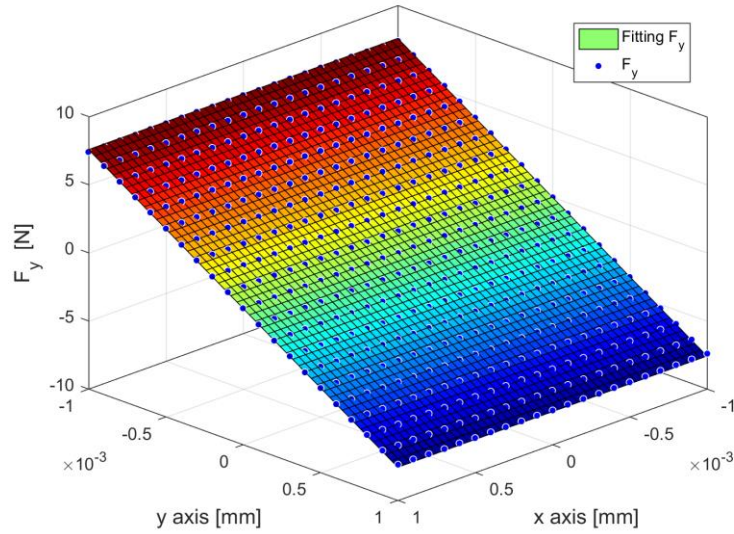
Figure 7.1.2.2.2 – Force along the y axis.

The Table 7.1.2.2.3 shows the values of the stiffness coefficients and comparing them with those of the Table 7.1.2.2.1 we can see that these are similar. In this case the minimum variation is caused by a difference in the values of the magnetic forces and for this reason in the subsequent implementations the coefficients obtained from the F_x fitting will be used.

Table 7.1.2.2.3 – Coefficients for forces along y direction.

Stiffness coefficients			
k_{100}	$8.45 \cdot 10^{-9}$	k_{211}	0
k_{010}	-7577	k_{121}	0
k_{101}	0.00123	k_{102}	$2.037 \cdot 10^{-20}$
k_{011}	-0.00426	k_{031}	0
k_{301}	$2.037 \cdot 10^{-20}$	k_{012}	0

Table 7.1.2.2.4 – Fitting of radial axial force.

Goodness of fit	
SSE	1.359
R-square	0.9999
Adjusted R-square	0.9999
RMSE	0.0559

The polynomial in equation 3.3 was used to fit the magnetic forces in the vertical direction. The stiffness coefficients are shown in the Table 7.1.2.2.5.
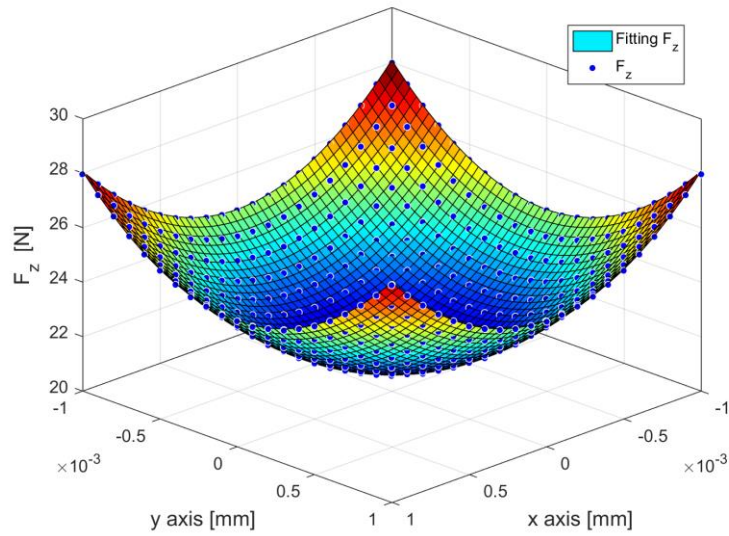
Figure 7.1.2.2.3 – Force along the z axis.

Table 7.1.2.2.5 – Coefficients for force along z direction.

Stiffness coefficients	
k_{000}	21.19
k_{110}	56.43
k_{001}	$3.439 \cdot 10^6$

Table 7.1.2.2.6 – Fitting of vertical force.

Goodness of fit	
SSE	0.3813
R-square	0.9997
Adjusted R-square	0.9997
RMSE	0.02947

Using the polynomial in equation 3.4, it was decided to interpolate the surface represented the pairs with the only coefficients shown in Table 7.1.2.2.7 and Table 7.1.2.2.8 so that there was only one contribution for each variable in the same order of magnitude.
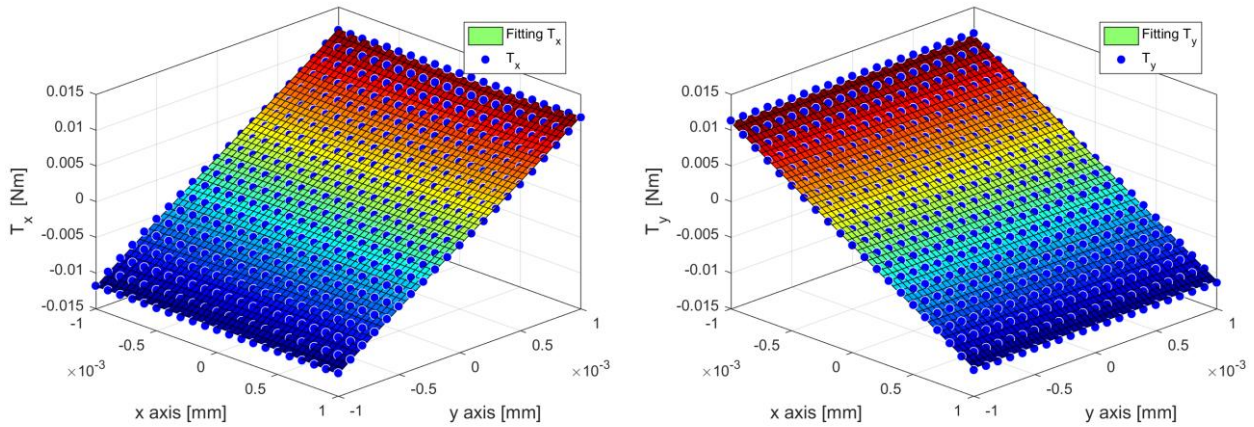
Figure 7.1.2.2.4 – Torques in radial directions.

Table 7.1.2.2.7 – Coefficients for torque along x direction.

Stiffness coefficients			
k_{100}	$8.963 \cdot 10^{-5}$	k_{211}	0
k_{010}	11.08	k_{121}	0
k_{101}	-88.99	k_{102}	$4.221 \cdot 10^{-6}$
k_{011}	$4.079 \cdot 10^{5}$	k_{031}	0
k_{301}	$4.221 \cdot 10^{-6}$	k_{012}	0

Table 7.1.2.2.8 – Coefficients for torque along y direction.

Stiffness coefficients			
k_{100}	-11.05	k_{211}	0
k_{010}	$-3.353 \cdot 10^{-16}$	k_{121}	0
k_{101}	$-1.14 \cdot 10^{-5}$	k_{102}	0
k_{011}	$-4.896 \cdot 10^{-22}$	k_{031}	$1.917 \cdot 10^{-29}$
k_{301}	0	k_{012}	$1.917 \cdot 10^{-29}$

Table 7.1.2.2.9 – Goodness of fit for radial torques.

Goodness of fit	
SSE	$1.0442 \cdot 10^{-5}$
R-square	0.9995
Adjusted R-square	0.9995
RMSE	$1.5565 \cdot 10^{-4}$

7.2 Non-linear Simulink model

The numerical investigation of the rotor trajectories is done through the solution of the nonlinear equations of motion (2.2) with a numerical integration procedure involving a variable step solver (ode45) in Simulink.

Figure 7.2.1 – Model of equation 2.2.

The new model is built starting from the linear one with the addition of a new block representing the non-linear part of the magnetic forces and the forces exchanging at the point of contact, as can be seen in the Figure 7.2.2.

Mass and stiffness matrices are the same as in the linear case, both obtained from the fem analysis with Lupos, while the damping matrix is set to zero due to the introduced viscous damping.

The following model introduces the transformation matrix useful for evaluating the forces and couples of magnetic interactions in the centre of mass.

The same initial conditions of the linear case are imposed (Table 7.2.1) except for the torque resistant to rotation because the resistive forces proportional to the speed at the point of contact are considered both in the radial direction and in the rotation.

Table 7.2.1 – Initial conditions.

Initial condition	Value
$\dot{r}_{z0}$	314 [rad/s]
x_0	$5 \cdot 10^{-4}$ [m]
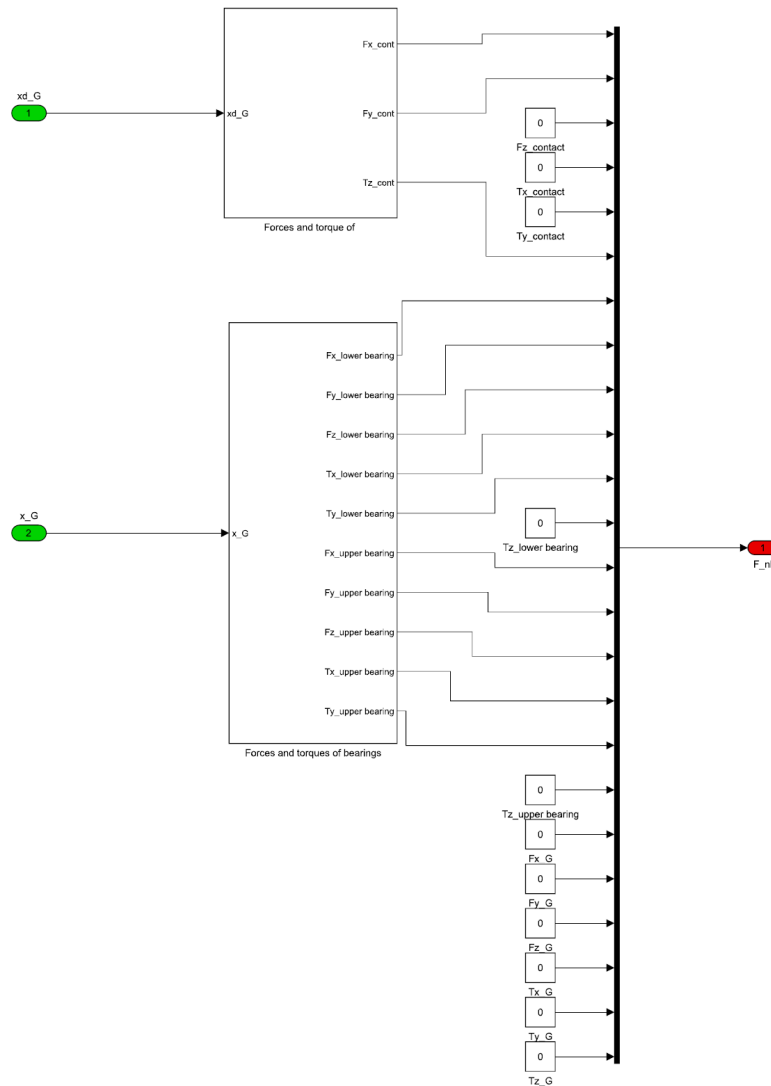
Figure 7.2.2 – Model of non-linear forces and torques.

With the new Simulink model, it is possible to analyse all the various aspects of rotor dynamics as the speed decreases (Figure 7.2.3). As in the non-linear case, the velocity trend is a decreasing exponential.
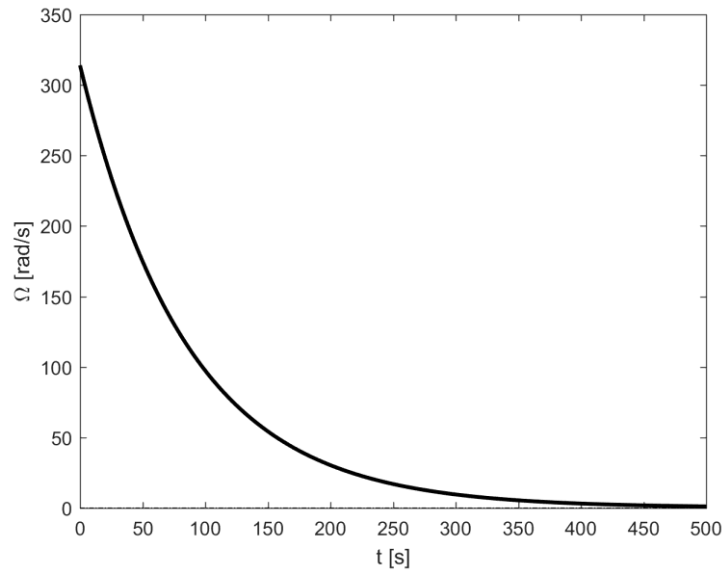
Figure 7.2.3 – Speed trend.

If we analyse the displacement of the centre of mass along the rotation axis (Figure 7.2.4) we will notice how the rotor will tend to move downwards due to a static offset for the weight force.
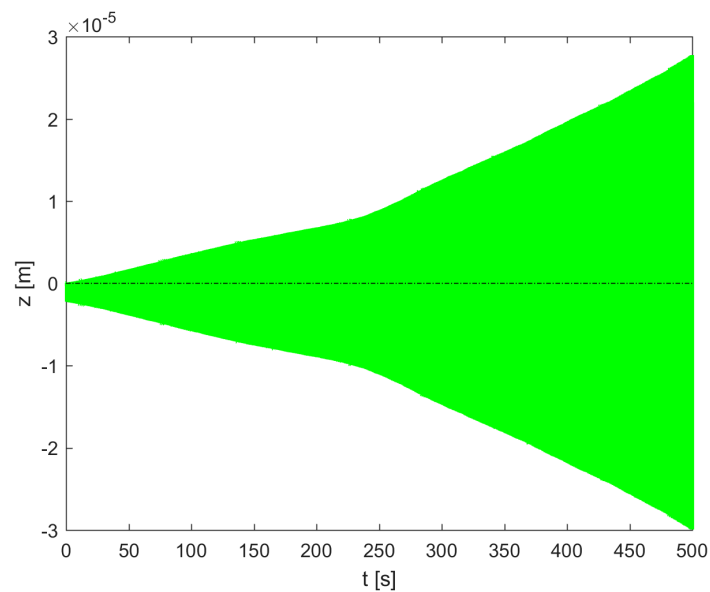
Figure 7.2.4 – Displacement of the centre of mass.

The Figure 7.2.5 and Figure 7.2.6 show the rotor displacements in the two radial directions as time and rotation speed change. The analysis is done in three different time periods to then represent the different type of trajectory in the XY plane.
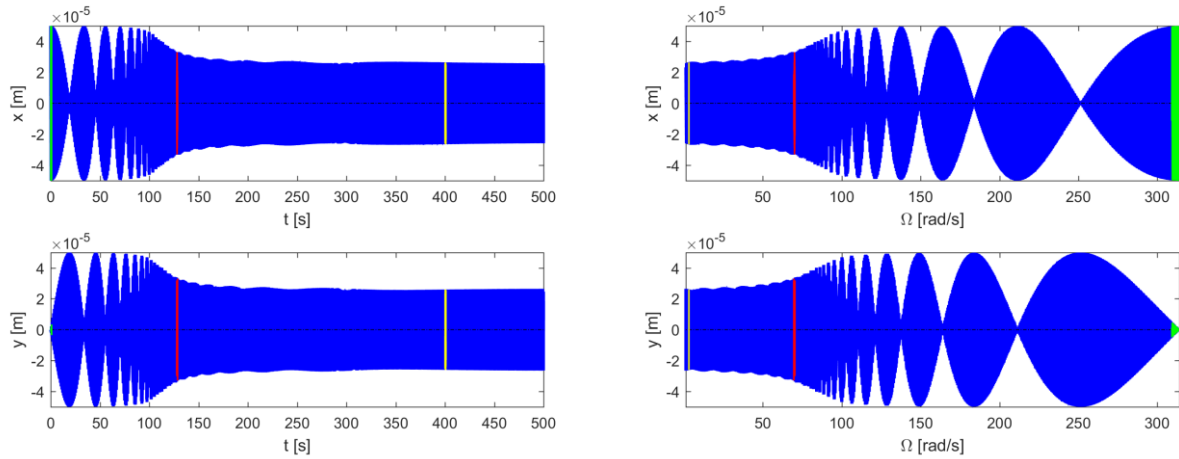
Figure 7.2.5 – Shifts according to time and speed.

The trajectory at the beginning of the simulation is shown in green. The rotor is at high speed and due to the initial displacement, the linear alignment moves from the stability point. Over time, the speed decreases and the rotor begin to describe the typical trajectory of the flower petals as can be seen in the magenta trajectory. In the last part of the simulation, the rotor continues to move around the equilibrium position with increasingly circular trajectories.
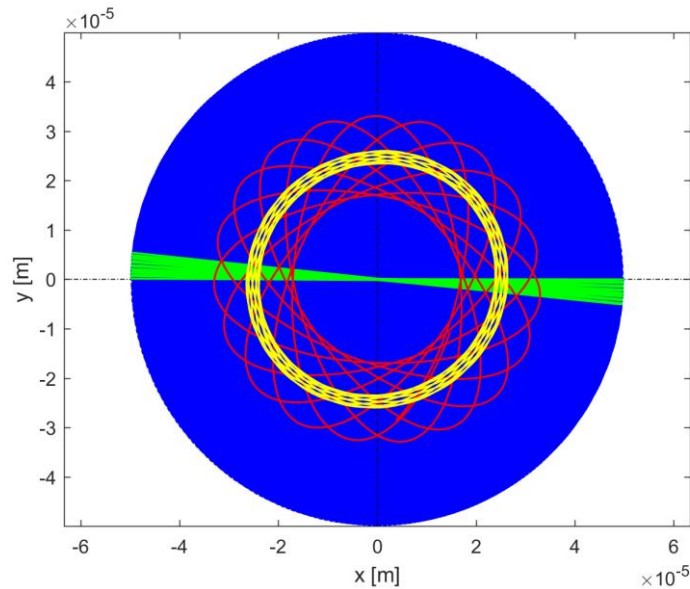
Figure 7.2.6 – Centre of mass trajectory.

Similarly, to what was done for the displacements, the small rotations along the two main directions were evaluated in the Figure 7.2.7. Analysing the behaviour of the system in three different moments and therefore at three different speeds, it is in the initial phase, and therefore at high speeds, the rotations are very small.
This behaviour is reversed with the progressive reduction of rotation speed.
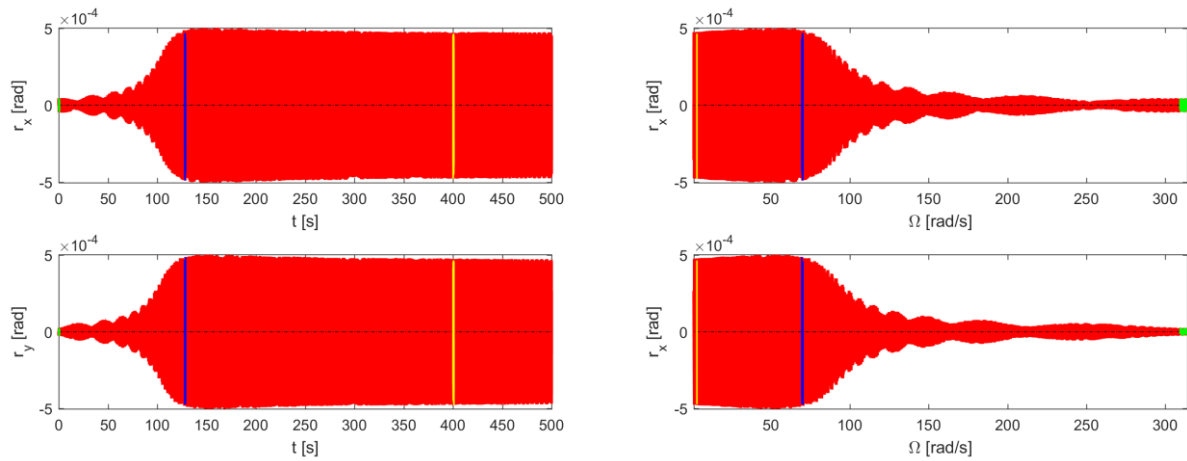
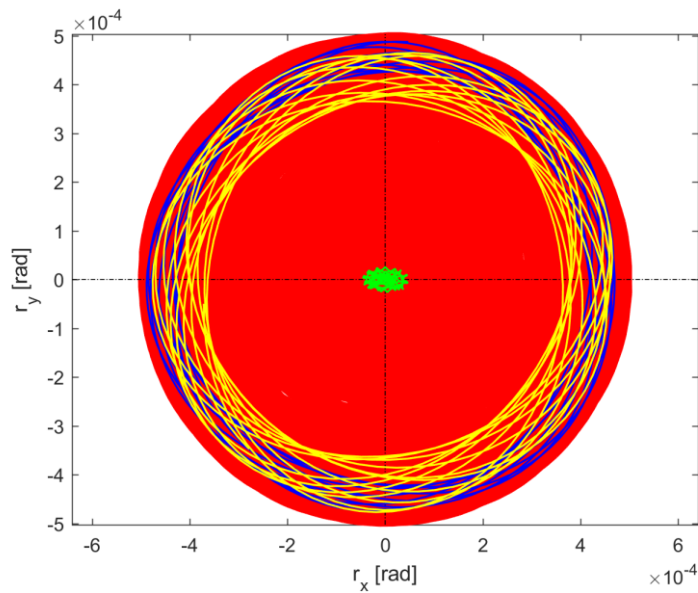Figure 7.2.7– Rotations according to time and speed.

Figure 7.2.8 – Rotation rx-ry.

The Campbell diagram can be plotted only in the case of linear systems, because only in this case does the very concept of natural frequencies apply. However, in the case of nonlinear systems, the Campbell diagram of the linearized system may yield important information on the behaviour of the system.

8. Non-linear model with three different initial displacements

The numerical model used for dynamic analysis is influenced by the initial conditions chosen. Given the same speed set by the electric motor, it was decided to analyse the behaviour of the rotor with three different initial shifts.
The initial condition on the displacement does not influence the speed of rotation, in fact in Figure 8.1 it can be seen how we have the same decreasing trend in the three cases.
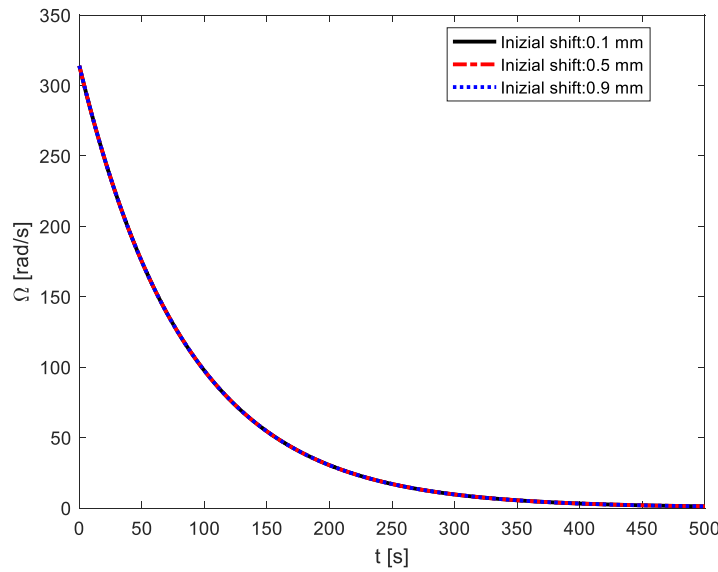
Figure 8.1 – Speed trend.

The differences of the three cases are visible in the Figure 8.2 and Figure 8.3 that represent translations and rotations along the main axes. When the rotor is turned over at high speeds, the displacements over time are along the same dimension but with different amplitudes. With the progressive reduction of the speed, the rotor will have displacements no longer along the axis considered at the same time instant.
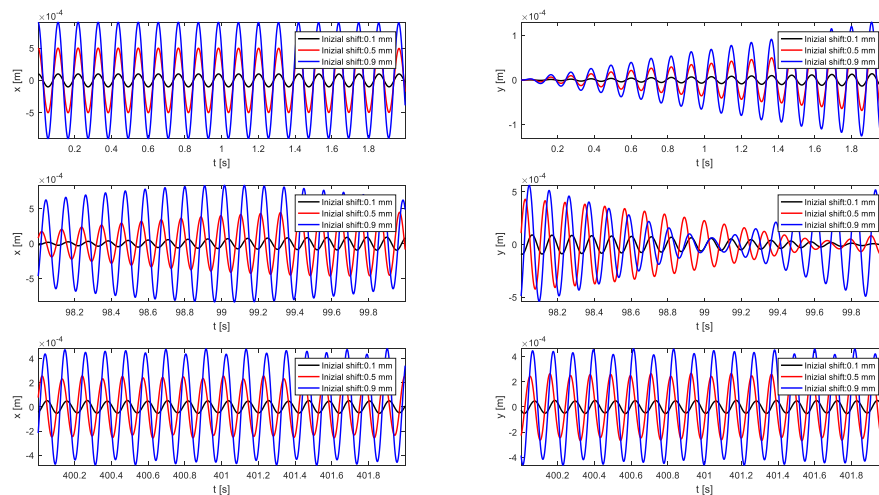
Figure 8.2 – Comparison of movements.

The same is true for rotations. At high speeds, only an increasing value of the rotation is the initial displacement increases. By reducing the speed, the rotor will have a rotation along the axis considered more and more with a time delay.
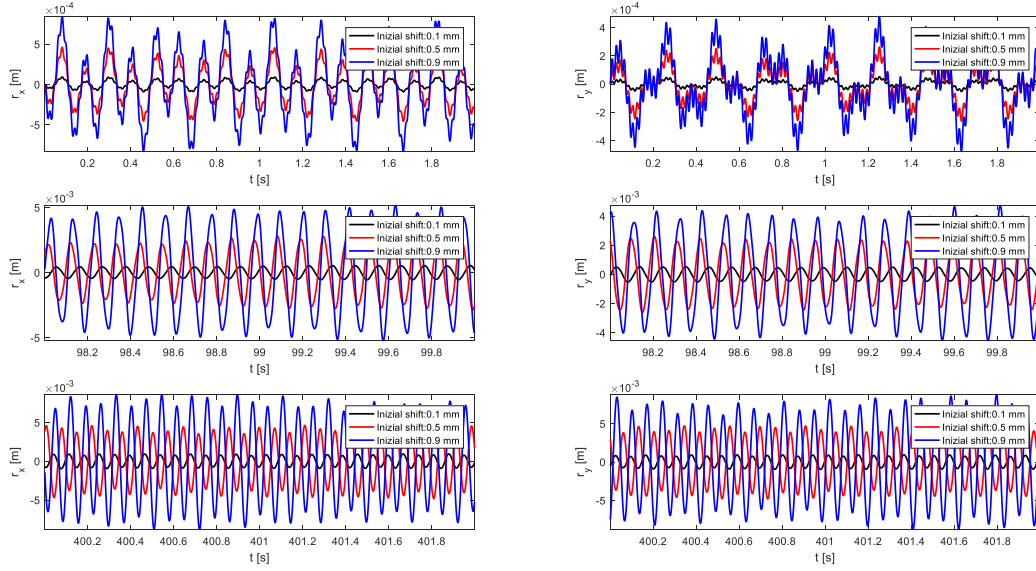

Figure 8.3 – Comparison of rotations.

9. Comparison between linear and non-linear model

To verify the correctness of a linear approach for the dynamic analysis of a rotor with magnetic bearings, we compare the results obtained from the two numerical models having the same initial conditions:

- initial speed rotation: Ω=314 rad/s;
- initial displacement along the x axis: $x_0 = 5 \cdot 10^{-4}$ m;
- null damping matrix;
- contact point resistance forces proportional to speed. The coefficients for damping are:
  - $c_x = 3 \cdot 10^{-4} \, N \cdot s / m$
  - $c_y = 3 \cdot 10^{-4} \, N \cdot s / m$
  - $c_{rz} = 3 \cdot 10^{-4} \, N \cdot s / rad$.

As we can see in Figure 9.1, the non-linear contribution of the magnetic forces does not influence the descending trend of the rotor's speed of rotation.
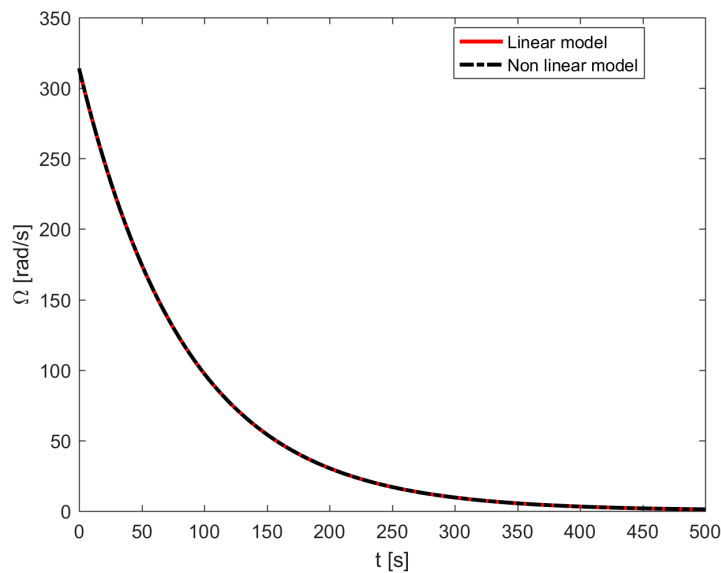
Figure 9.1 – Speed trends.

The different between the two model is visible with the displacements. Figure 9.2 shows the rotor displacements in the radial direction for three different moments of the simulation. In the initial phase, when the rotor is at high speed, the displacements for the two cases under consideration are the same. After 100 seconds, we can see how the displacements between linear and nonlinear case are similar with a slight phase shift.
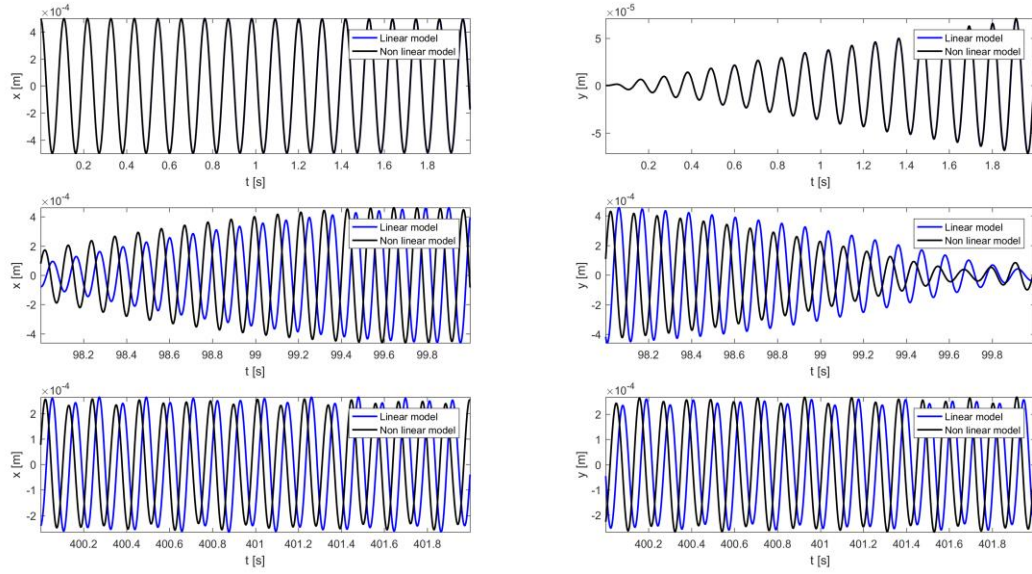
Figure 9.2 – Displacements in the time.

Analysing the rotations along the two main directions, it can be seen how the trend is similar in the first part of simulation (Figure 9.3). Subsequently, the trend of the rotations obtained between the two models presents a small phase shift until reaching a trend in opposition to do in the last simulative part.
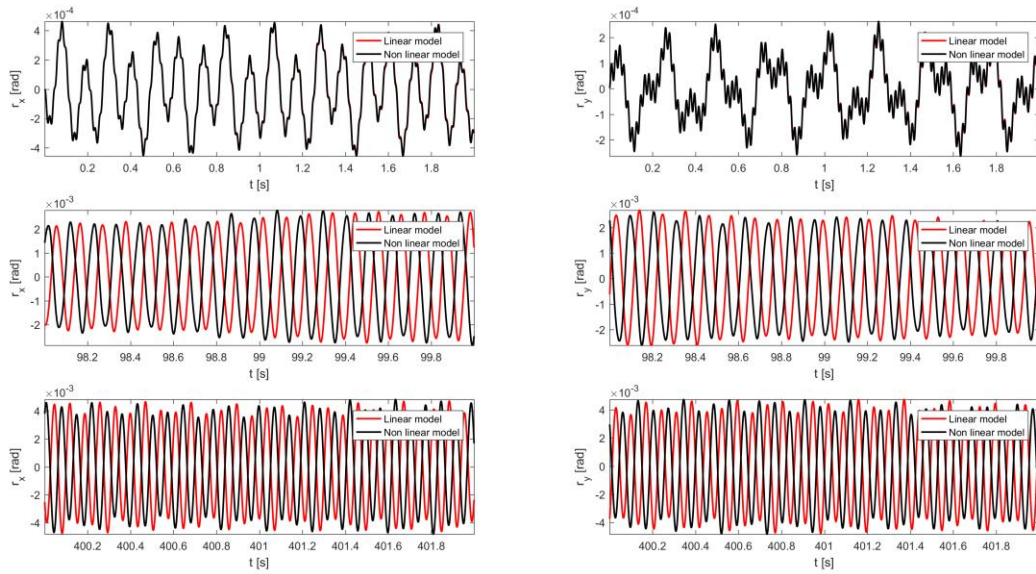

Figure 9.3 – Rotations according to time.

In the Figure 9.4 we make a comparison between the linear and nonlinear component of the magnetic forces and torques. Although the linearized forces are larger than the non-linear contribution, these must be considered for the dynamic analysis of a real rotor because they are only two order of magnitude smaller.
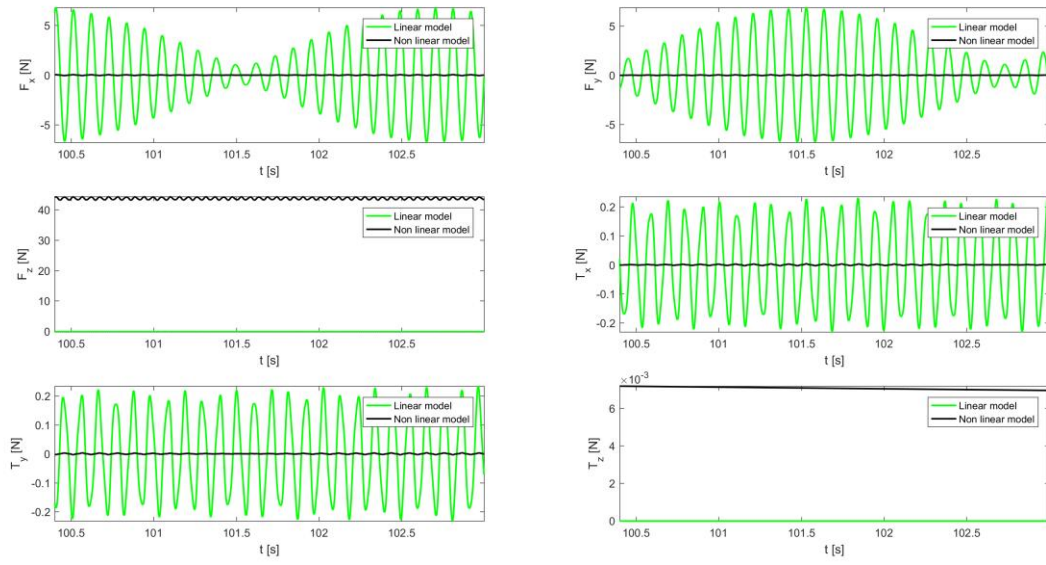
Figure 9.4 – Confrontation between forces.

10. Unbalance model

In real life, the centre of mass cannot be exactly coincident with the centre of the cross section of the shaft. The distance between the two points may be small, but the presence of the eccentricity (ε) causes a static unbalance that can strongly affect the behaviour of the system.
The problem of an unbalanced system is addressed by solving the dynamic equation 10.1.

$$\mathbf{M\ddot{x}} + \left(\mathbf{C} + \Omega\mathbf{G}\right)\mathbf{\dot{x}} + \mathbf{Kx} + \mathbf{F_{nl}} = \mathbf{F} \tag{10.1}$$

The mass matrix obtained by the fem analysis in LUPOS is analogous to that obtained for a balanced rotor. The most important terms are those on the main diagonal with the increase in the overall mass. Due to an unbalance due to the addition of mass in one point of the rotor, the moments of inertia have changed. The polar moment of inertia is decreased, while transversal the moments of inertia are no longer equal.
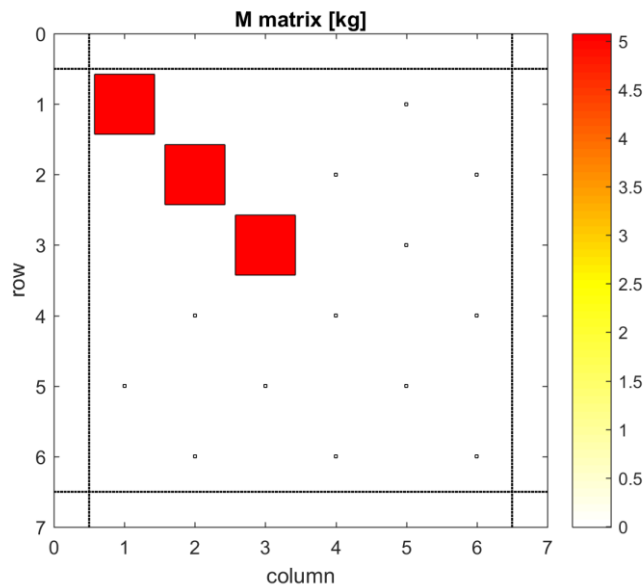

Figure 10.1

It is important to note that the off-diagonal terms have increased a lot.
The modal analysis of the system was performed by using LUPOS obtaining ten complex conjugated underdamped modes and two overdamped modes. The modes are coupled together at five different natural frequencies.
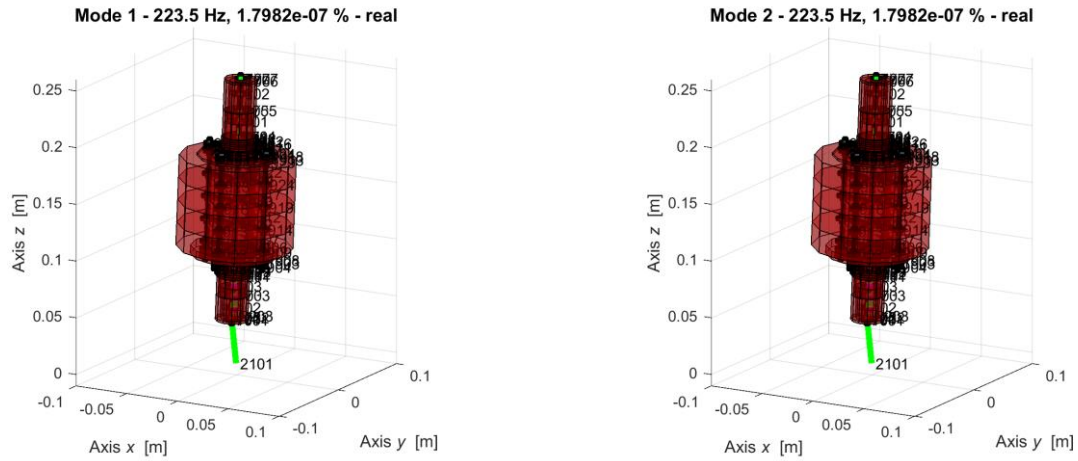
Figure 10.2 – Shaking modes.

The system has four cylindrical and four conical modes. With the unbalanced system the cylindrical modes do not all manifest themselves at the same natural frequency, but at two different frequencies.

For a given frequency there are two modes that identify a cylindrical vibratory movement along a direction, while we can observe the motion along the direction orthogonal to the first with the new two different modes.
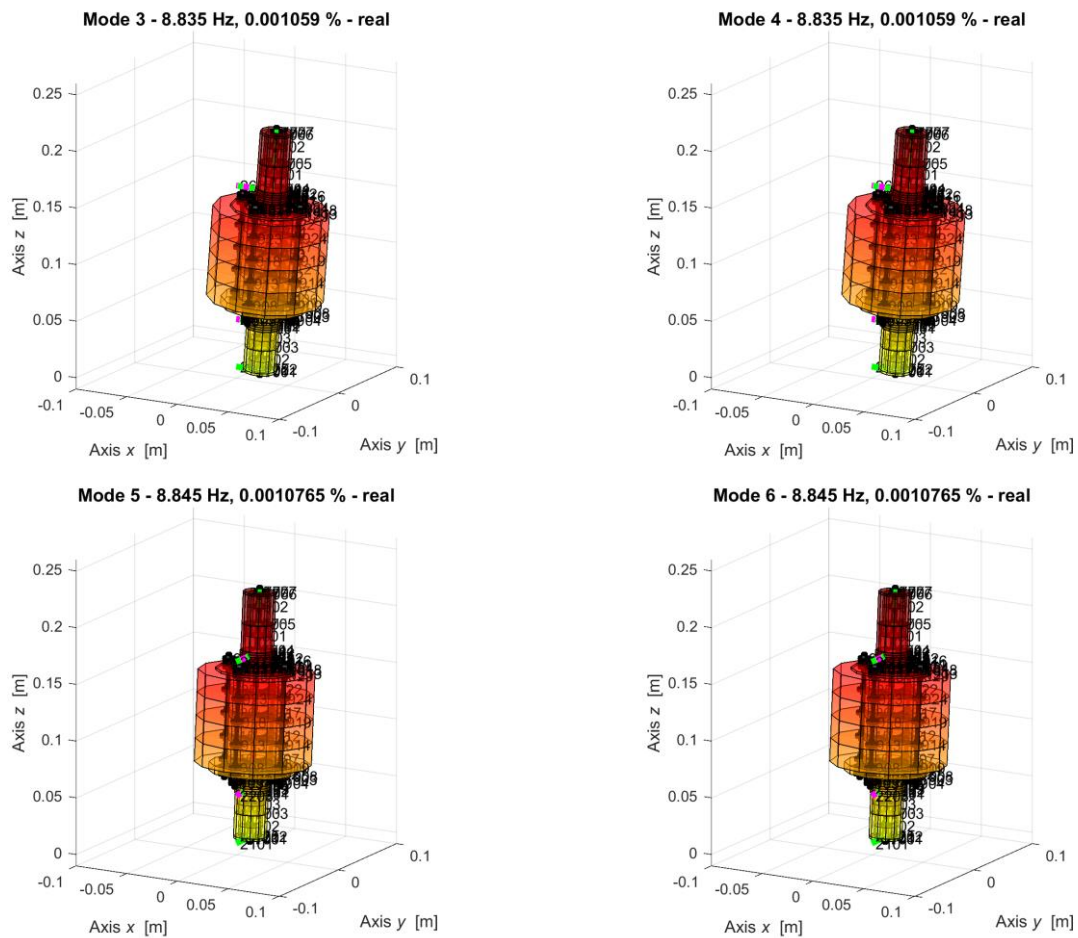

Figure 10.3 – Bounce modes.

A similar discourse can be made regarding conical modes. As can be seen in the figure, the conical whirls in the two different main directions occur at two different natural frequencies.
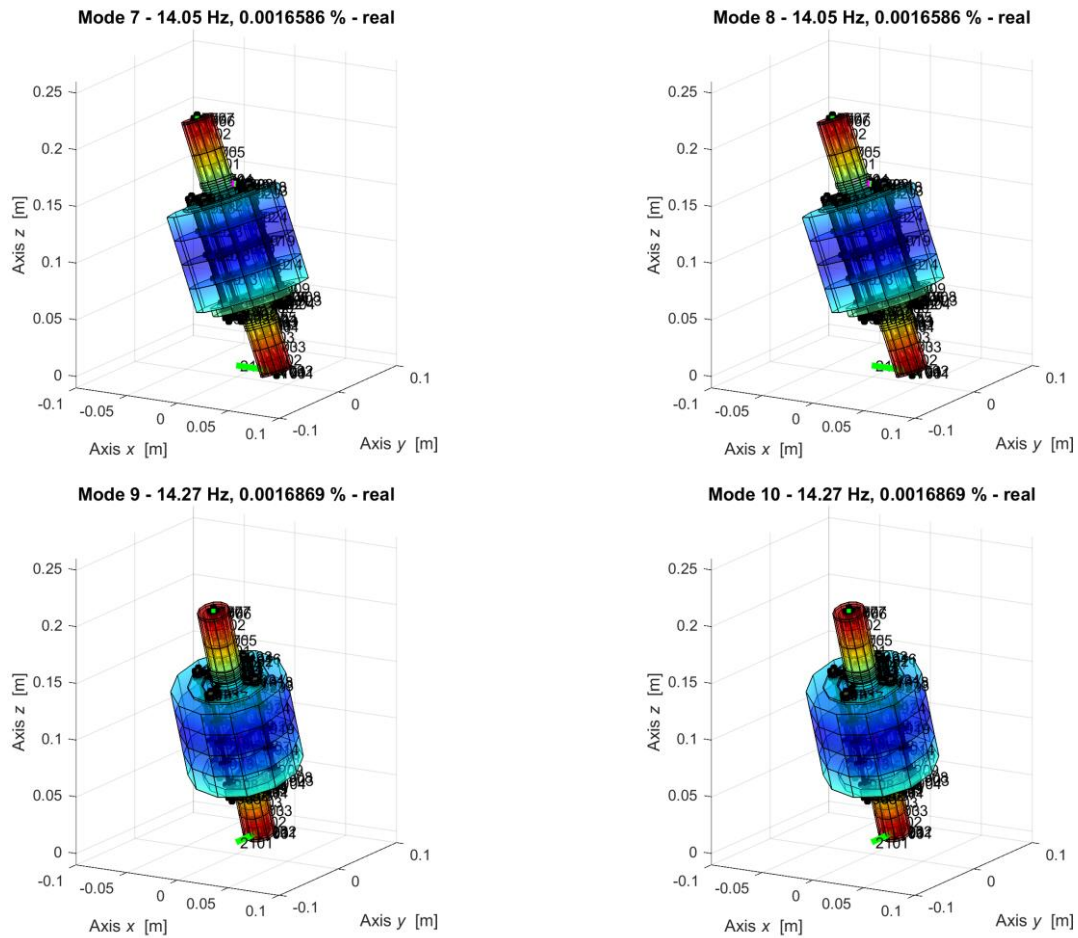

Figure 10.4 – Conical modes.

The two overdamped modes are those that have a negative real part and a very small imaginary part. These two modes can be identified in the two zero-frequency rotations.
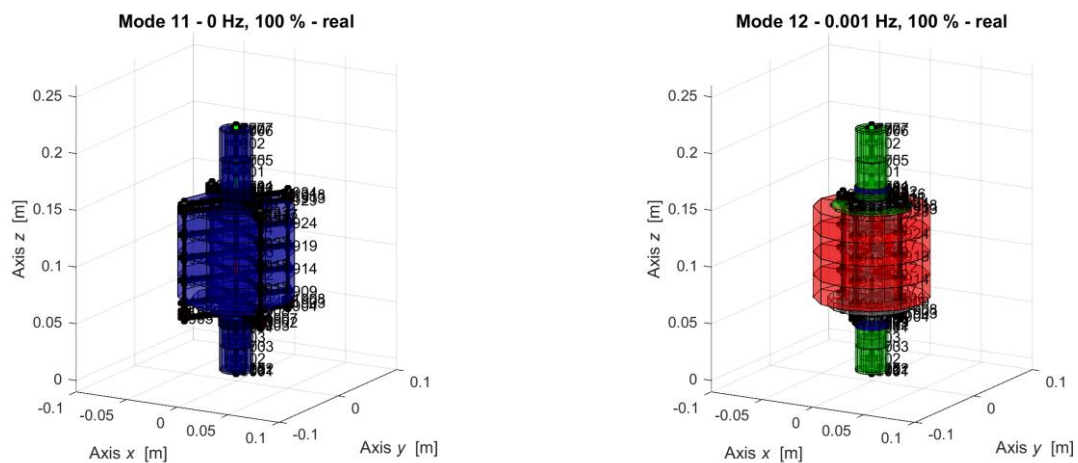

Figure 10.5 – Rotation modes.

The Table 10.1 shows the critical speeds and frequencies for each mode.

Table 10.1 – Critical speeds.

Modes	Ω [rad/s]	f_n [Hz]
1	1404.3	223.5
2	1404.3	223.5
3	55.512	8.835
4	55.512	8.835
5	55.575	8.845
6	55.575	8.845
7	88.28	14.05
8	88.25	14.05
9	89.66	14.27
10	89.66	14.27
11	0	0
12	0	0

10.1 Model M, C, G, K

The numerical investigation of the rotor trajectories is done through the solution of the nonlinear equations of motion (2.2) with a numerical integration procedure involving a variable step solver (ode45) in Simulink.
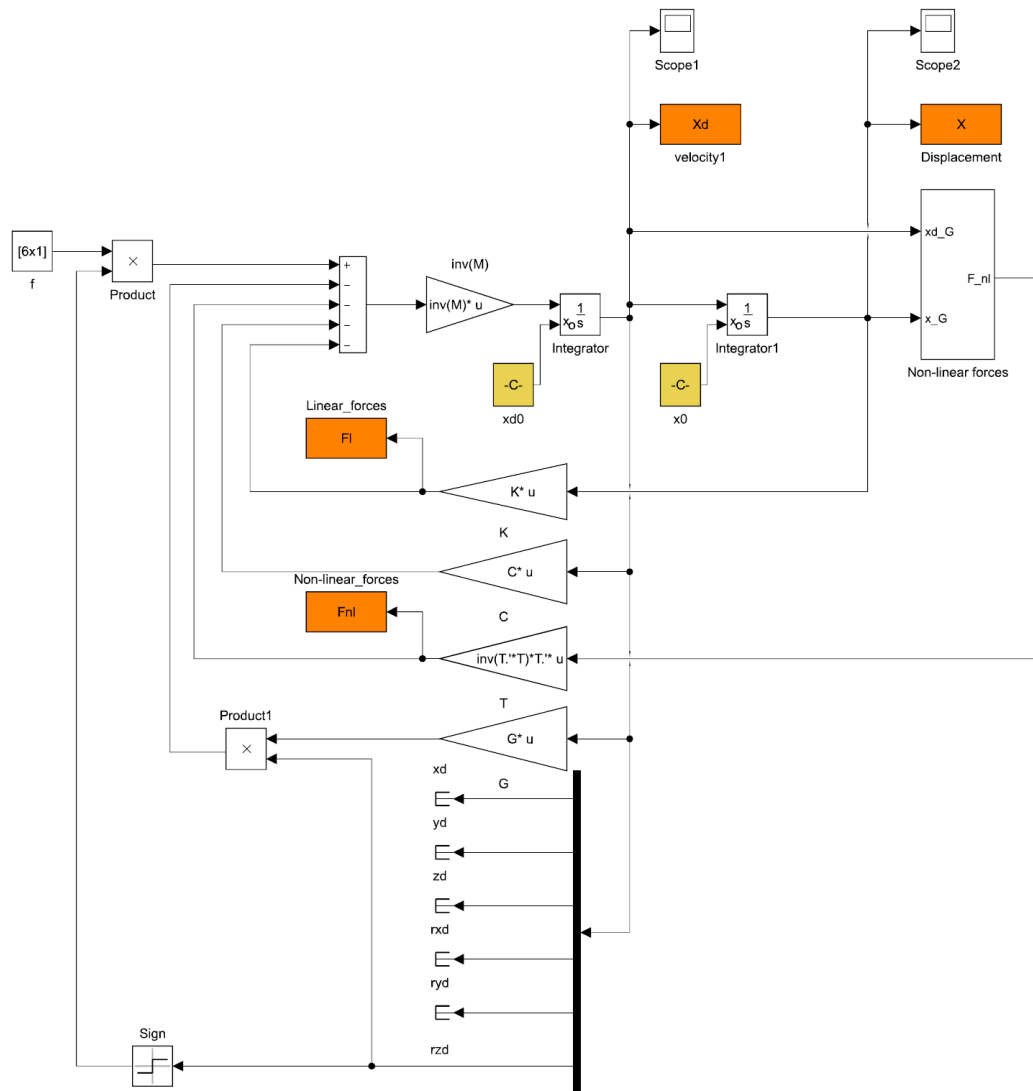
Figure 10.1.1 – Model of equation 2.2.

The new model is built starting from the linear one with the addition of a new block representing the non-linear part of the magnetic forces and the forces exchanging at the point of contact, as can be seen in the Figure 10.1.1.

Mass and stiffness matrices are the same as in the linear case, both obtained from the fem analysis with Lupos, while the damping matrix is set to zero due to the introduced viscous damping.

The following model introduces the transformation matrix useful for evaluating the forces and couples of magnetic interactions in the centre of mass.

The same initial conditions of the linear case are imposed (Table 10.1.2) except for the torque resistant to rotation because the resistive forces proportional to the speed at the point of contact are considered both in the radial direction and in the rotation.

Table 10.1.1 – Initial conditions.

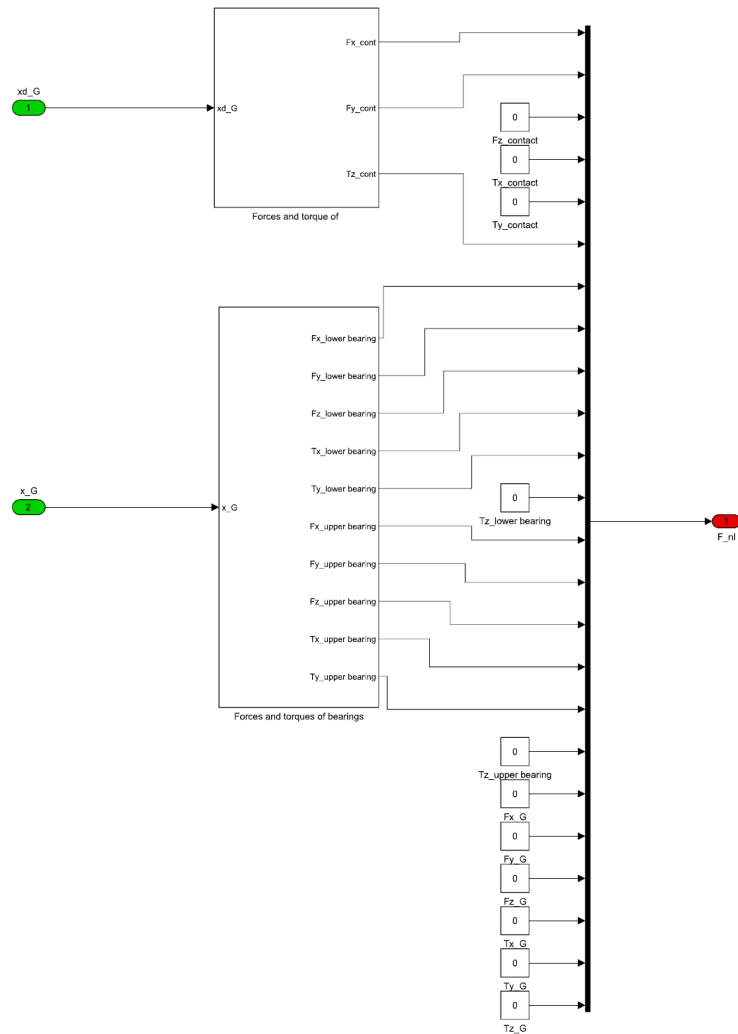| Initial condition	Value
$\dot{r}_{z0}$	314 [rad/s]
x_0	$5 \cdot 10^{-4}$ [m]

Figure 10.1.2 – Model of non-linear forces and torques.

With the new Simulink model, it is possible to analyse all the various aspects of rotor dynamics as the speed decreases (Figure 10.1.3). As in the balance rotor, the velocity trend is a decreasing exponential.
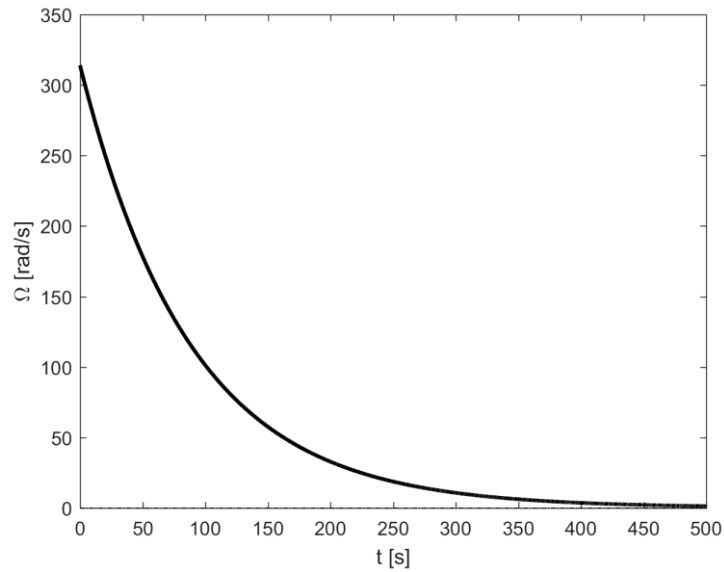
Figure 10.1.3 – Speed trend.

If we analyse the displacement of the centre of mass along the rotation axis (Figure 10.1.4) we will notice how the rotor will tend to move downwards due to a static offset for the weight force.
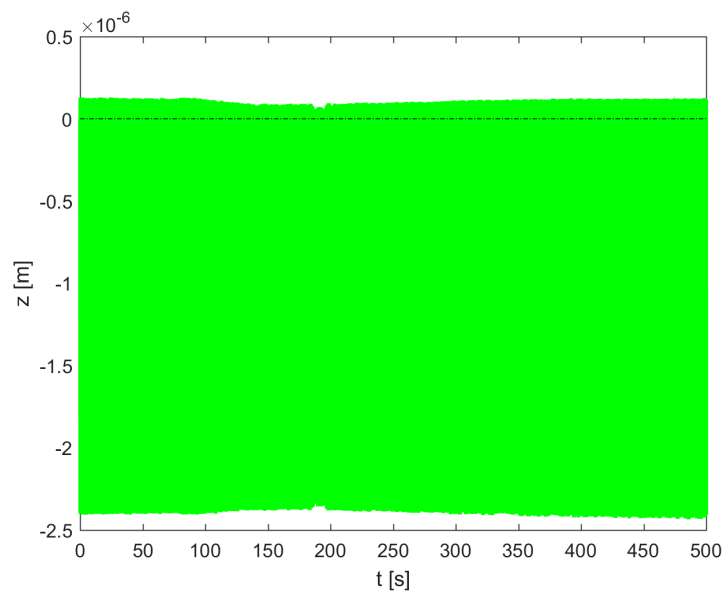
Figure 10.1.4 – Displacement of the centre of mass.

The Figure 10.1.5 and Figure 10.1.6 show the rotor displacements in the two radial directions as time and rotation speed change. The analysis is done in three different time periods to then represent the different type of trajectory in the XY plane.
It is interesting to note that at low speeds, the rotor reduces the displacement in the direction in which the initial imbalance has been given to increase it in the orthogonal direction.
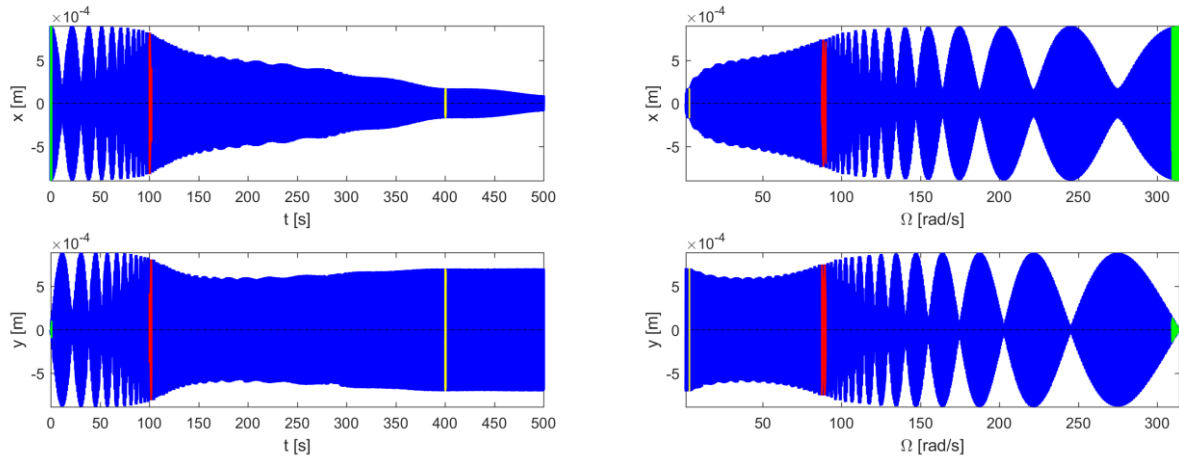
Figure 10.1.5– Shifts according to time and speed.

The trajectory at the beginning of the simulation is shown in green. The rotor is at high speed and due to the initial displacement, the linear alignment moves from the stability point. Over time, the speed decreases and the rotor begin to describe the typical trajectory of the flower petals as can be seen in the magenta trajectory. At low speeds the rotor continues to move around the equilibrium point with elliptical trajectories.
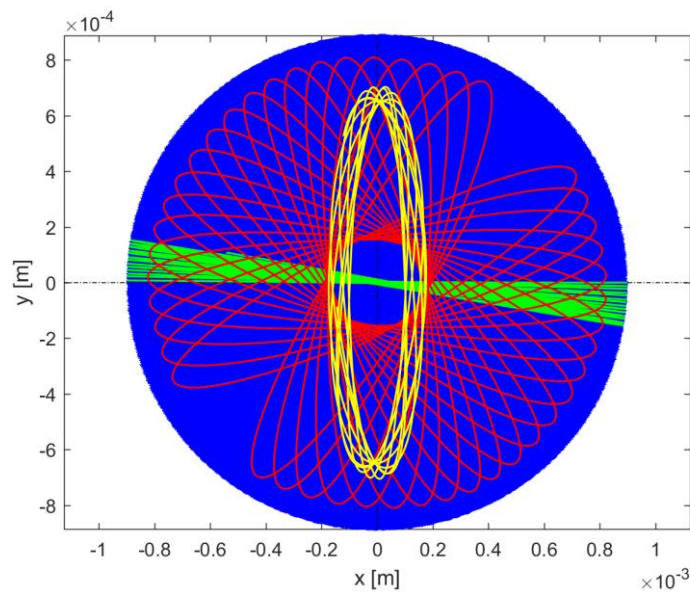

Figure 10.1.6 – Centre of mass trajectory.

Similarly, to what was done for the displacements, the small rotations along the two main directions were evaluated in the Figure 10.1.7. Analysing the rotations during the simulation time, it can be seen how, for the rotation along x, there is immediately an angle increase and then have a reduction in the final part of the simulation, when the speed is low. Rotations along y have opposite behaviour in the simulation end.
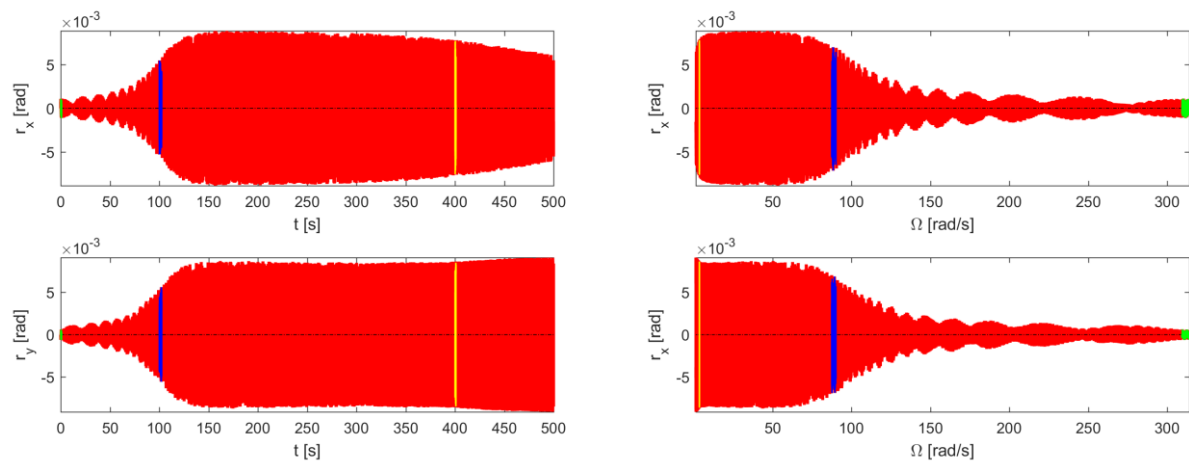
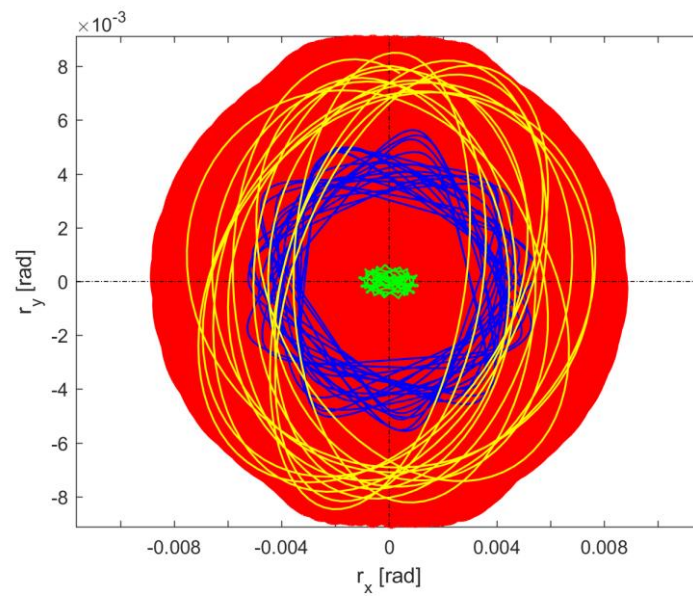Figure 10.1.7 – Rotations according to time and speed.

Figure 10.1.8 – Rotation rx-ry.

11. Time – frequency analysis

Very often the analysis of a signal over time is not enough to show some characteristics of the dynamic system, for this reason it is flanked by the analysis in the frequency field.

The equations of rotor motion can be written in a more compact form by defining a set of complex coordinates.

$$\mathbf{M}\ddot{\mathbf{x}}_C + (\mathbf{C} + \Omega\mathbf{G})\dot{\mathbf{x}}_C + \mathbf{K}\mathbf{x}_C = \mathbf{F} \tag{11.1}$$

$\mathbf{x}_C, \dot{\mathbf{x}}_C, \ddot{\mathbf{x}}_C$ are respectively the generalized displacements, the velocities and accelerations of the only active degrees of freedom and have the following form:

$$\mathbf{x}_C = \begin{Bmatrix} x + iy \\ z \\ r_y - ir_x \\ r_z \end{Bmatrix} \tag{11.2}$$

From the results obtained in real field we can plot the displacements and rotations in the complex field (Figure 11.1).
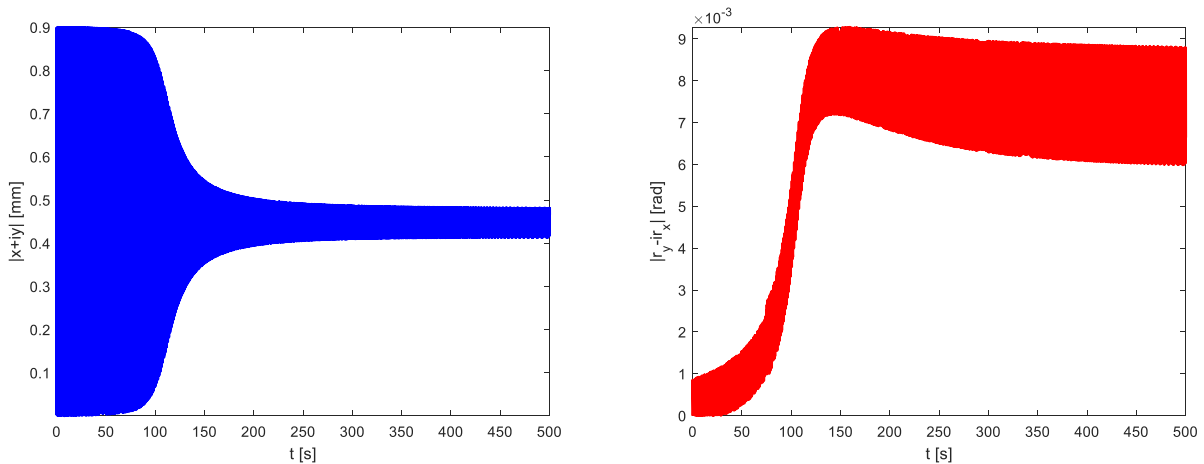

Figure 11.1 – Displacements and rotations in complex coordinates.

The displacements along the vertical axis and the small rotations around it will be the same as the real field. Complex coordinate analysis is useful for time frequency analysis of the system.

Through the decomposition into "Fourier transform" it is possible to approximate any function over time by adding sum of harmonic functions. If the functions are not periodic, they should be considered as functions having a period tending to infinity.

In this way it is possible to highlight how many and which harmonics a signal contains and which oscillation amplitudes these harmonics possess.
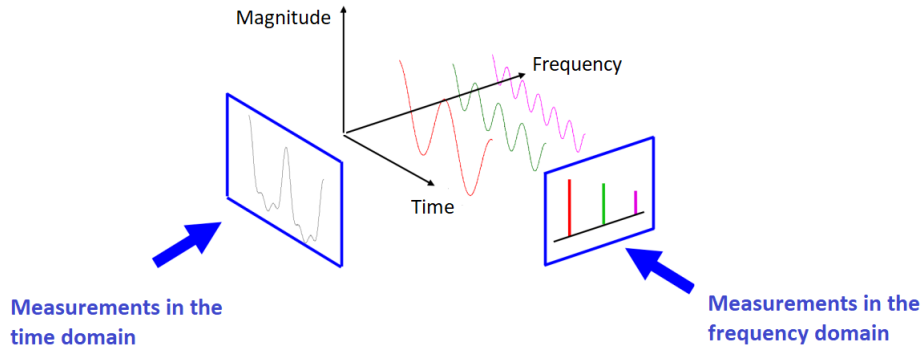
Figure 11.2 – Same measure but different point of view.

With this type of analysis, we can know which are the main harmonics of a signal that excites a system.

As mentioned, the signals we analyze are not continuous functions in the time domain but discrete; in other words, instead of a function $f = (t)$, we have a finite set of its samples $f_k = (N \cdot \Delta t)$ where:

- Δt is delta time sample,
- N is the number of samples.

The number of samples is given by the ratio between the total time of the signal (T) and the delta time.

For frequency analysis, other parameters depending on the first are necessary:

- $f_s = \dfrac{1}{\Delta t}$ frequency sample,

- $\Delta f = \dfrac{f_s}{N} = \dfrac{1}{N \cdot \Delta t} = \dfrac{1}{T}$ frequency resolution,

- $f_b = \dfrac{f_s}{2}$ frequency bandwidth (Nyquist theorem).

The Fourier analysis is formally applied to signals of infinitely large duration and therefore also the duration of the samples representing the signal in discrete form must be theoretically of infinite length.

This hypothesis is obviously not feasible since the sequence of the samples will necessarily have a beginning and an end, and therefore the number of available samples will be a finite number.

This leads me to an error called leakage.

For the frequency analysis of the magnetic rotor, we have chosen as the sampling time the average value between two successive time instants. So, we got the following parameters in Table 11.1.

Table 11.1 – Initial parameters for time-frequency analysis.

Parameters	Value
Δt [s]	10^{-3}
N	500001
f_s [Hz]	1000
Δf [Hz]	0.002

To limit the effect of leakage, we can proceed to the windowing operation. This operation consists in applying a window to the temporal history to be analyzed, which aims to impose a periodicity on the signal, canceling the extremes and keeping the signal as unchanged as possible in its central part.

When we have sufficiently long acquisitions, another way to analyze its frequency content is to consider the signal as consisting of a succession of time windows of shorter duration, frames, of which the analysis is performed, and the results are mediated. In other words, we consider a temporal history consisting of N samples of a signal, in which there are k samples (chosen arbitrarily) which constitute the temporal sub-story. Everyone will be windowed to reduce the leakage error.
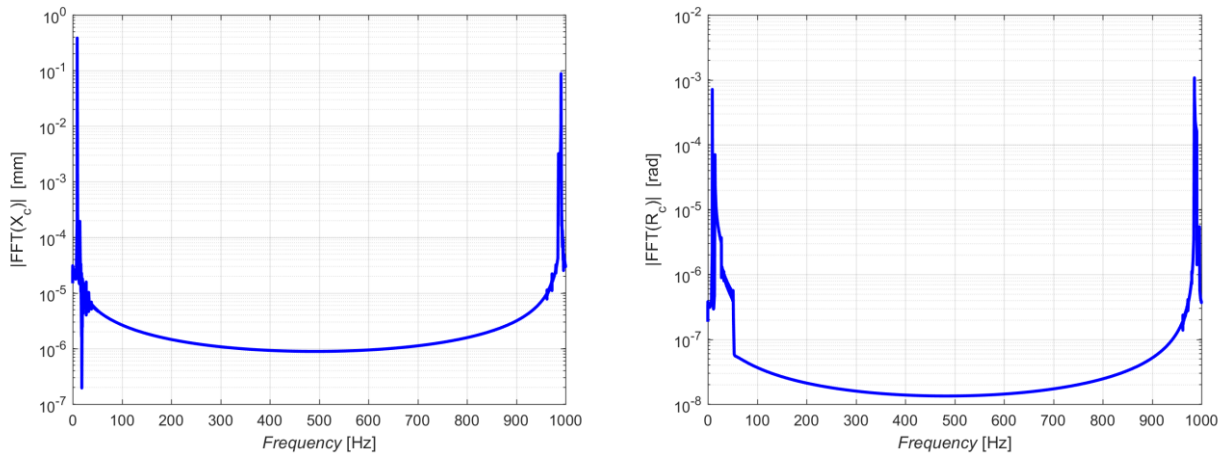
Figure 11.3 – Measurement in the frequency domain.

As you can see in Figure 11.3, at the frequency of 9.114 Hz and at the frequency of 14.39 Hz there are the two natural frequencies of the magnetic rotor.

Through spectrograms it is possible to understand how the frequency content of a signal evolves over time. For this type of analysis, it is of primary importance to set the parameters optimally, that is to look for the best compromise between the frequency resolution Δf, the resolution in the time Δt, the calculation times and the waste of sampled data.

Increasing the size of the time windows (large Δt) the frequency resolution improves (small Δf) as it allows to identify the frequency more precisely. However, this has some disadvantages: at the beginning and at the end of the signal it is not possible to associate a frequency content.

Furthermore, it can erroneously associate to an instant of time some frequencies that may have manifested themselves decidedly before or after, that is it samples harmonics that are not there.

As can be seen in the Figure 11.4, the frequency information appears in a range between $t_{i,FFT}$ and $t_{f,FFT}$ This depends on the sampling frequency and the number of frames for each time point.
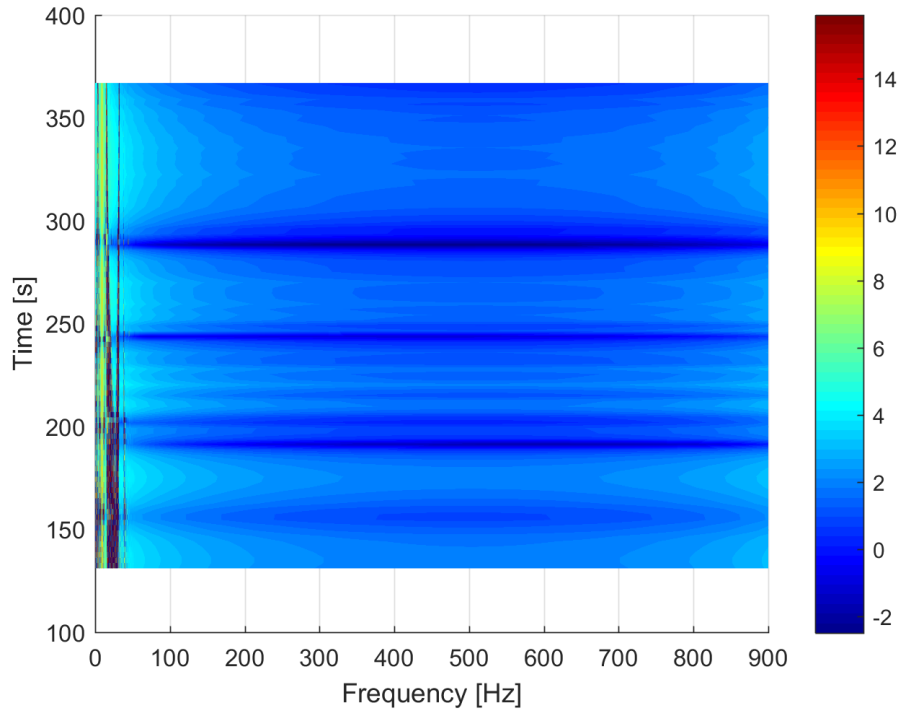
Figure 11.4 – Time frequency analysis with $k = 2^{18}$ and 99% overlap.

Assumed $k = 2^{18}$ and with $f_s = 1000\,\mathrm{Hz}$, we get the time interval of the content in frequency.

$$t_{i,FFT} = t_i + \frac{1}{2}\frac{k}{f_s} = 131s \tag{11.3}$$

$$t_{f,FFT} = t_f - \frac{1}{2}\frac{k}{f_s} = 368.9s \tag{11.4}$$

The Figure 11.5 shows the two frequencies to which the system representing two of the modes found through the modal analysis.

The time frame size is $\Delta t = k \cdot \frac{1}{f_s} = 262.14s$. The frequency resolution is $\Delta f = 0.0038Hz$ while the

temporal one is $\Delta T = (1 - overlap) \cdot k \cdot \frac{1}{f_s} = 2.621s$.
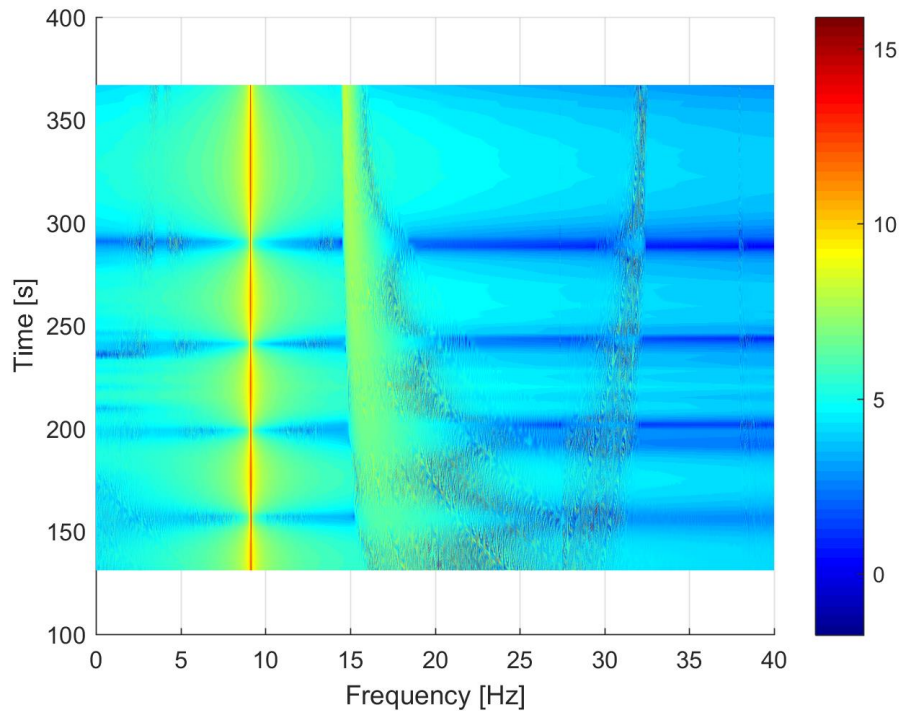
Figure 11.5 – Time frequency analysis with $k = 2^{18}$ and 99% overlap between 0 Hz and 40 Hz.

Decreasing the size of the frame to $k = 2^{15}$ samples, you get $\Delta f = 0.0305 Hz$, $\Delta t = 32.768 s$ and $\Delta T = 0.327 s$. In this way it is possible to better highlight the constant frequency part as can be seen in the Figure 11.6. All this however goes to the detriment of the frequency resolution which results quadrupled.
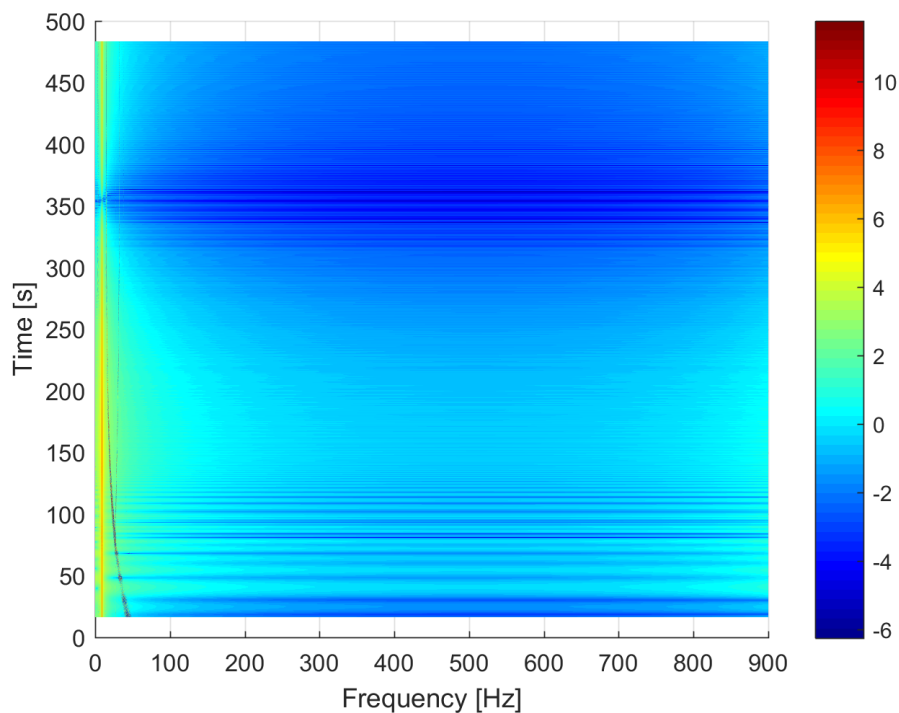
Figure 11.6 – Time frequency analysis with $k = 2^{15}$ and 99% overlap.
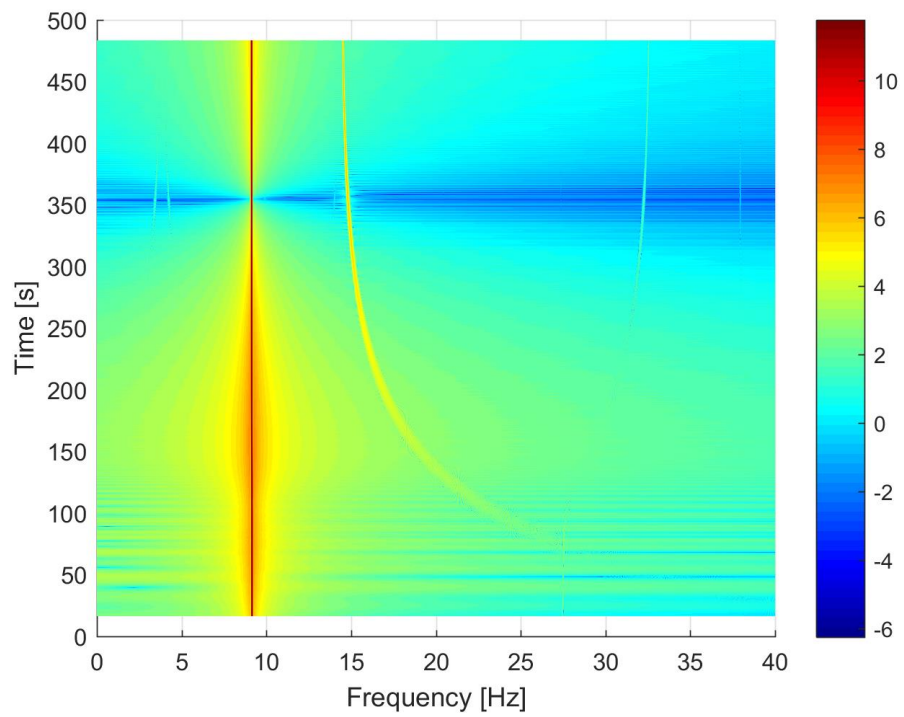
Figure 11.7– Time frequency analysis with $k = 2^{15}$ and 99% overlap between 0 Hz and 40 Hz.

Conclusions

The thesis project is based on the creation of a model of a vertical rotor supported by magnetic bearings and its numerical analysis of the linear and non-linear behaviour of magnetic forces.

In a first part the configuration was studied, paying attention to the linear forces exchanged between the rotor and stator magnets in order to minimize the contribution of the weight force and therefore of the friction.

In the second part the magnetic rotor in LUPOS was modelled which allowed us to carry out a modal analysis and therefore identify the natural frequencies.

Using a Simulink model, a dynamic rotor model was implemented which allowed us to plot the typical petal trajectory of a rotor. This analysis was further enriched by also considering the non-linear contribution of the magnetic rings perhaps exchanged between rotor and stator.

The choice of which type of approach to use for the analysis depends very much on the type of study you will want to perform.

With the same initial conditions, if we want to study the decay of speed, we will not notice any difference between a linear and non-linear study of the forces (this is very important as the rotor will be used as an accumulator of kinetic energy).

However, for a correct dynamic analysis and on the trajectory, it is advisable to implement the linear model of magnetic forces with the non-linear contribution.

These results will have to be confirmed by an experimental study.

Reference

[1]   http://www.wisegeek.com/what-are-neodymium-magnet.htm available in 2018-12-05.

[2]   Bonisoli E, Vigliani A, "Static behaviour of magnetoelastic forces". In: 16th AIMETA congress of theoretical and applied mechanics, Ferrara, 2003.

[3]   Earnshaw S., "On the nature of the molecular forces wich regulate the constitution of the luminiferous ether", Transaction of Cambridge Philisophie Society, 7(116), pp.97-112, 1842.

[4]   Braunbeck SW., "Körper Freischwebende in electrischen and magnetischen feld", Z. Phys, 112, pp.753-763, 1939.

[5]   Braunbeck SW., "Freies Schweben diamagneticher Körper in Magnetfeld", Z. Phys, 112, pp.764-769, 1939.

[6]   Bonisoli E., "Magnetic model for rotodynamics", Politecnico di Torino, Department of Mechanical and Aerospace Engineering, Internal rep

[7]   Genta G., *Vibration Dynamic and Control*, Springer Science, LLC, Turin,2009.

[8]   Vatta F., Vigliani A, *Lectures on*

Acknowledgments